



SPECTROSCOPY OF RED QUASARS

Niels Bohr Institute

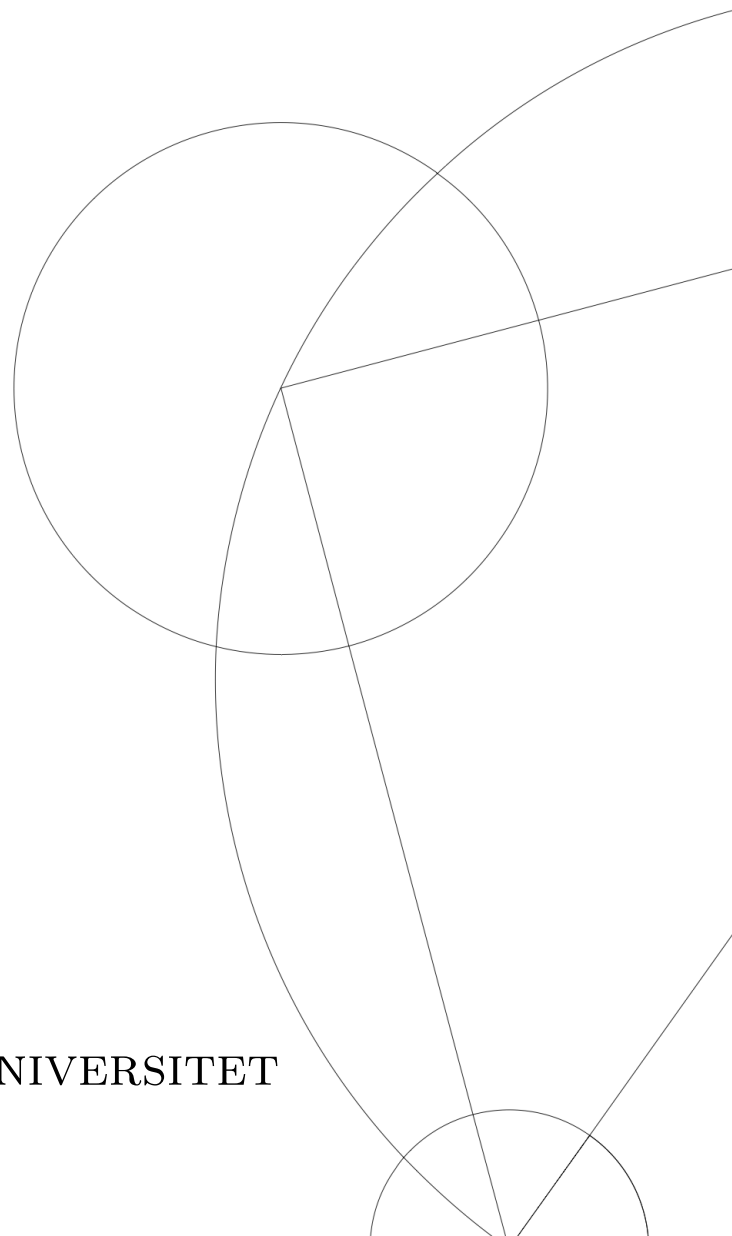
SPECTROSCOPY OF RED QUASARS

Skrevet af *Suk Joo Ko*

December 3, 2019

Under vejledning af
Johan Peter Uldall Fynbo

KØBENHAVNS UNIVERSITET





UNIVERSITY OF
COPENHAGEN

NAME OF INSTITUTE: Niels Bohr Institute

NAME OF DEPARTMENT: The Cosmic Dawn Center

AUTHOR(S): Suk Joo Ko

EMAIL: dch259@alumni.ku.dk

TITLE AND SUBTITLE: Spectroscopy of red Quasars
- Niels Bohr Institute

SUPERVISOR(S): Johan Peter Uldall Fynbo

HANDED IN:

DEFENDED:

NAME _____

SIGNATURE _____

DATE _____

Abstract

A quasar is the most luminous class of active galactic nuclei (AGN). The radiation from AGN is fueled by matter accreting onto a supermassive black hole with masses of sometimes several billion solar masses. The motivation for studying quasars is partly to understand the AGN phenomenon itself and partly to use quasars as bright lighthouses that we can use to study intervening material. An example of this use of quasars is the study of the chemical evolution of galaxies back to very high redshifts where information is very difficult to get at with other methods. Most quasars are optically blue objects. Some of them have optical colours redder than the normal quasars because of dust extinction due to dust either in the host galaxies or along the line-of-sight. Many optical surveys select quasars among point sources by using a method that relies on the fact that quasars are bluer than stars in some broadband filter combinations. However, fewer of the dust reddened quasars are selected in traditional optical surveys, such as the Sloan Digital Sky Survey, because the dust reddening moves them out of the selection windows in broad-band colour-colour diagrams. One possible cause of reddening is foreground dusty objects such as metal- and dust-rich damped Lyman- α Absorption (DLA) systems. The main objective of the thesis is to search for those reddened quasars using selection methods specifically designed to locate such objects among red point-sources on the sky. The data from where candidates are selected are from the ESO public imaging surveys called KiDS and VIKING (Kilo Degree Survey and VISTA Kilo Degree survey). Stellar and low redshift objects were rejected by setting colour criteria. A sample of candidate quasars have been observed prior to the onset of the project using the low-resolution OSIRIS spectrograph mounted on the 10.4-m Grand Telescopio de Canarias on La Palma. In the thesis the data have been reduced and analyzed. The redshift and extinctions of the confirmed candidates are found by a template matching of the quasar template from [Selsing *et al.*, 2016] and the extinction modeled using the extinction curve of the Small Magellanic Cloud (SMC) [Pei, 1992]. The candidates are classified as Type 1 broad emission line quasars, Type 2 narrow emission line quasars, Broad absorption line (BAL) quasars, quasars with DLAs, and stellar objects. The modeling includes both photometric and spectroscopic information. We have selected a sample of 54 candidates into the photometric selection. The blue population is about 76 % of the sample, where the red population is about 20 % of the sample. In the end, we find that our colour selection selects highly dust extinguished quasars at a rate of about twice as large as in the SDSS quasar catalogue. We also find that there are a higher fraction of BAL line quasars in our sample than in the SDSS quasar sample. BAL quasars are the most dominant population in the red population about 73 %, whereas the blue population in BAL quasars is about 45 %. Type 2 quasar groups seem to be relatively redder than type 1 group. The 46 % of the red population is type 2 quasars. The blue population has about 14 % of type 2 quasars. The bluest quasars in our sample are similar to some of the reddest quasars seen in the SDSS selection of quasars. The highest redshift in our sample is 3.64, and the highest V -band extinction is 0.80. The average redshift of samples is 2.368. The average redshift of the blue population is 2.437 whereas the red population is 2.111. The average V -band extinction of samples is 0.24. The average V -band extinction of the blue population is 0.223 and the red population is 0.312.

Contents

1	Introduction and motivation	3
1.1	The quasar phenomenon	3
1.2	Sources of spectral lines, different types of quasars, and the unified model	6
1.3	Absorption lines in quasar spectra	9
1.4	Radio loud and radio quiet quasars	11
1.5	Selection of red quasars	11
1.6	The objective of the thesis	12
2	Observations	14
2.1	Selection of KV-RQ quasars	14
2.2	Data characteristics	15
2.3	Observations from the Gran Telescopio Canarias	17
3	Data reduction	18
3.1	Data calibration	18
3.2	Normalization of spectra	25
4	Results	28
4.1	Determination of redshift and extinction with template matching	28
4.2	Fitting of DLA lines	32
4.3	Quasar classification	36
4.4	Stellar classification	37
4.5	The classification/identification of the samples	37
4.6	$g - r$ versus $r - i$ diagram	44
4.7	$g - r$ versus $J - K_S$ diagram	45
4.8	$W1 - W2$ versus $W2 - W3$ diagram	47
5	Discussion	49
5.1	Colour criteria	49
5.2	Missing and unclassified objects	55
5.3	DLA normalization errors	58
6	Conclusion	59
	References	62
7	Appendix	65
7.1	The list of chemical emissions of arc lamp	65
7.2	Spectral Classification of stars	69
7.3	Table of photometric data of [Heintz <i>et al.</i> , 2016]	77
7.4	Spectra of KV-RQ	78
7.5	The script: Dust extinction model	108
7.6	The script: Voigt profile	110

1 Introduction and motivation

1.1 The quasar phenomenon

A quasar is a luminous active galactic nucleus (AGN). An AGN is a high luminosity compact region that lies in the center of its host galaxy. The radiation is not produced from stars. The luminosity of a quasar can be several hundred times that of the entire Milky Way galaxy despite the fact that they have sizes comparable to the size of the solar system. AGN emit radiation over most of the electromagnetic spectrum from radio, infrared, optical, ultra-violet wavelengths and X-ray and γ -rays. The radiation from AGN is ultimately powered by accretion of matter onto a supermassive black hole (with masses of up to 10 billion solar masses) in the center of the host galaxies. The black hole itself does not radiate, because the light cannot escape from within the event horizon. The source of radiation is located outside the event horizon [Schmidt, 1963]. The detailed spectra of quasars are complicated (see Fig. 1). The continuum in the UV to the near-IR regime is believed to come from a host accretion disk close to the black hole, but there are also other emission regions, e.g. a so-called broad-line region, a narrow-line region, etc. The classification of AGN contains many classes. Quasars are AGN with optical luminosities higher than $10^{11} L_{\odot}$. AGN with optical luminosity lower than $10^{11} L_{\odot}$ are classified as Seyfert galaxies. The word "Quasar" comes from *quasi-stellar radio sources* because the first members of the class were identified as sources of radio emission that looked like stars in the optical band. In 1963 their nature as the luminous nuclei of distant galaxies was realised [Schmidt, 1963]. A few years later it was realised that there is a much more similar looking object without bright radio emission [Sandage, 1965]. Today, we know that radio-quiet objects and radio-loud objects are very similar objects, so we use the term quasar to refer to both radio and radio-quiet objects.

In photographic observation of quasars, they seem to be point-like and faint objects that resemble stars. The spectroscopic analysis showed that quasars do not emit the close to black-body emission characteristic for stars, and the emission/absorption lines from quasars are markedly different from the spectra of stars. The spectra of quasars contain bright UV flux, broad emission lines, and often time-variable flux both in the continuum and in the emission lines.

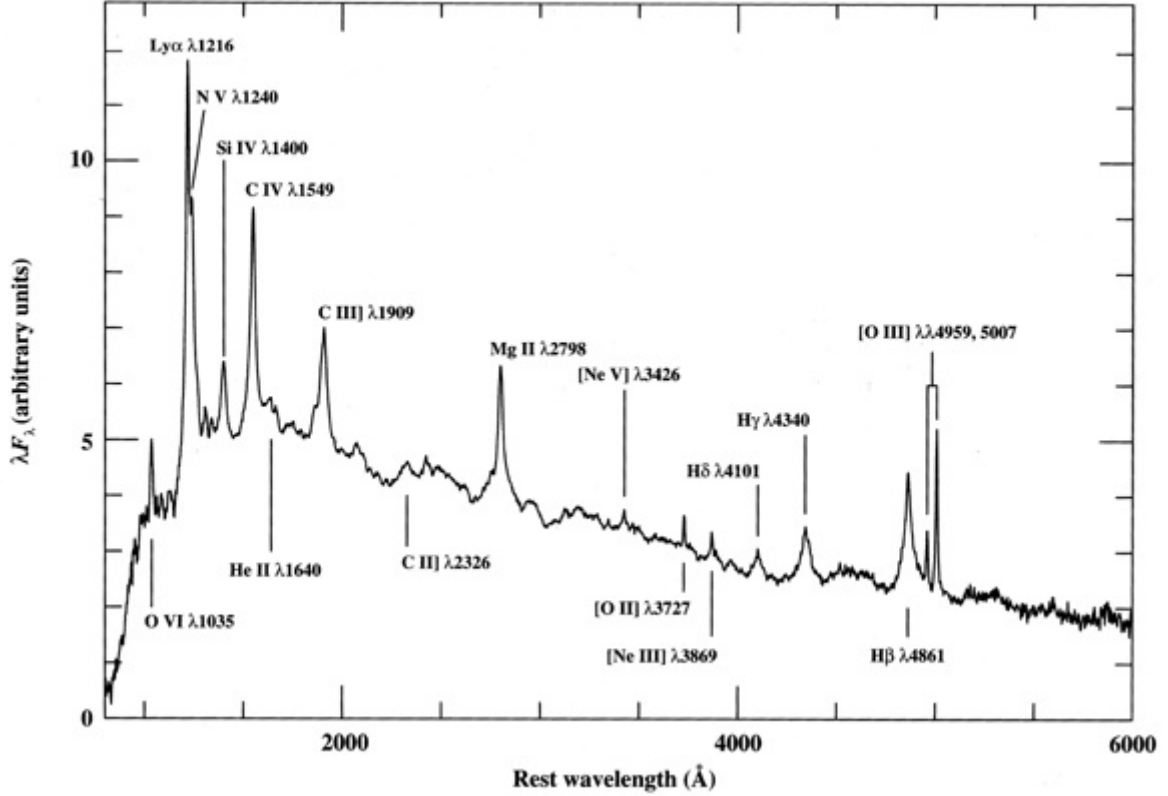


Figure 1: A composite spectrum made by combined spectra of over 700 quasars [Francis *et al.*, 1991]. The quasar spectra are from the Large Bright Quasar Survey. The emission lines from gas and metals appear different compared to the close-to black body spectra of stars. The drop in the blue is due to intergalactic hydrogen absorption.

The emission lines of quasar are broad because of the Doppler effect and the rapid movement of the clouds forming the emission. The clouds move around the nucleus with velocities of thousands of kilometers per second, and some part of radiation become a blueshifted or redshifted depending on the position in the orbit.

The first quasar was found at a redshift of 0.13 (3C273, [Schmidt, 1963]). The most distant quasars are currently observed in the redshift range of $6 < z < 7.5$. By Hubble's law, the redshift of cosmic radiation is the result of the expansion of the Universe. The comoving density of quasars is highest at redshifts around 2 and then drops both moving back in time and forward in time [Shaver *et al.*, 1996]. The most distant quasars show that quasars must have formed when the Universe was less than 700 million years old. The most distant quasar, ULAS J1342+0928 has redshift of $z = 7.54$ [Bañados *et al.*, 2018]. A quasar sends its energy in all directions, some of the AGNs send most of its energy at the direction of jets. Only few jets from quasars point directly toward to the Earth. Such quasars are known as Blazars.

The radiation of AGN is enormous and the radiation pressure acts as a force on the gas pointing away from the center where the luminosity is formed. The intense radiation pressure can deactivate the radiation by halting the in-fall of new material and hence the fueling process. To remain luminous the outward pressure should be smaller than the inward gravitational force caused by the black hole to keep the in-fall of new fuel and hence the radiation process active. This gives rise to the concept of the so-called Eddington luminosity, which is the maximal luminosity and object with a given mass can have without being disintegrated by the radiation pressure. The Eddington luminosity can be estimated in the following way. The radiation

pressure can be estimated assuming that the most important link between the radiation and matter is Thompson scattering on free charged particles. Thompson scattering is the elastic scattering from the electromagnetic radiation that affects a charged particle. It is an electron scattering that create the outward force. The scattering on protons is less efficient comparing to electrons because of its almost 2000 times larger mass. The cross-section of the scattering of electrons is,

$$\sigma_T = \frac{e^4}{6\pi\epsilon_0^2 c^4 m_e^2} = 6.653 \cdot 10^{-25} \text{cm}^2 \quad (1)$$

where e is the charge of the electron, ϵ_0 is the constant of permittivity of free space, c is the speed of light and m_e is the electron mass. The electron scattering drags the proton together, so the inward gravitational force includes both proton and electron. When there is a balance between the gravitational force and the radiation pressure we have,

$$\frac{GM(m_e + m_p)}{r^2} = \frac{\sigma_T L}{4\pi r^2 c} \quad (2)$$

where G is the gravitational constant, M is the mass of center, m_p is the mass of the proton, r is the radius, and L is the luminosity. The Eddington luminosity describes the largest luminosity of a quasar can have, that the state is in the balance of gravitational force and radiation pressure,

$$L_E = \frac{4\pi GMm_p c}{\sigma_T} \approx 3 \cdot 10^4 \frac{M}{M_\odot} L_\odot \quad (3)$$

where L_\odot is the bolometric luminosity of the Sun. The argument underlying this calculation is one of the strong arguments behind the theory that AGN are powered by accretion onto a black hole: there has to be something very massive in a very small area to sustain the bright emission.

The gravitational falling of matter onto a black hole cannot last forever. The in-fall can stop for a range of reasons, e.g. if the luminosity of the quasar blows it away if the gas is simply all consumed. In the end, quasars turn off and the galaxy will turn into normal galaxies without AGN. The black hole will still be there but will be in a passive state. Most galaxies contain a massive black hole in its center, which means that most galaxies must go through AGN phases one or more times during their evolution. The processes that cause black holes to accrete must be related to the processes that cause galaxies to form new stars as the redshift evolution of star-formation and AGN follow each other closely (see Fig. 2).

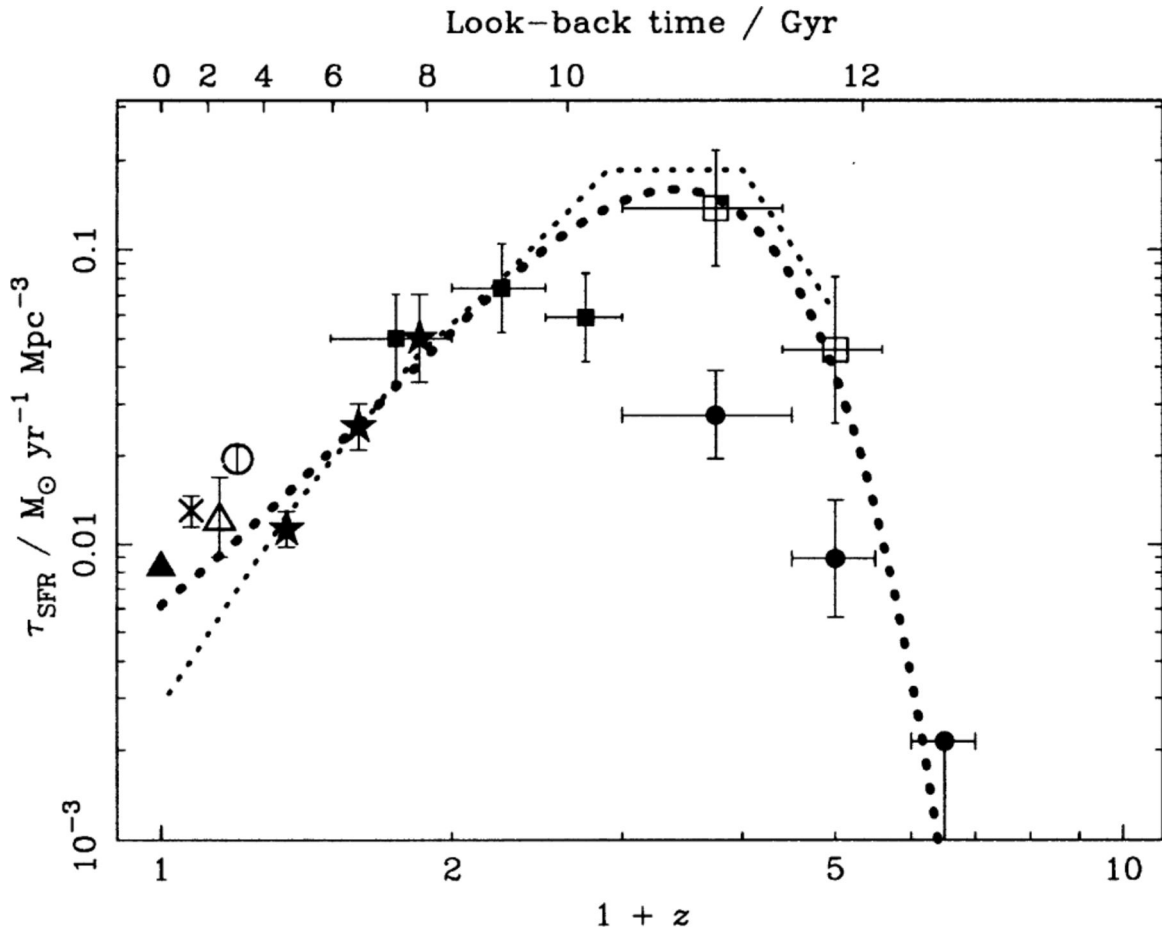


Figure 2: The function of redshift that display the star formation rate (SFR) as $(\tau_{SFR}(r))$. Note that the evolution of the luminosity density of AGN at a wavelength of 280 nm (Boyle Terlevich 1998) is marked as the thin dotted line. The plot displays the evolution of the luminosity density, converted into SFR of assuming $\tau_{SFR} = 10^{-2} M_{\odot} \text{ yr}^{-2}$ is equal to $10^{17} W H z^{-1} M \text{ pc}^{-3}$. Other lines are SFR of ultraviolet/optical/near-infrared observations. The SFR of redshift resembles the evolution processes of the AGN luminosity density. We believe the SFR and the AGN luminosity density are related. [Blain *et al.*, 1999]

The motivation for studying quasars are many. Important examples include the study of the evolution process of early galaxies and the ambition to understand the conditions in the early Universe. The studies of quasars are also used to solve cosmological problems, that data from quasars are used to test various cosmological models [Sandage, 1965]. One of the important reasons for studying quasar is to know about the re-ionization of the intergalactic medium during the first Gyr after the Big Bang. The so-called Lyman- α forest contains information about the density of neutral gas in the early Universe. The absorption lines in quasar spectra from the structure along the line-of-sight also give evidence for the metal formation in the early stage of the Universe. We have many reasons to study quasars and improve our cosmological models [Sparke & Gallagher III, 2007], [Peterson, 1997]

1.2 Sources of spectral lines, different types of quasars, and the unified model

The spectral lines of quasars contain a lot of information. We can identify the type, velocities, and chemical content of the clouds around the radiation source from the spectral lines. The clouds and the host galaxy around the AGN emit or absorb photons in different wavelength

regions. The broad line regions are made in clouds with neutral hydrogen densities of $n_H \geq 10^{10} \text{cm}^3$ [Sparke & Gallagher III, 2007]. The region also generates emission lines from ionized gas such as HeII at 4686 Å, OVI at 1402 Å, NV at 1239 Å, 1243 Å and CIV at 1548 Å and powered from the soft X-ray from the nucleus. The broad emission lines are often the most characteristic feature in AGN spectra.

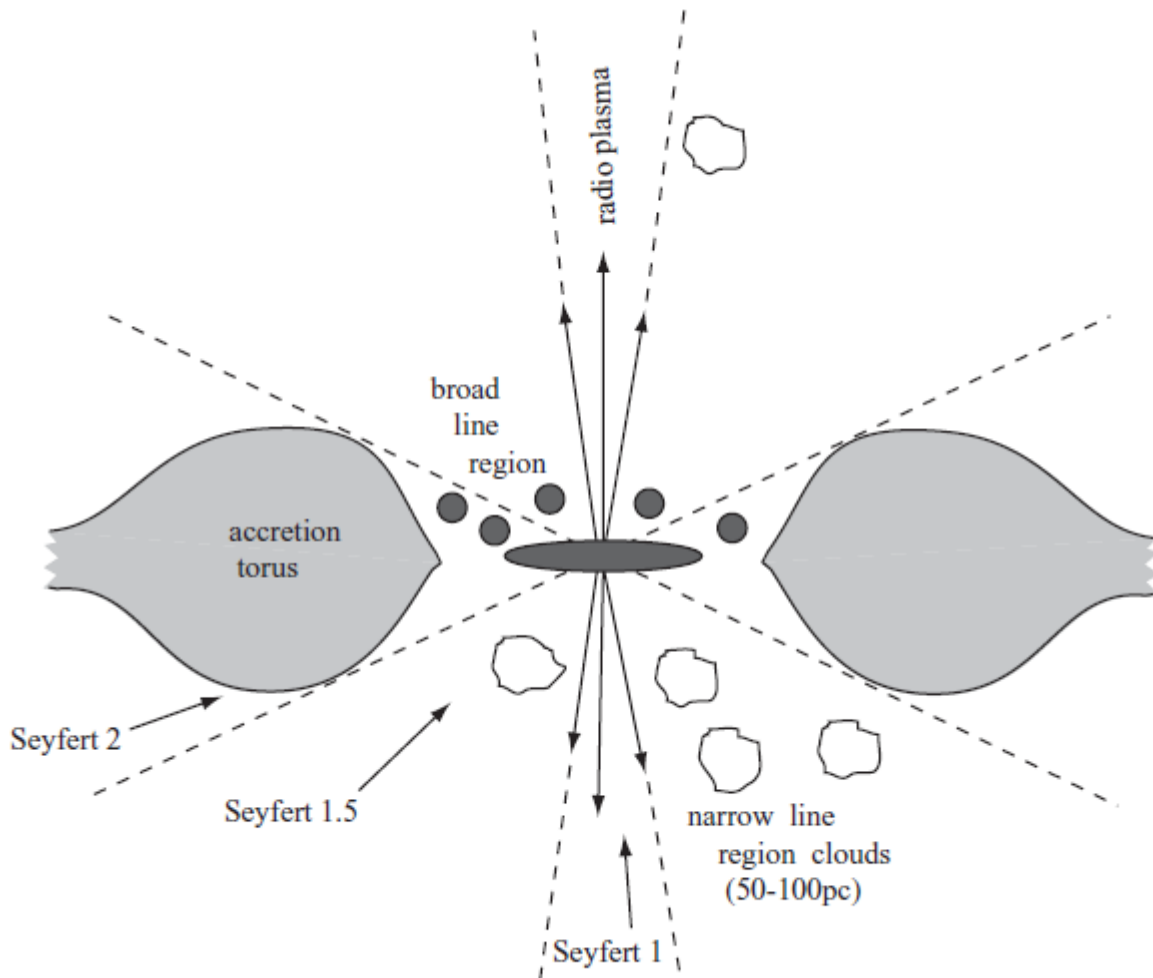


Figure 3: A simple model of an active galactic nucleus [Sparke & Gallagher III, 2007]. The fast-moving broad line regions are close to the nucleus of $\leq 1pc$ and slow-moving narrow line regions are lie in distance of 50 – 100pc. The direction of view changes the type of AGN. The type 1 quasars have view angle of Seyfert 1 and type 2 quasars have view angle of Seyfert 2.

The unified model of a quasar suggests (see Fig. 3) that the broad emission lines come from a region close to the black hole and its accretion disk shielded from some viewing angles by a dust torus. Some of the quasar spectra do not show broad emission lines. The unified model of quasar suggest that those missing broad-line region clouds are hidden behind the dust torus, where the angle of our view is blocked by the torus [Sparke & Gallagher III, 2007].

Many quasars also show narrow emission lines - either only narrow lines or superimposed on the broad lines. These are supposed to originate from lower density clouds further away from the black hole in the region referred to as the narrow-line region. The position of the narrow-line region clouds lies above the nucleus, outside of the broad-line region and torus. The low density of electron allows doing forbidden lines as [O II] at 3727 Å and [O II] at 5007

Å [Sparke & Gallagher III, 2007]. Forbidden lines generated by collisions of atoms, where the region of density $n_H \leq 10^8 \text{cm}^3$ permits forbidden lines for excited atoms that decay by emitting forbidden lines [Sparke & Gallagher III, 2007]. The forbidden lines can use to measure electron densities and temperature of the clouds.

Quasars are classified as Type 1 quasars if the broad lines are seen and type 2 quasars if only narrow lines are seen (see Fig. 4). In other words, Type 1 quasars are dominant of broad emission lines and few narrow lines, where Type 2 quasars are lack of broad lines and dominant of narrow lines. The unified model suggests that spectral lines of quasars are depending on the angle of view. Spectra of Type 1 quasars observed with avoiding the dust torus and central disks. In this case, the spectra include lines of broad-line region and narrow-line region. The Type 2 quasars has no broad line emissions because the view of the broad lines is blocking by dust torus [Sparke & Gallagher III, 2007].

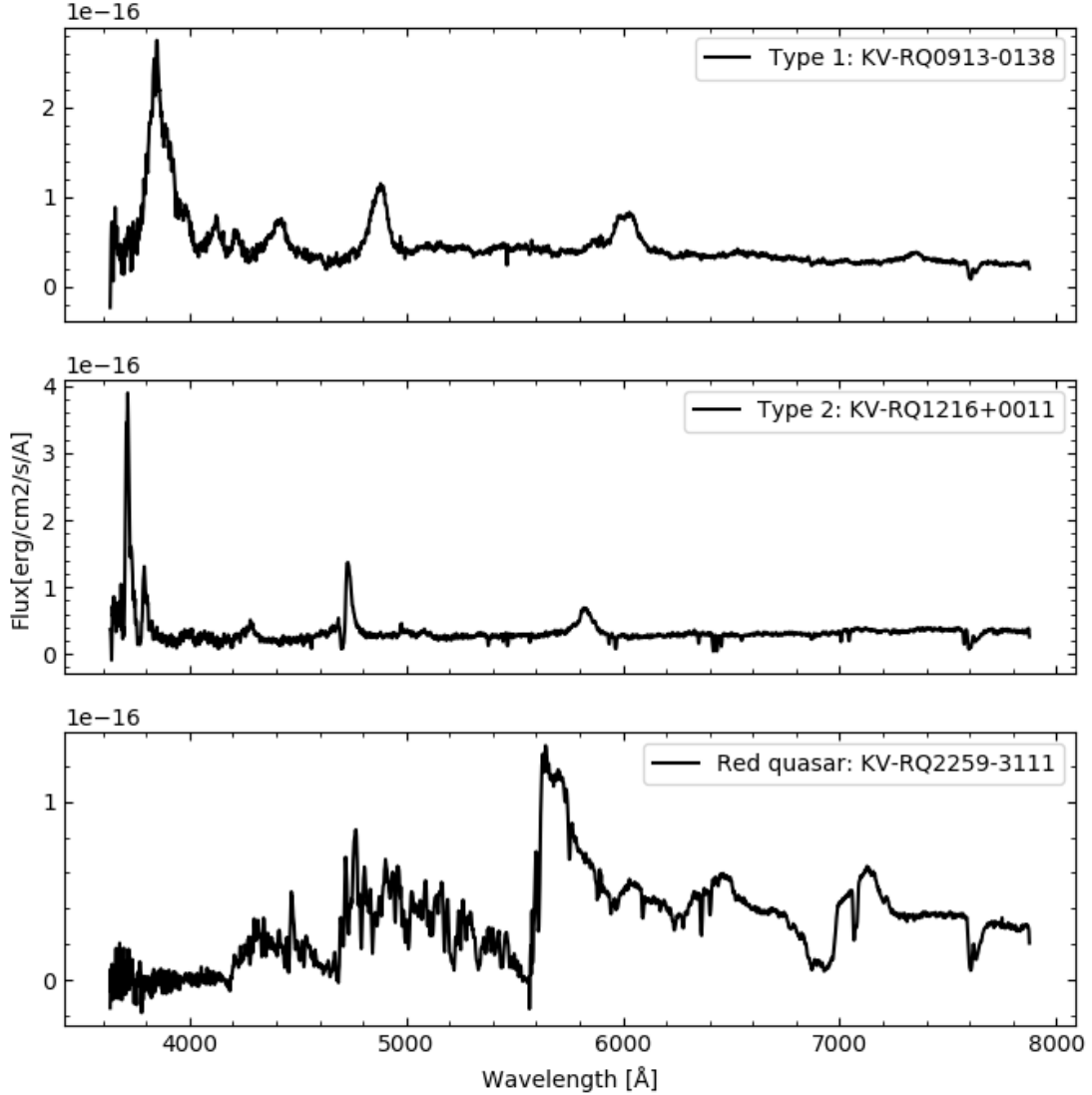


Figure 4: The three plots of different types of quasars. The above plot shows type 1 KV-RQ0913-0138 quasar that is dominant in broad emission lines. In the middle, the plot shows type 2 KV-RQ0908-0003 quasar of many narrow emission lines. The plot below shows red KV-RQ2259-3111 quasar of weak emission of the blue colour and strong emissions of the red colour.

1.3 Absorption lines in quasar spectra

Many absorption lines in quasar spectra come from intergalactic gas at lower redshift than the quasar itself - from so-called intervening absorption system. Most of the lines appear narrow because the intergalactic gas intercepts photons only close to the resonance frequency as the clouds are cold. Absorption lines appear most as groups of patterns, as an example, the magnesium and carbon absorption lines found as doublet pairs. MgII at 2796 Å, 2803 Å observed in the absorbing clouds of redshift $0.2 \leq z_{abs} \leq 1.5$ where the CIV at 1548 Å, 1551 Å observed in $0.2 \leq z_{abs} \leq 1.5$. The intergalactic gas covers from strong neutral clouds to diffuse gas of highly ionized gas. [Peterson, 1997].

Some quasars show very broad absorption lines and are therefore referred to as Broad absorption line (BAL) quasars. The lines are from the blueshifted absorption in the quasar's rest frame (host galaxy). Most of BAL quasars are dominated by high ionization absorption lines of CIV at 1548 Å, SiIV at 1394 Å, 1403 Å and NV at 1239 Å, 1243 Å. About 15% of BAL quasars have low ionization absorption lines of MgII at 2796 Å, 2803Å, AlII at 1671 Å, AlIII at 1855 Å, 1863 Å and CII at 1335 Å. [Peterson, 1997].

High concentrated neutral hydrogen clouds are observed as damped Lyman- α system (DLA) inside of few quasar spectra. The column density of neutral hydrogen of $N(HI)2 \cdot 10^{20}cm^{-2}$ displays absorbed damping wings in the spectrum of a quasar [Sparke & Gallagher III, 2007]. Those clouds are called as the Lyman α clouds. The damped wings are broadened by radiation damping of Lyman α absorption of neutral hydrogens. The Damped Lyman- α system also corresponds to the Lyman limit for the clouds of $N(HI) \geq 10^{17}cm^{-2}$. The Lyman limit appears as the flux of the quasar drops to zero in the wavelength of $912(1 + z_{abs})\text{Å}$ [Sparke & Gallagher III, 2007], [Peterson, 1997].

When a hydrogen cloud absorbs photons, the absorbed energy excites an hydrogen atom. Damped Lyman- α systems (DLAs) are the strongest hydrogen absorbers with column densities of neutral hydrogen above $210^{20} cm^{-2}$. Lyman limit clouds are made of mainly ionized hydrogen gases but has column densities of neutral hydrogen above about a few $10^{16} cm^{-2}$ where they become optically thick at the Lyman limit (912 Å). The gas density of DLAs are close to the most of outer HI disks of Milky way and present nearby galaxies. It suggests that the DLAs trace early stage of the galaxy formation [Sparke & Gallagher III, 2007], [Peterson, 1997]. The Lyman α clouds are observed most as an absorption line of the quasar spectrum, instead of the light emission from their stars. The observation of damped Lyman α cloud spectra displays the metal and dust absorption in the clouds. Typical metal lines of damped Lyman α clouds are MgII at 2796 Å, 2803 Å, ZnII at 2026 Å, 2063 Å, CrII at 2056 Å, 2062 Å, 2066 Å, CIV at 1548 Å and SiIV at 1394 Å [Peterson, 1997]. Clouds of density around $N(HI) \geq 10^{16}cm^{-2}$ give rise to the strong metal lines from low ionisation species such as MgII, SiII, CII, and OI [Peterson, 1997]. Those lines are often found in neutral hydrogen disks of present galaxies. CIV and SiIV are found in present galactic halos. MgII metal lines are found in all of the DLAs [Peterson, 1997]. The spectrum below the Lyman α wavelength can be completely absorbed for very distant quasars of redshift ≤ 6 because of the combined effect of many Lyman α lines. It is called a Gunn-Peterson trough [Peterson, 1997]. The highest redshift of our data in this thesis is 3.64 so we will not observe this feature.

The study of DLAs is important for the study of galaxy formation in the early Universe. Most DLAs are observed at relatively high redshift between $2 < z_{abs} < 4$, where this is the time area of the neutral hydrogen dominated at the Early Universe [Peterson, 1997]. The low redshift limit comes from the fact that wavelengths below about 3000 Å cannot be observed from the ground due to the Ozon layer in the atmosphere. DLAs at redshifts $0 < z < 2$ have been studied with the Hubble Space Telescope, which is equipped with UV sensitive spectrographs.

The ultraviolet photons can penetrate clouds of density below $N(HI) \leq 10^{16}cm^{-2}$, where most of the intergalactic hydrogens are ionized by ultraviolet photons. At the cloud of $N(HI) \geq 3 \cdot 10^{16}cm^{-2}$, the dominant absorption lines in the spectrum are Lyman- α hydrogen lines. The Lyman- α forest is an absorption series of multiple Lyman- α lines from multiple gas clouds of different redshifts. The Lyman- α forest is often used to determine the density

of neutral hydrogen and the temperature of the clouds. Some of Lyman- α forests have a density of neutral hydrogen enough to have damping wings as a damped Lyman-alpha system. [Sparke & Gallagher III, 2007], [Peterson, 1997]

1.4 Radio loud and radio quiet quasars

We can identify the type of quasars by reading its spectrum. In addition to the distinction between type 1 and type 2 quasars, quasars are also classified as either radio-loud or radio-quiet. Obviously, the strength of the radio emission determines if a quasar is a radio-loud or a radio-quiet quasar. The radio-loud quasars have strong radio-wavelength emissions. Those radio wavelength emission is emitted from powerful jets and they constitute about 10 % of the quasar population [Peterson, 1997] The radio-quiet quasar has weak radio-wavelength emission comparing to radio-loud quasar. Most of the quasar population is dominated by radio-quiet which is around 90 % of the population [Peterson, 1997] Some of the quasars have broad absorption lines (BAL), the blueshifted absorption lines from the quasar's rest frame. These broad absorption lines are from outflows of gas of the AGN. Most of BAL quasars are radio-quiet quasars and inside of broad absorption lines we found ionized metal elements like carbon and magnesium.

1.5 Selection of red quasars

The most frequently applied technique to identify quasars among the much more numerous stellar sources on the sky is photometric optical selection. The photometric approach consists in registering radiation input in passbands of different wavelengths using filters. Each filter register radiation of different wavelengths from near ultra-violet to mid-infrared. We can map out the spectral shape of the object by comparing the strength of different wavelengths. As example, we can compare the strength of ultraviolet band and strength of the near-infrared band. Most quasars have strong UV emission and therefore we often out-select quasars from stars by comparing the blue magnitude (short-wavelength strength) and red magnitude (long wavelength strength). In that case, the technique may have a selection bias against dusty quasars as dust extinction affects the blue light more than the red light. There are several ways a quasars can be reddened, e.g. due to dust in the host galaxy or dust in intervening material.

Many major spectroscopic redshift surveys, as Sloan Digital Sky Survey, contains systematically biases toward the population of red quasars [Strauss *et al.* , 2002], [Krogager *et al.* , 2016]. Sloan Digital Sky Survey uses $u - g$ versus $r - i$ selection for selecting the low redshift quasars and $g - r$ versus $i - z$ selection for selecting the high redshift quasars [Richards *et al.* , 2002]. The optical surveys have also an issue of biases against high redshift quasars of $z > 2.5$. HI absorbers as Ly- α forest, damped Ly- α system, and Lyman limit systems enter at the ultra-violet bands in the redshift region of $z > 2.5$. HI absorbers will absorb most of the continuum radiation in u- band and the strength of ultraviolet filter to be redder [Fan, 1999]. The colour of dust extincted quasars resemble of main-sequence stars in the traditional selection (see Fig. 5).

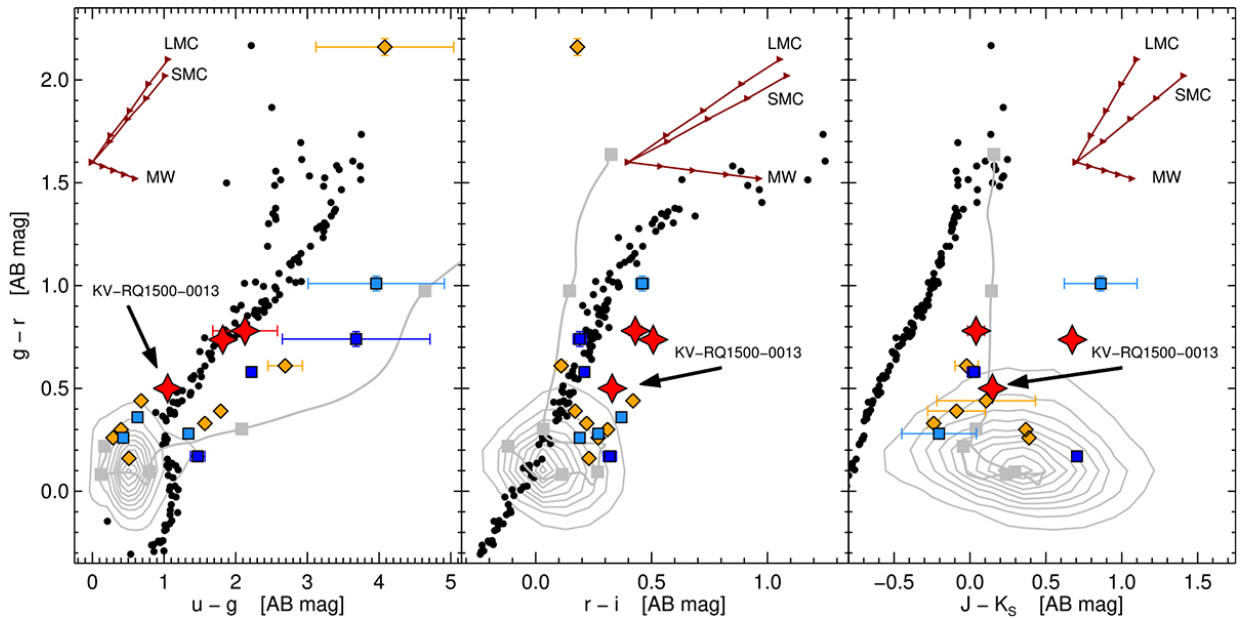


Figure 5: KV-RQ1500-0013 is the dusty DLA quasar. The black dots are the main sequence stars from [Hewett *et al.*, 2006]. The colour-colour diagram of $g - r$ versus $u - g$ shows that the dusty KV-RQ1500-0013 is close to the stellar population. The gray contours are the SDSS-DR12 quasar population at $1.5 < z < 4.0$, where the red arrows are reddening vectors of LMC, SMC and MW (Milky Way) of different extinction. Red stars are the quasars which misclassified as stars in SDSS and classified quasars in KV-RQ surveys. Blue squares are photometrically selected to be quasars in the SDSS (light) and BOSS (dark) surveys. Orange diamonds are observed partly of the SDSS and BOSS survey and selected as radio sources [Heintz *et al.*, 2018].

Recent studies estimate that the missing population of dust-reddened quasars in the optical survey is a fraction between 10 % to 40 %. [Heintz *et al.*, 2016]. Many of those missing quasars are highly extinguished, containing metal rich clouds, has weak emission lines or broad absorption lines [Richards *et al.*, 2002], [Richards *et al.*, 2003]. The damped Ly- α system usually tends to be missed than other dust poor quasar, where damped Ly- α system quasars lie behind dust rich galaxies or metal-rich galaxies. [Krogager *et al.*, 2016]

1.6 The objective of the thesis

The traditional photometric selection of SDSS may have a selection bias against the significant population of redden quasars. The main purpose of this thesis is to make a selection method of the potential dust biased red quasars with new techniques. The Niels Bohr Institute developed the new technology that is optimized for selecting quasar of significantly redder spectral energy distribution. The selection method is aimed to avoid the dust biases. The thesis is mainly motivated by [Heintz, 2019], the optical infrared photometric colour selection criteria for targeting quasars at $z \geq 2$. In $z \geq 2$, we can observe dusty DLAs that may have a selection bias in the classical quasar surveys.

The approach is to search the population of highly dust reddened quasar, rather than building an unbiased selection. We will search the dust red population from the data of KiDS VIKING Red Quasar (KV-RQ) survey by using colour criteria of $g - r$ versus $r - i$, $g - r$ versus $J - K_S$ and $W1 - W2$ selection.

The properties as the redshift, the extinction, the identification of quasar type or the identification of stellar type are investigated through spectral analysis. We can identify and characterize the samples by combining photometric and spectral analysis.

2 Observations

2.1 Selection of KV-RQ quasars

The colour criteria in the selection have the purpose to select reddened dust biased samples, especially dusty DLAs. The selection criteria will mainly focus on selecting quasars at $z \geq 2$. We will mainly select our samples from optical/near-infrared photometry.

$$g - r > 0.0; \quad r - i > 0.5; \quad (4)$$

The $g - r$ versus $r - i$ selection colour criteria motivated from [Fynbo *et al.*, 2012] is used to include the reddest sources in the optical selection

One of the problems of the quasar selection is to select the quasars from the stellar populations, especially dwarf stars. The optical wavelength strength of dwarf stars resembles the quasars, we need to exclude them with the caution.

$$0.5 < g - r < 1.1 \quad J - K_S < 0.8; \quad (Blue) \quad (5)$$

$$g - r > 1.1 \quad or \quad J - K_S > 0.8 \quad (Red) \quad (6)$$

The $g - r$ versus $J - K_S$ colour criteria is used as supplemental stellar rejection criteria. These colour criteria have the purpose to divide quasar samples into the two groups. The blue colour group and the red colour group. The blue colour group selects blue magnitude quasars and the red colour group selects red magnitude quasars from the stellar population [Heintz, 2019].

The $g - r$ versus $J - K_S$ colour criteria requires the additional criteria, especially for the selection of the red colour samples. The dwarf stellar population is close to the red quasar population in the optical and near-infrared region. We will use the WISE colour selection to reject the dwarf stellar population.

$$For \quad W2 - W3 < 2.75; \quad W1 - W2 < 0.8 \quad (Blue) \quad (7)$$

$$For \quad W2 - W3 > 2.75; \quad W1 - W2 < 0.62(W2 - W3) - 0.91 \quad (Blue) \quad (8)$$

$$For \quad W2 - W3 < 2.75; \quad W1 - W2 < 1.0 \quad (Red) \quad (9)$$

$$For \quad W2 - W3 > 2.75; \quad W1 - W2 < 0.62(W2 - W3) - 0.71 \quad (Red) \quad (10)$$

The mid-infrared $W1 - W2$ versus $W2 - W3$ colour criteria is used to reject quasars of redshift $z < 2$. [Krogager *et al.*, 2016]

The WISE colour selection has additional colour criteria. $W1 - W2 > 0.4$ for the blue colour group and $W1 - W2 > 0.6$ for the red colour group. Those boundaries are used to reject contaminated stars and galaxies from the high redshift quasars. The most of contaminating sources are found near red samples, so the boundary of $W1 - W2 > 0.4$ blue sources is smaller than red sources. [Heintz, 2019]

The errors of colour criteria are defined by the propagation of uncertainty.

$$\sigma_{Colour} = [\sigma_{Colour_1}^2 + \sigma_{Colour_2}^2]^{\frac{1}{2}} \quad (11)$$

We also have used an overall flux limit of $J < 19$. This is simply to secure that the targets are bright enough for spectroscopic follow-up.

2.2 Data characteristics

The quasar samples are from KiDS VIKING Red Quasar (KV-RQ) survey. The KiDS refers to the Kilo Degree Survey and VIKING refers to the VISTA Kilo Degree. The KiDS is an optical imaging survey of 1500 square degree that uses Astro-WISE as the main tool to cooperate and use for the hardware resource. The data products of KiDS are intended to deliver data to European Southern Observatory (ESO). [de Jong *et al.*, 2013] VIKING is a survey of 1500 square degrees like KiDS. The survey uses VISTA z , Y , J , H , and K_S bands to collect rest-frame optical samples of galaxies of $z \geq 1$. VIKING supplies two other surveys as VISTA Hemisphere Survey (VHS) with a large area, shallower depth, and VIDEO by the photometric depth and smaller spatial coverage. The VIKING detects distant quasars, low-mass stars, galaxy clusters and super galaxy clusters to $0.7 < z < 2$. [Edge *et al.*, 2013]

The KV-RQ built by using photometric data from KiDS and VIKING survey. The data are about two magnitude deeper than the detection limits of the SDSS and the UKIRT Infrared Deep Sky Survey (UKIDSS). By improving the classification of detecting dust-redden quasars of optical to near/mid-infrared photometry with a large number of quasar data, KV-RQ survey improved identifying of quasars at $z > 2$ and removed most of unwanted objects as dwarf stars and compact galaxies. [Heintz *et al.*, 2018]

The photometric catalog of the data was compiled by cross-matching of the Kilo-Degree Survey Data Release 3 survey, the VISTA Kilo-Degree Infrared Galaxy Data Release 2 and the WISE AllSKY data release. Each survey covers different colours. KiDS covers $u(3550 \text{ \AA})$, $g(4775 \text{ \AA})$, $r(6230 \text{ \AA})$ and $i(7360 \text{ \AA})$ filters. The VIKING survey covers near-infrared $Z(8770 \text{ \AA})$, $Y(10200 \text{ \AA})$, $J(12520 \text{ \AA})$, $H(16450 \text{ \AA})$ and $KS(21470 \text{ \AA})$ filters. The filters converted flux into AB magnitude of $m_{AB} = -2.5 \log_{10}(f)$. The AllWISE surveys near-infrared covers $W1(3.4 \mu m)$, $W2(4.6 \mu m)$, $W3(12 \mu m)$ and $W4(22 \mu m)$ filters of Vega catalog.

The candidates was required to be detected in both KiDS and VIKING and to have photometric data of the g , r , i , J and KS filters and WISE 1, 2 and 3 bands of a signal-to-noise ratio of minimum 3 ($\frac{S}{N_{(W1-3)}} \geq 3$). The KiDS catalogue defined a morphology flag for each as SG2DPHOT. $SG2DPHOT = 1$ for high confidence stars, $SG2DPHOT = 2$ for objects

with a FWHM less than the typical stellar locus, $SG2DPHOT = 4$ for stars following their star/galaxy classification, $SG2DPHOT = 5$ for high-confidence star that satisfies their star/galaxy classification and $SG2DPHOT = 0$ for likely galaxies. The sample includes only sources of $SG2DPHOT \geq 1$. The VIKING survey has P_{GAL} value, a probability to the object is a galaxy. In [Venemans *et al.*, 2013], the P_{GAL} selection is required to remove foreground galaxies from quasar colour selection. [Venemans *et al.*, 2013] used $P_{GAL} \leq 0.95$. In our case we used $P_{GAL} \leq 0.90$.

The catalogue has a magnitude limit of $J < 20$ in the near-infrared magnitude. The purpose is to avoid biasing sample of heavily reddened optical colours [Heintz, 2019].

The template spectrum are a tool to investigate the reddening by extinction, and redshift of samples. We can determine the extinction curve of samples by using template matching of observed samples and template spectra. Small Magellanic Cloud (SMC) extinction curve is often used to match the extinction with the template spectrum. The problem of combining various QSO samples are that they collected at different times and different telescope instruments. Those differences cover wider rest frame regions and may contaminate the composite spectrum. The template spectrum of [Selsing *et al.*, 2016] selected blue QSOs at redshift of $1 < z < 2.1$ from SDSS. The template uses the observations from X-shooter to cover ultraviolet to near-infrared light, that composite spectrum covers the rest frame range from Lyman α to 11350 Å with no serious contamination.[Selsing *et al.*, 2016]

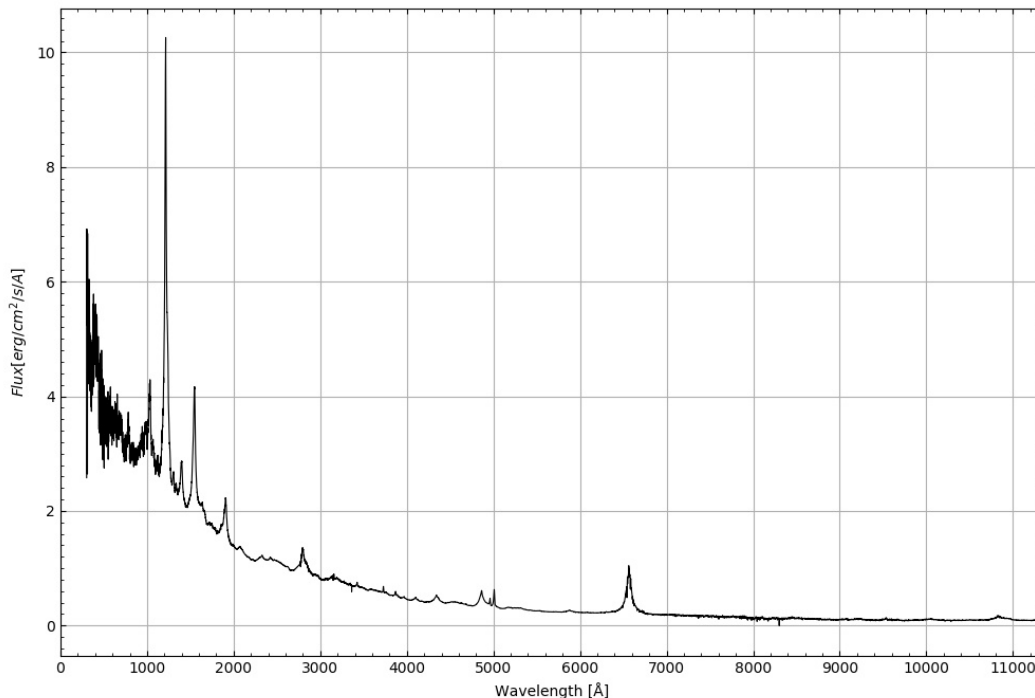


Figure 6: The composite spectrum of wavelength from 0 Å to 11350 Å. The template is a collection of blue QSOs of the redshift of $1 < z < 2.1$ from SDSS [Selsing *et al.*, 2016].

2.3 Observations from the Gran Telescopio Canarias

The spectra of the KV-RQ candidate quasars have been obtained from the Gran Telescopio Canarias (GTC) telescope, using the Optical System for Imaging and low-Intermediate-Resolution Integrated Spectroscopy (OSIRIS) spectrograph. OSIRIS is a spectrograph for the optical wavelength range from 3650Å to 10000Å. OSIRIS has a total field of view of 7.8 x 8.5 arcmin for direct imaging and 7.5 x 6.0 arcmin for multi-object spectroscopy. (<http://www.gtc.iac.es/instruments/osiris/>)

Grism 1000B was used to obtaining The spectra of KV-RQ with a wavelength range from 3630Å to 7500 of the resolution of 1018. Grism 1000B has a 65 % peak efficiency of dispersion pixels $2.12D(\text{Å}/pix)$.

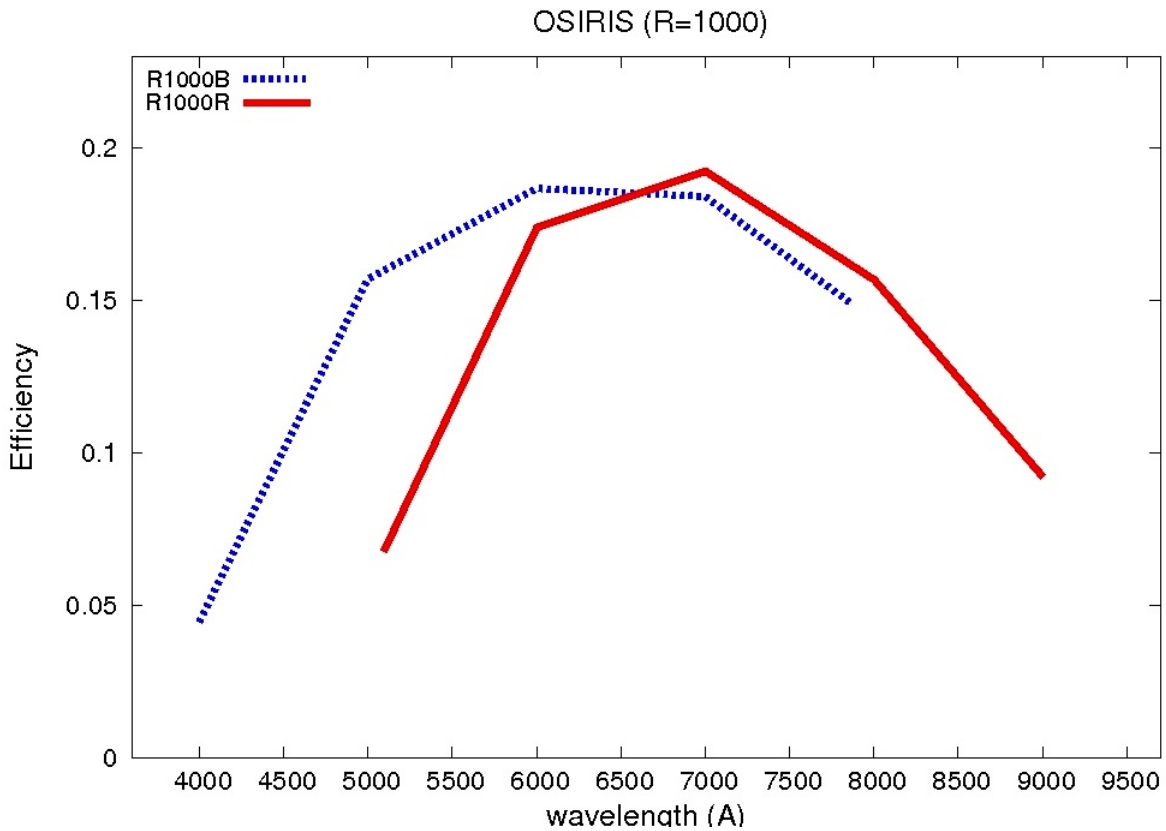


Figure 7: The efficiency of the OSIRIS Grism over the wavelength. The spectra of KV-RQ is obtained from the Grism 1000B, marked as the blue dashed lines. (<http://www.gtc.iac.es/instruments/osiris/media/OSIRIS-R1000.jpg>).

3 Data reduction

3.1 Data calibration

The Charge-Couple Device (CCD) collects the electronic signal of photons into light-sensitive pixels. Each pixel registers signal of photons into a digital value. Those digital values have no physical value without any calibration, so we should change it to physical value. We have to calibrate a CCD image to an useful scientific data. The raw image of CCD contains noise and systematic errors. The data has been calibrated from bias frame, dark current frame and flat field by image data processing. Bias frame is the electronically added offset, to cover no exposure time with a closed shutter. It is a constant offset so it doesn't make a negative value of the pixel to corrupt the data. Dark current is the thermal noise from the electrical excitation. When an electron from the material of CCD does a thermal excitation, it causes a registration of the digital value into a pixel. We measure dark current with exposure time more than zero with a closed shutter. Dark current has been already calibrated in our image, so we don't have to subtract the value of the dark current. A flat field is used to correct that the sensitivity of CCD pixels that is not constant as each pixel. We use the flat field to correct those individual differences of sensitivity. Our final image of science frame is,

$$science\ frame = \frac{raw\ image - bias\ current}{normalized(flat\ field - bias\ current)} \quad (12)$$

The data has been calibrated with the image data processing by IRAF. Now the data set should calibrate with long-slit spectroscopy. We have to subtract the sky background, calibrate digital values to wavelength and flux. We have to subtract the sky background as cosmic rays before we calibrate the digital value into physical value. We used L.A. Cosmic by Pieter G. van Dokkum (<http://www.astro.yale.edu/dokkum/lacosmic/>), an algorithm to detect cosmic rays of arbitrary shapes and size. By using L.A. Cosmic we can select cosmic rays and subtract it from our sample. Before we use L.A. Cosmic, the data should be bias-subtracted, flat-fielded and not sky subtracted. As previous steps, our data has been bias-subtracted and flat-fielded. We used parameters as `yorder = 5` (order of sky line fit), `objlim = 2.1` (contrast limit between cosmic ray and underlying object), `sigfrac = 0.5` (fractional detection limit for neighbouring pixels), `sigclip=4.5` (detection limit for cosmic rays as sigma), `nfilter = 4` (maximum number of iterations) and `gain = 0.95` (gain electrons/ADU).

We need to calibrate the wavelength, extract and trace one-dimensional spectra of the quasar after subtracting cosmic ray. The CCD image has a pixel position of X values and Y values. Z values are the intensities of the pixels. These pixel positions should be converted to reference wavelength by arc lamps. Arc lamps are made of heated chemical lamps, where each lamp contains a heat emission of a single chemical element. Those chemical emission lines are measured in the laboratory, where we can use those lines to reference wavelengths. The list of chemical emissions of the arc lamp is in the Appendix.

We can use the IRAF task `identify` to mark one-dimensional image vectors and finds dispersion function for spectra (in this case, arc-line calibration spectra). We will mark strong peaks of spectra to search chemical lines of CCD image and calibrate the wavelength.

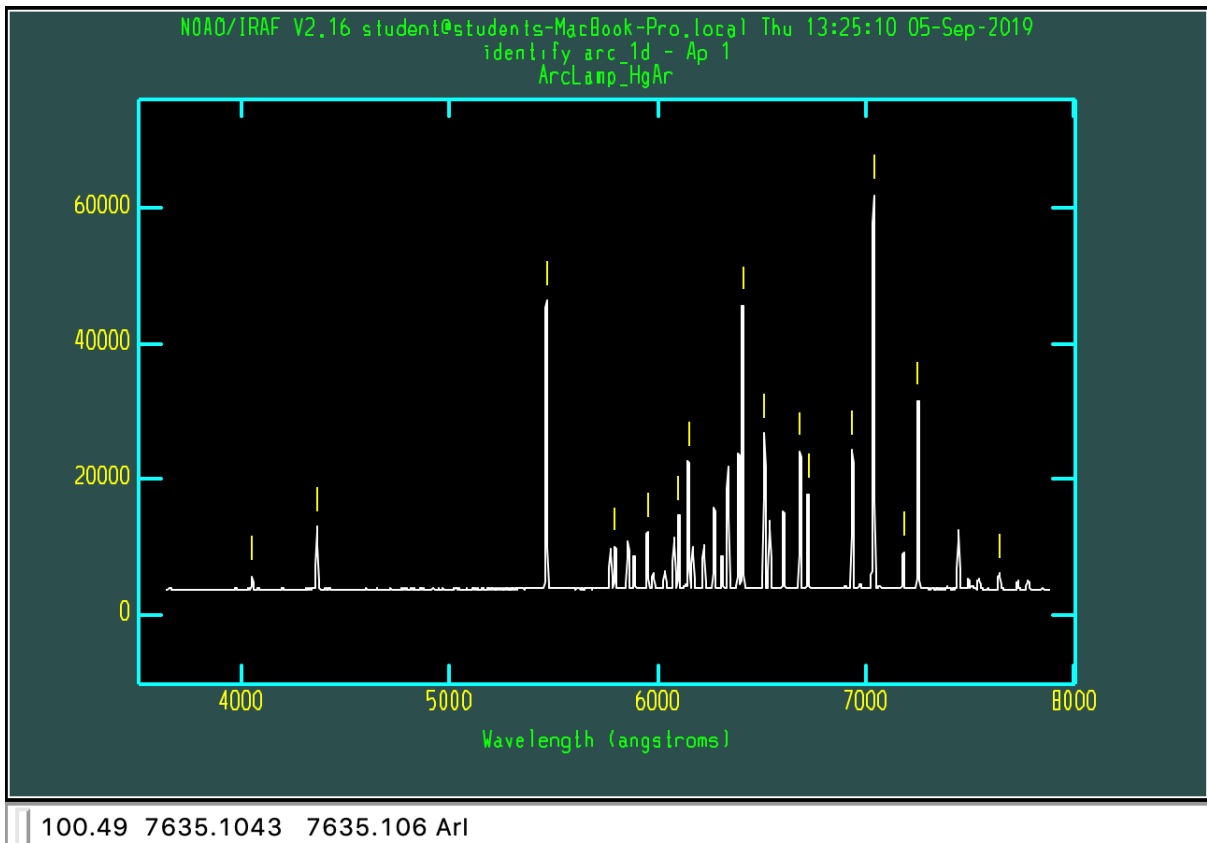


Figure 8: IRAF task `identify` marked strong peaks of spectra by referring the arc lamps. The dispersion function of the measurement will be used for the calibration of the wavelength. The x-axis is the wavelength measured in \AA and the y-axis it the counts of the elements.

Our data is the long-slit science image of a 2-dimensional spectrum. The 2D frame has the position of X-axis along the Y-axis. We want to extract the data of a one-dimensional spectrum to analyse our data. The data needs to be traced and extracted to the 1D spectrum. First, we have to find our object before tracing the spectrum. By IRAF task `apfind` we can select the object and remove from the background.

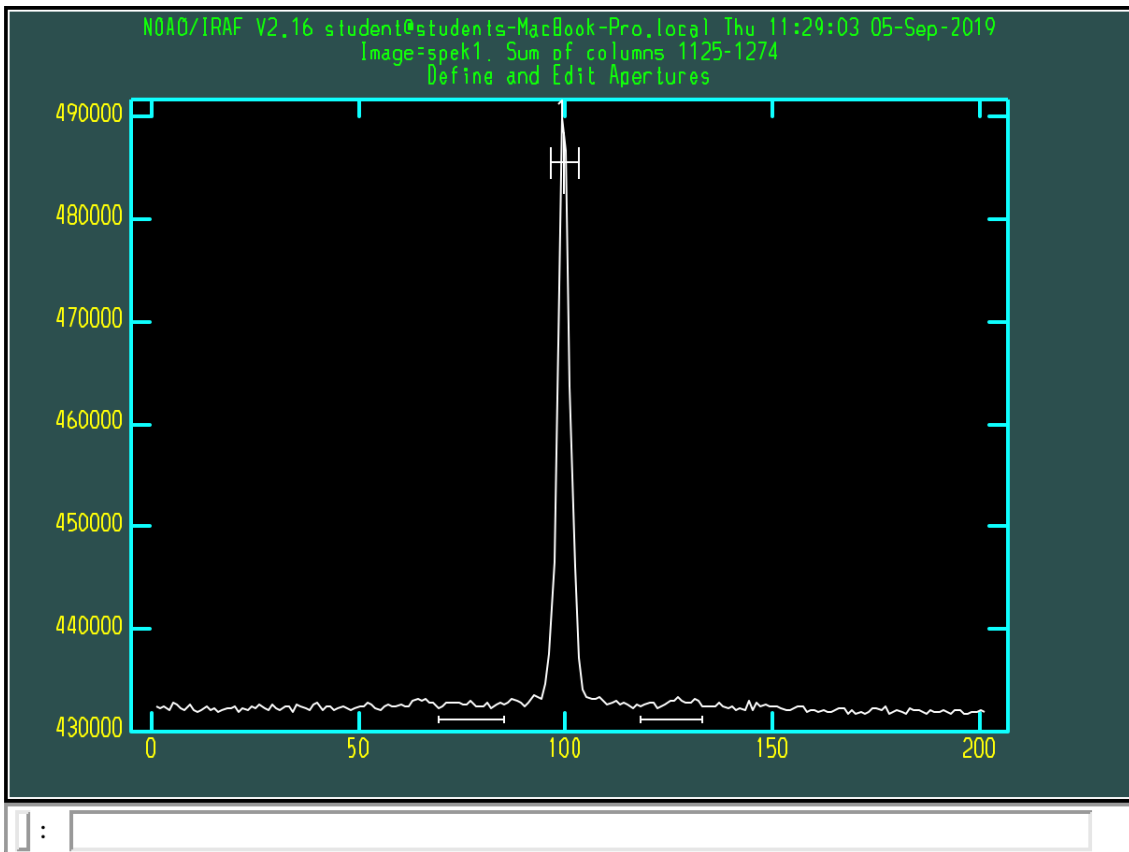


Figure 9: IRAF task `apfind` selected the main object with a central marker. The markers from below are background selections. The x axis is the pixels and the y axis is the sum of the columns.

The spectrum is not consistently following columns. Therefore, we have to trace the spectrum with IRAF task `aptrace`. We can delete outlines and change the value of order of the fit with `aptrace`.

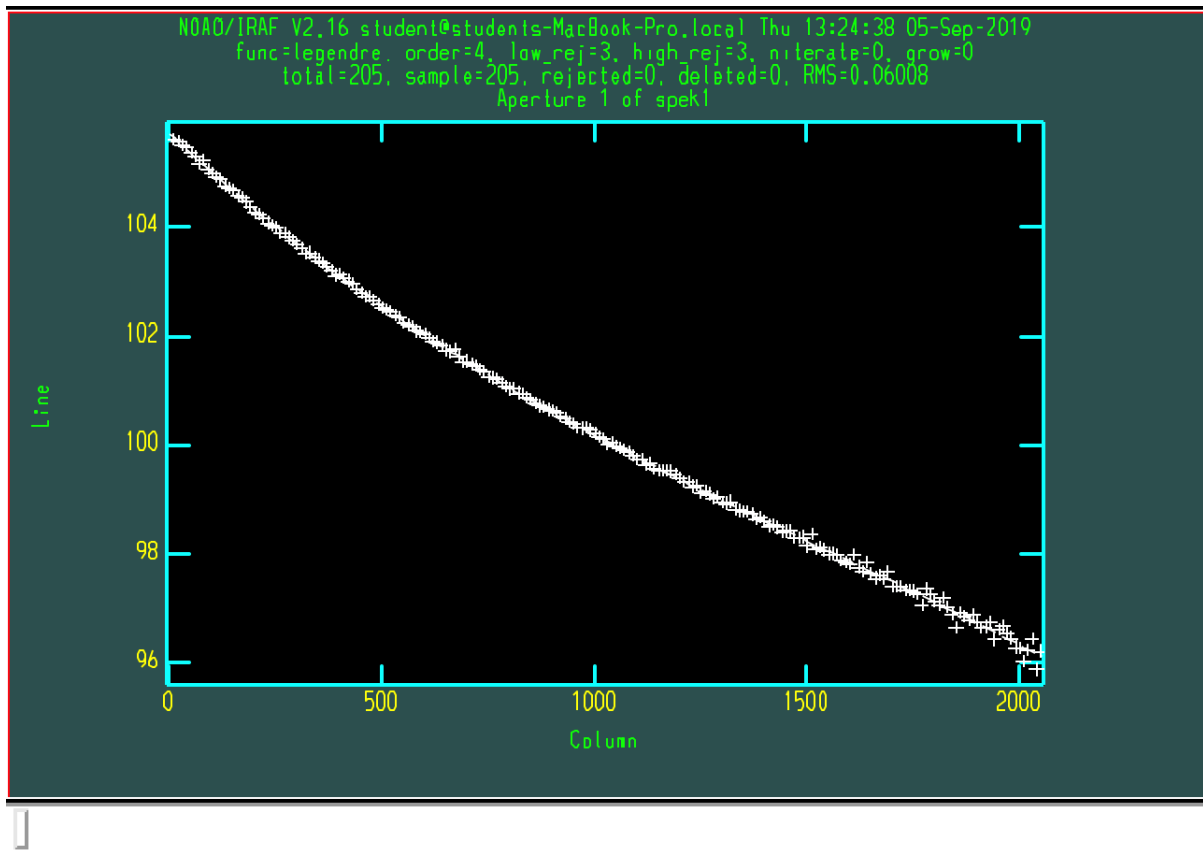


Figure 10: IRAF task `aptrace` fitted the spectrum of the order of 4. The fitted function is the Legendre polynomial function. The x-axis is the lines of a 2-dimensional spectrum and the y-axis is the columns.

After tracing the spectrum, we will extract our one-dimensional spectrum by using IRAF task `apsum`. All of the extraction processes of our one-dimensional spectra can be done by IRAF task `apall`, that does IRAF tasks `apfind`, `aptrace` and `apsum`.

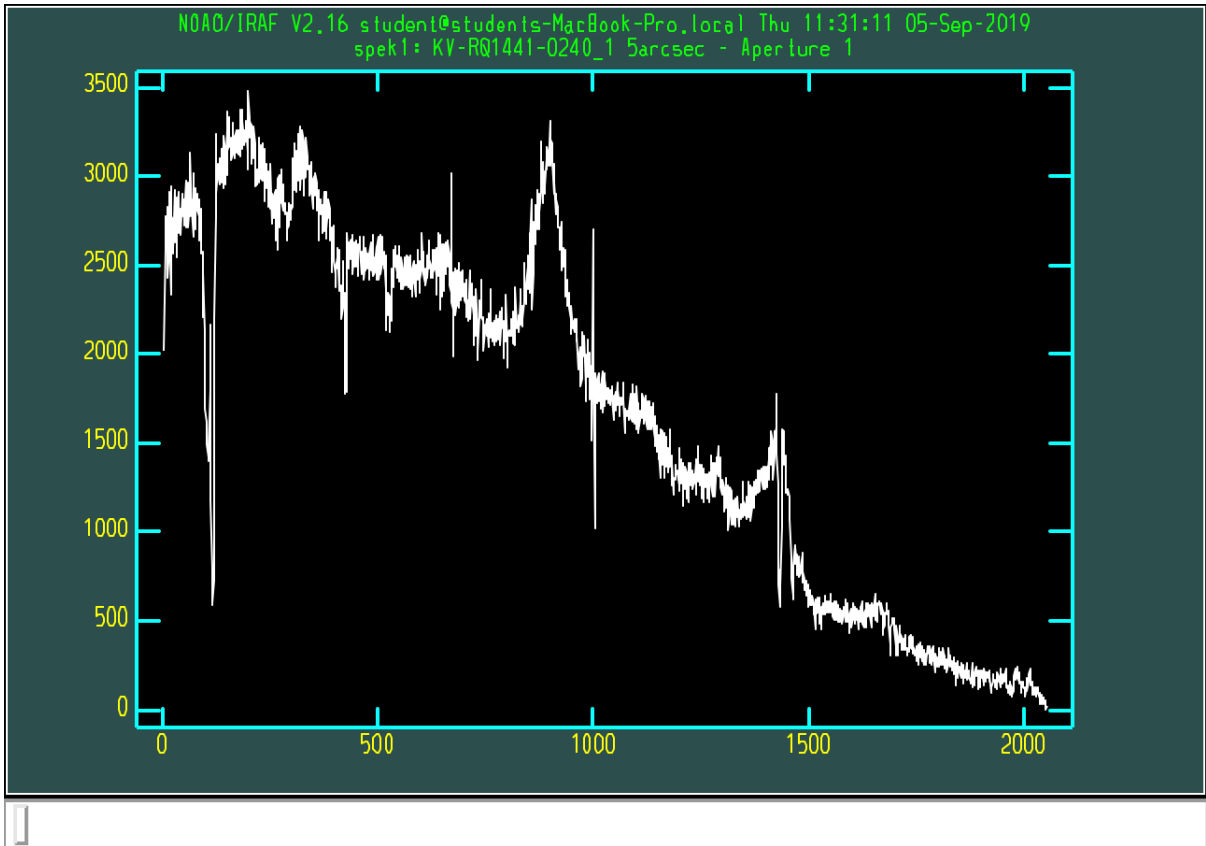


Figure 11: IRAF task `apsum` extracted the one-dimensional spectrum without a physical unit of flux. The flux of the spectrum is the pixel value and the wavelength is not in the physical value.

The data needs to be flux calibrated. The detector measures photons as pixel values with a sensitivity. The sensitivity function of the detector describes how sensitive is a signal measures as a pixel. By using the sensitivity function of the detector, we can transform the pixel value into the physical value as flux [$erg/cm^2/s/\text{\AA}$]. The common method to measure instrumental sensitivity is observing a spectrophotometric standard star with known spectral flux in absolute units. We observed a signal of the star and by using known flux as a reference, we can then calculate a sensitivity function of the machine. Each sample has used a specific spectrophotometric standard star as a reference of the sensitivity function. The first step of calculating the sensitivity function is, to subtract the sky background and extract a one-dimensional spectrum of the standard star. The process is the same as in the quasar samples from above. We have to change the value of exposure time and airmass of previous tasks and adjust the standard star. Those physical quantities can be found by reading the header of the data by either IRAF `imhead - long+` or using FITS tool as `grepfits OBJECT EXPTIME AIRMASS`. We do the same processes of the previous calibration of a quasar, as background subtraction, wavelength calibration, and 1D extraction. Now we have to produce an input data with the sample of standard star by using the IRAF task `standard`. The input data contains calibration information as a spectrum identification line, the spectrum image name, the sky image name, the aperture number, the length of the spectrum, the exposure time, airmass, wavelength range, and title. The identification lines are made of band-pass wavelength, the fluxes in the band-passes and information about the band-passes. The parameters of the IRAF task `standard` should be adjusted with the data of standard star, before we run the task.

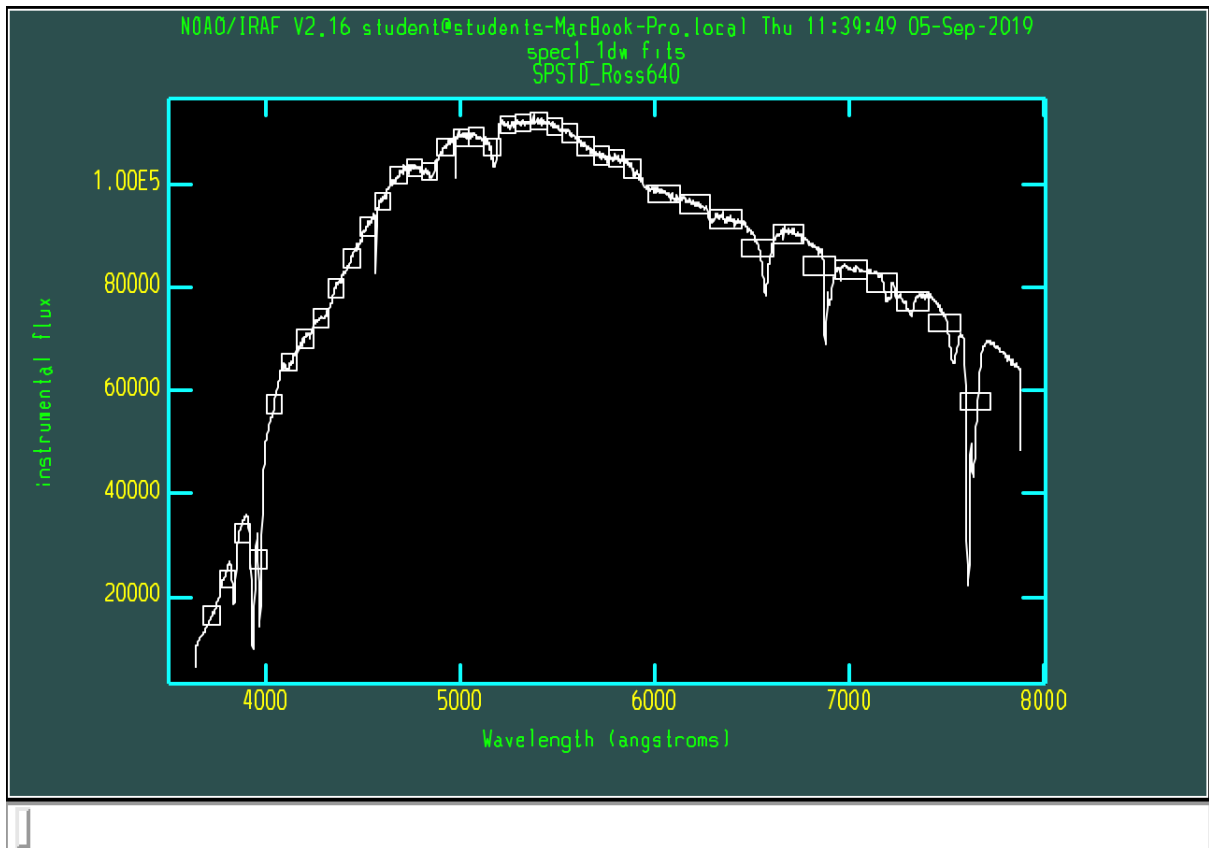


Figure 12: IRAF task `standard` creating the input data for calculating the sensitivity function. The x-axis is the wavelength, measured in \AA and the y-axis is the instrumental flux.

We input the finished standard star data file into IRAF task `sensfun` to create the sensitivity function of detector.

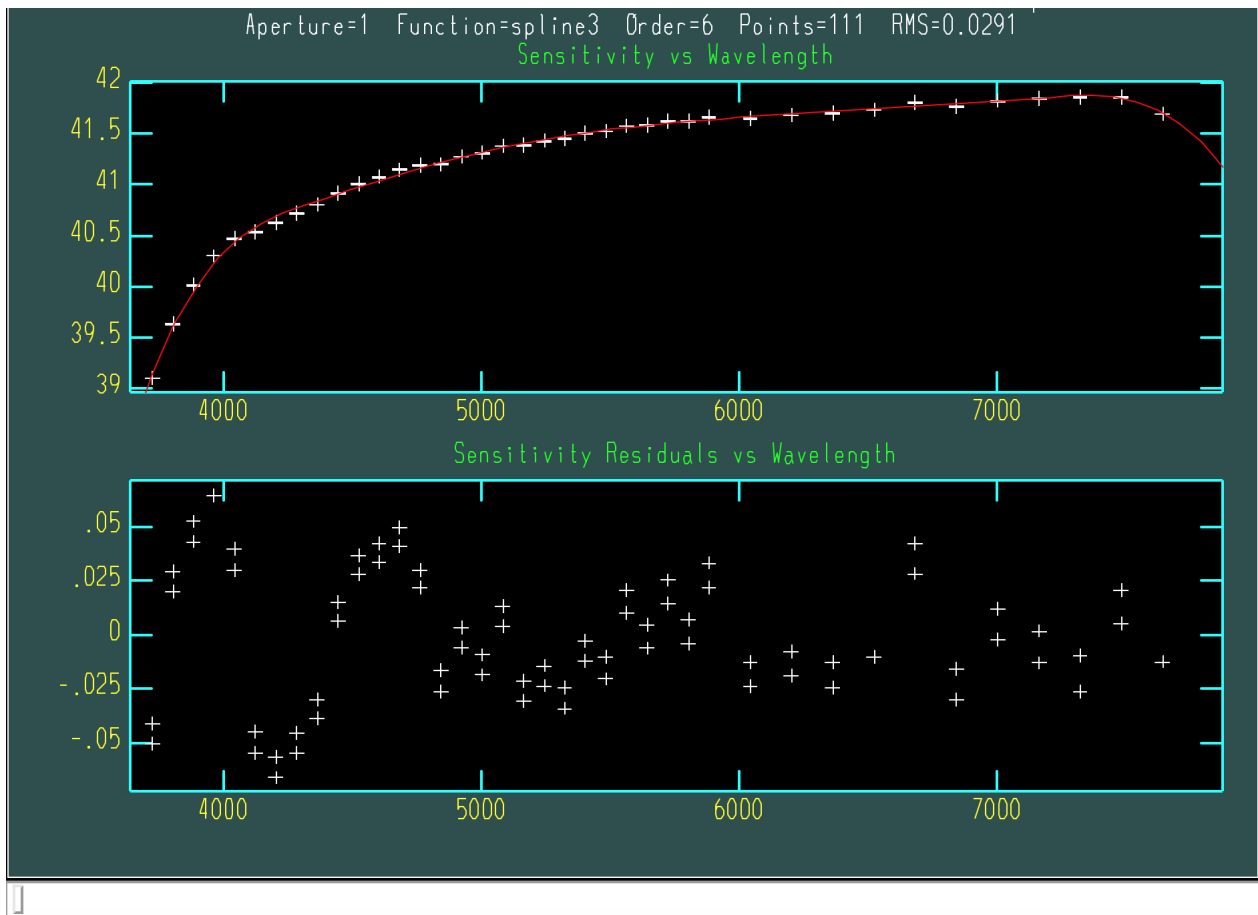


Figure 13: IRAF task `sensfun` creates the sensitivity function of the detector by using the input data of the standard star. The x-axis is the wavelength, measured in Å. The y-axis for plots are sensitivity and sensitivity residuals.

After creating the sensitivity function and 1D extraction, the extracted data can be flux calibrated of IRAF task `calibrate`. By setting exposure time, air mass of the quasar and the sensitivity function into the IRAF task `calibrate`, the pixel values of extracted data changes to flux [$\text{erg}/\text{cm}^2/\text{s}/\text{Å}$].

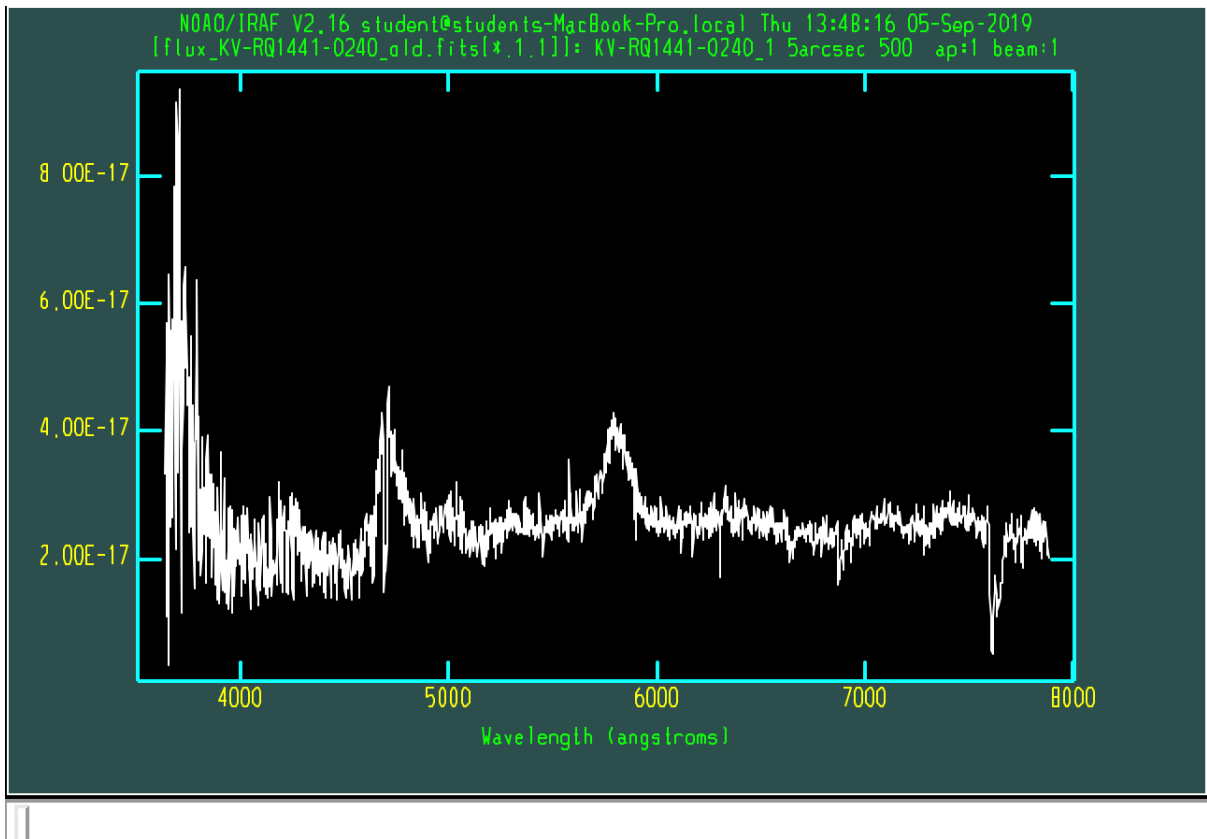


Figure 14: IRAF task `calibrate` changed the pixel values to physical units. The flux is measured in $[erg/cm^2/s/\text{\AA}]$ and wavelength is measured in the \AA .

The data set is now FITS file containing physical information of the sample. The headers of 'NAXIS1' (Axis length), 'CD1.1' (WCS matrix element 1,1) and 'CRVAL1' (RA at Ref pix in decimal degrees) are used to plotting wavelength in the Python. The details are in the Appendix.

3.2 Normalization of spectra

Some of the extracted 1D spectra contain DLA systems. In order to fit the Lyman- α lines, we need to normalize those spectra to be able to fit the lines with a Voigt profile. The detail of fitting with the Voigt profile is written in section 4.2. In this section, we will focus on how to normalize our extracted 1D spectra. We used Python script `specnorm.py` (<http://python4esac.github.io/plotting/specnorm.html>) to obtain the normalized absorption spectrum of the sample.

We can access the window displaying the sample's 1D spectrum, by using `specnorm.py` with iPython terminal to a file containing two columns of wavelength and flux. In this window, we can mark the continuum point of a quasar by left or right-click to select or deselect continuum points. After selecting all necessary continuum points, we can fit the splines to the continuum by hitting `Enter`. Button `n` normalizes the spectrum, and button `w` to write normalized result into the file.

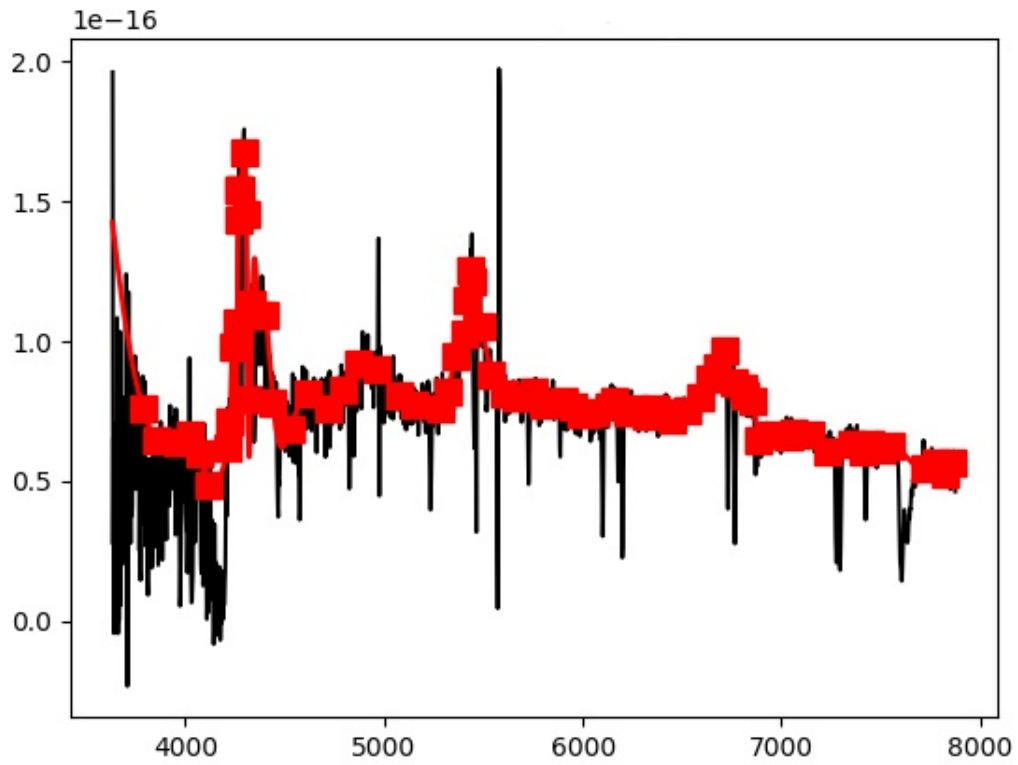


Figure 15: The extracted 1D spectrum of KV-RQ1500-0013 quasar in the script `specnorm.py`. The red squares marked continuum points of the spectrum and red lines are fitted splines.

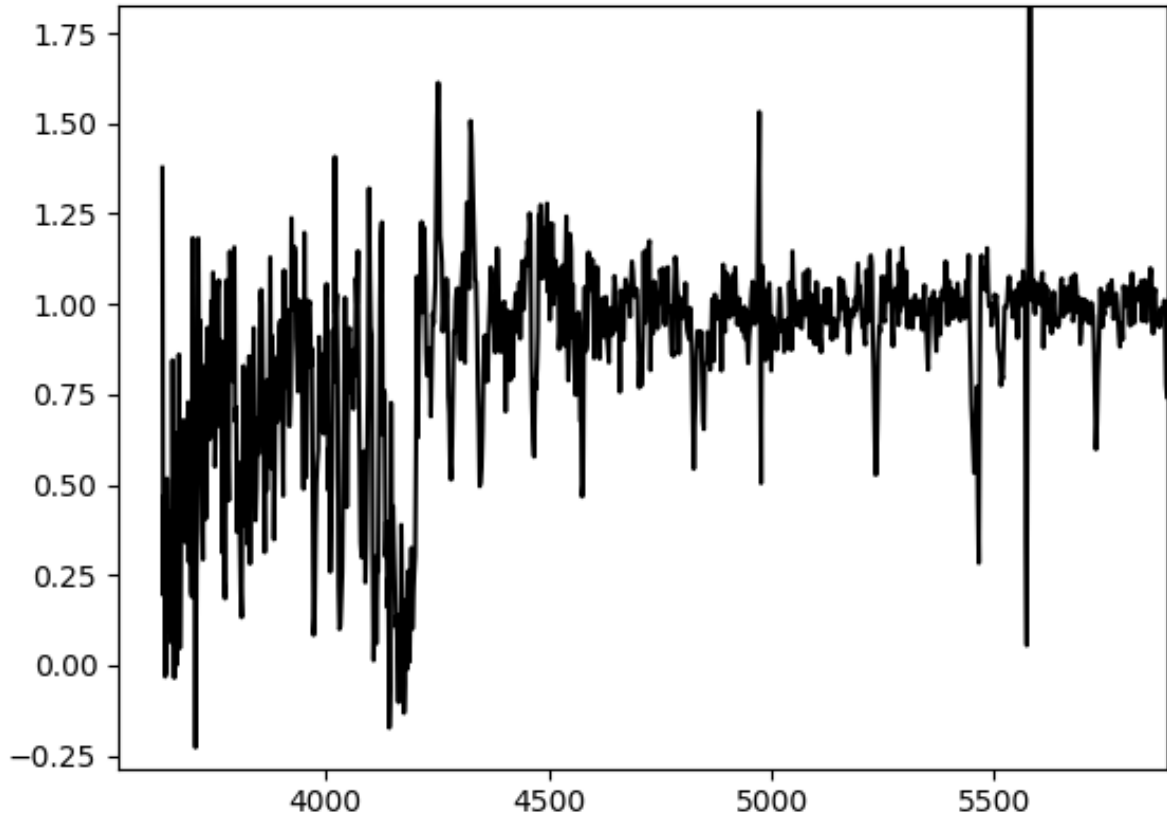


Figure 16: KV-RQ1500-0013 quasar is normalized after fitted splines. By zooming closer, the KV-RQ1500-0013 has an absorption line that suspects to be a damped neutral hydrogen wing of DLA.

4 Results

4.1 Determination of redshift and extinction with template matching

The measured spectrum is strongly affected by the expansion of the Universe and the resulting cosmological redshift. The wavelength of the light will be redshifted when the light of the quasar is recorded in the spectrograph. The observed wavelength of the light from the quasar become longer than the emitted rest-frame wavelength.

$$z = \frac{\lambda_{Observed} - \lambda_{Emitted}}{\lambda_{Emitted}} \quad (13)$$

The redshift of the quasar is used to determine the distance and look-back time to the observed quasar. We applied the template matching the quasar template from [Selsing *et al.*, 2016] to derive the value of the redshift of our observed samples. Most of the absorption lines in the quasar spectra are caused by intergalactic gas clouds. Therefore instead of absorption lines, we will use the template matching of emission lines to find the redshift of the quasars.

As discussed in section 1.2, 1.3 the quasars have different types of emission lines depending on its type. We picked common emission lines of the composite quasar template from [Selsing *et al.*, 2016]. The most important emission lines for our study are Lyman- α emission line at 1216 Å, SiV at 1393 Å and 1400 Å, CIV at 1548 Å, 1551 Å (in template matching we only applied 1551 Å), CIII] at 1909 Å and MgII at 2798 Å in the plot of template spectrum.

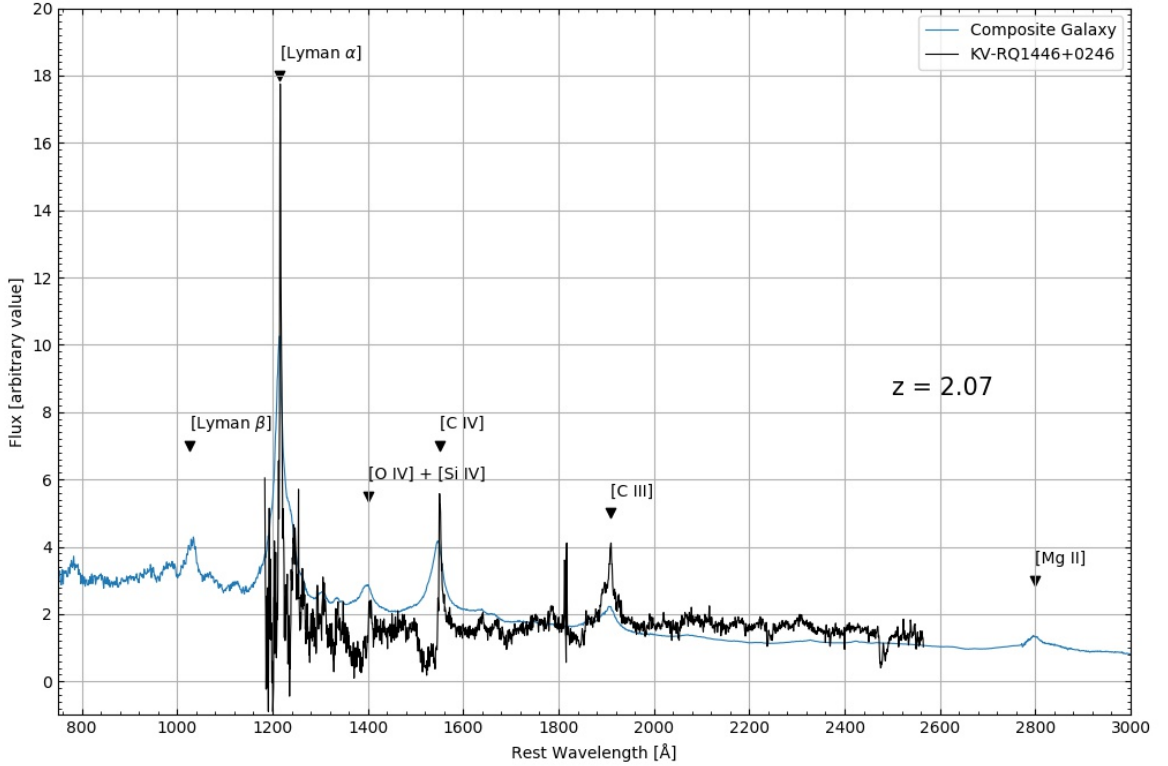


Figure 17: The plot of template matching of BAL KV-RQ1446+0246 and composite quasar from [Selsing *et al.*, 2016]. The flux in the y-axis is arbitrary flux value to scale the sample of quasar with the QSO template and the wavelength in x-axis is the rest wavelength of KV-RQ1446+0246. The rest wavelength is calculated with the redshift equation.

We template matched the sample with the best-fitted redshift value with a variation of 0.01. Therefore, the qualitative uncertainty of redshift is ± 0.01 . This method of deriving the uncertainty is not quantitative as, e.g., in the case of least-square minimisation. The reason why we cannot use a method like that is that there is too much intrinsic variation in the phenomenon so that the deviation between the observed spectrum and the shifted template spectrum is not primarily a question of measurement error. The quasar emission lines can have different shapes, there are velocity shifts between emission lines of several hundreds of km s^{-1} . There can also be variations in other aspects such as the slope of the quasar continuum and the shape of the dust extinction curve. However, we here assume these variations to be small.

To derive the amount of extinction for the dust reddening of the quasar, we used the extinction model of the Small Magellanic Cloud (SMC) with the composite quasar template from [Selsing *et al.*, 2016]. We created the extinction model of the composite quasar template and fitted it into our quasar samples. We assumed that the extinction feature of the quasar is similar to the Small Magellanic Clouds (SMC) and the Large Magellanic Clouds (LMC). The Milky Way, LMC, and SMC are few observable galaxies of observed interstellar extinction curves. The dust model of Milky Way, LMC and SMC have been parameterized in [Pei, 1992]. The Magellanic Clouds resemble galaxies of high redshift. The Magellanic Clouds have lower mass and fewer heavy elements, and they are close to the early chemical stages of galaxies at high redshifts.

$$A_\lambda = A_V \left(\frac{1}{R_V} + 1 \right) \sum_{i=6}^6 \frac{a_i}{\left(\frac{\lambda}{\lambda_i} \right)^{n_i} + \left(\frac{\lambda_i}{\lambda} \right)^{n_i} + b_i} \quad (14)$$

A_λ is the extinction of magnitudes at the wavelength, A_V is the total extinction of the quasar, R_V is total-to-selective extinction ratio of value $R_V = 3.08$ for Milky Way, $R_V = 2.93$ for SMC and $R_V = 3.16$ for LCM. a_i , b_i , n_i and λ_i are analytic extinction curve parameters [Pei, 1992].

Table 1: Analytic Extinction Curve Parameters for the applied dust models ([Pei, 1992]).

Parameter	a_i	$\lambda_i(\mu m)$	b_i	n_i
Milky Way Galaxy				
BGK	165.	0.047	90.	2.0
FUV	14.	0.08	4.00	6.5
2175 Å	0.045	0.22	-1.95	2.0
9.7 um	0.002	9.7	-1.95	2.0
18 um	0.002	18.	-1.80	2.0
FIR	0.012	25.	0.00	2.0
Large Magellanic Cloud				
BGK	175.	0.046	90.	2.0
FUV	19.	0.08	5.50	4.5
2175 Å	0.023	0.22	-1.95	2.0
9.7 um	0.005	9.7	-1.95	2.0
18 um	0.006	18.	-1.80	2.0
FIR	0.020	25.	0.00	2.0
Small Magellanic Cloud				
BGK	185.	0.042	90.	2.0
FUV	27.	0.08	5.50	4.0
2175 Å	0.005	0.22	-1.95	2.0
9.7 Å	0.010	9.7	-1.95	2.0
18 um	0.012	18.	-1.80	2.0
FIR	0.030	25.	0.00	2.0

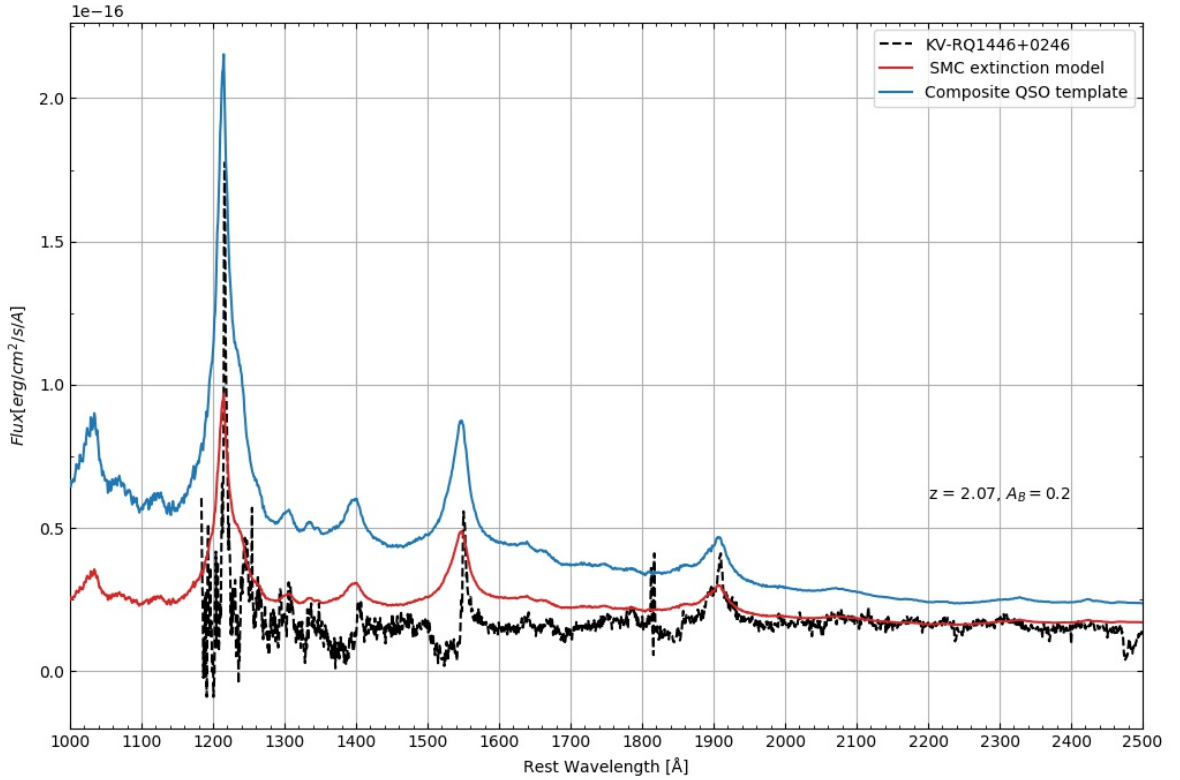


Figure 18: The figure shows BAL KV-RQ1446+0246 as the black dashed line, SMC extinction model of composite template from [Selsing *et al.*, 2016] as the red line, where the blue line is the composite template without extinction.

We defined the extinction of magnitudes at the wavelength of SMC (a few cases of LMC) by using the dust extinction model to our composite template [Selsing *et al.*, 2016]. The value of flux is different for each sample, so we have to normalize the composite template as the same scale of our sample.

We selected the region of quasar wavelength between $\lambda 6900$ to $\lambda 7100$ and measured the mean value of flux of the region. The redshift of our quasar sample is applied to the wavelength of the composite template. We tried to match the same region of the quasar sample and the template spectrum. The wavelength region of template is $\lambda 6900(1+z)$ to $\lambda 7100(1+z)$.

$$Normalized(Flux_{A_{\lambda}Template}) = \frac{Flux_{A_{\lambda}Template}}{Mean(Flux_{A_{\lambda}template_{\lambda 6900(1+z)..7100(1+z)})Mean(Flux_{Quasar_{\lambda 6900..7100}})} \quad (15)$$

The normalized extinction flux is calculated by dividing the mean flux of the extinguished model and mean flux of quasar. We fitted the best extinction model to the quasar spectrum and noted the best matched total extinction of quasar. The variation of extinction value is 0.05. As the redshift, the determination of the uncertainty is subjective (by eye) with an estimated size of ± 0.05 . This uncertainty is not to be used as a formal Gaussian error

estimate, but a rough estimate of the error associated with the template matching. Again, the real uncertainty is probably dominated by other variations in the underlying spectra of quasars and the variation in the extinction curve shapes.

4.2 Fitting of DLA lines

Absorption processes of spectra display information on the physical and chemical properties of the astrophysical environment around the sample. We want to identify the DLA system by investigating the absorption line of neutral hydrogen in our samples. This can happen by investigating the wide of the absorption line. The wide of an absorption line defined as the equivalent width w_{obs} in \AA ,

$$w_{obs} = \int \frac{F_c - F_\lambda}{F_c} d\lambda = \int (1 - e^{-\tau(\lambda)}) d\lambda \quad (16)$$

where F_λ is the observed flux at the wavelength and F_c is the interpolation flux of continuum without any absorption. In our case F_c is the normalized flux continuum of section 3.2. $\tau(\lambda)$ is the optical depth. The equivalent width measures the strength of an absorption line. The area of equivalent width describes the width of the photons in continuum has been absorbed. The quasars are distant objects of high redshift, where the measurement of the observed equivalent width includes redshift,

$$w_{obs} = w_{rest}(1 + z_{abs}) \quad (17)$$

Optical depth is the natural logarithm of the ratio that describes spectral transparency of astrophysical environment,

$$\tau(\lambda) = \int n(l)\sigma(\lambda)dl = N\sigma(\lambda) \quad (18)$$

$n(l)$ is the particle density over the path length l , $\sigma(\lambda)$ is the attenuation cross-section (the probability cross-section of an absorption process) of wavelength. Integral of the particle density over the path length l defines the column density $N = \int n(l)dl$ of absorbing clouds. As we mentioned before, the DLA system is a damped wing system of neutral hydrogen [HI] of column density $N(HI)10^{20}cm^{-2}$. The equation of optical depth is related to the column density of the environment. We can provide the column density of neutral hydrogen by fitting to the equivalent width, by using the optical depth equation and the equivalent width. [Peterson, 1997]

We assume the velocity distribution of the atoms is outline as a Gaussian function, then the shape of the optical depth of width over the absorption line, describes as a Voigt function. The absorption feature is called a Voigt profile, written as $e^{-\tau}$. [Petitjean, 1995]. The Voigt profile describes the physical properties of the absorbing medium as its temperature, and column density. The equation is suited to fit in a single absorption line profile, as the damped wing

system of neutral hydrogen [HI]. The mathematical Gaussian and a Lorentzian distribution function are called Voigt–Hjerting function [Hjerting, 1938] and the function contains a constant factor of physical properties of the absorbing medium. The Gaussian distribution describes thermal Maxwell–Boltzmann velocity distribution of idealized gases of using Doppler b parameter and gas temperature for thermal motions. The Lorentzian distribution describes the quantum absorption cross-section per ion, with the velocity distribution. The profile is dominant of the Gaussian component, as the 'Doppler core' and Lorentzian component appear as extended 'damping wings'. [Peterson, 1997]

The optical depth of Voigt profile considers the probability of photon of an energy $E = \frac{hc}{\lambda}$ is in gas with column density N of kinetic temperature T . The optical depth is given as,

$$\tau(\lambda) = (C_i N a) H[a, x(\lambda)] \quad (19)$$

C_i is a constant for i th electronic transition for photon absorption, a is the damping parameter, H is the Voigt–Hjerting function and $x(\lambda)$ is variable of $x = \frac{\lambda - \lambda_i}{\Delta\lambda_D}$. The variable x is the wavelength position from line center for Doppler width for the distribution. C_i is given by,

$$C_i = \frac{4\sqrt{\pi^3} e^2 f_i}{m_e c \Gamma_i} \quad (20)$$

The constant m_e is the electron mass, f_i is the oscillator strength, e is the elementary charge and Γ_i the damping constant that describes reciprocal of the mean lifetime of the transition.

The Voigt–Hjerting function is given as,

$$H = \frac{a}{\pi} \int_{-\infty}^{+\infty} \frac{e^{-y}}{(x - y^2 + a^2)} dy \quad (21)$$

The variables x is used to the wavelength difference of the resonant wavelength in Doppler units and $y = \frac{v}{b}$ is for the particle velocity v in units of the Doppler parameter. We define the resonant wavelength of the transition as $\lambda_i = \frac{hc}{E_i}$ and thermal Doppler broadening as $\lambda_D = \frac{b}{c} \lambda_i$ of a Doppler unit. The Doppler parameter is $b = \sqrt{\frac{2kT}{m_p}}$ that connect with the kinetic temperature of the gas T , k is the Boltzmann constant and m_p is the proton mass. Those are related to the damping parameter,

$$a = \frac{\lambda_i^2 \Gamma_i}{4\pi c \delta \lambda_D} \quad (22)$$

that describes the relative strength of damping broadening to thermal broadening. By using Voigt–Hjerting function, the equation of optical depth is,

$$\tau(\lambda) = 1.498 \cdot 10^{-2} \frac{N f_i \lambda}{b} H(a, u) \quad (23)$$

We defined the Voigt profile as $e^{-\tau}$. We can now fit the DLA candidate with the Voigt profile by using the equation of the optical depth. Before we are fitting the data with the Voigt profile, we have to find the solution of the Voigt-Hjerting function. The one of the numerical approximation for the Voigt-Hjerting function is,

$$H(a, x) = H_0 - \frac{a}{\sqrt{\pi}x^2} [H_0^2(4x^2 + 7x^2 + 4 + Q) - Q - 1] \quad (24)$$

where $H_0 = e^{-x^2}$ is the zeroth order of the Voigt-Hjerting function and $Q = 1.5x^{-2}$. The approximation is defined in [García, 2006], [Tepper-García, 2007].

We previously mentioned that the equation of observed equivalent width w_{obs} is proportional to the optical depth $\tau(\lambda)$. The equation is 'curve of growth' which describes the relationship of the observed equivalent width w_{obs} , and optical depth $\tau(\lambda)$. The equivalent width grows as the increasing column density of the optical depth. In general, there are three parts in the 'curve of growth', the linear part of the curve, the flat-part of the curve and damping part of the curve.

The linear part is for the optically thin absorption line of the small column density ($\tau < 1$). The equivalent width is independent of the Doppler parameter b , as $W(\lambda_o) \propto \tau_0$. The line is referred to as the unsaturated line. The transition of the column density is given by,

$$N = 1.13 \cdot 10^{20} \frac{w_r(\text{\AA})}{\lambda^2(\text{\AA})f} \quad (25)$$

The flat part is for the transmitted intensity at the line center is almost zero. The photons cannot reach at the center of the line through the absorbing cloud. The equivalent width is strongly dependent on column density N and Doppler parameter b . It is hard to determine the column density N and Doppler parameter b of the flat part, due to the strong dependence on the parameters. The line is referred as the saturated line. The equivalent width and centered optical depth are related as,

$$\frac{w}{\lambda} = 2 \frac{b}{c} \sqrt{\ln(\tau_0)} \quad (26)$$

The damping part is for the optical depth at the line center has a broad wing, which makes the large area of Doppler line to be saturated. Those are called as damping wings, that the only unsaturated part of the line is in the low opacity of damping wing, which is far out of center. The line is independent on the Doppler parameter b , and the equivalent width is dependent on the column density N . The line is referred to as the heavily saturated line. The equivalent width and centered optical depth are related as,

$$\frac{w}{\lambda} = 2.64 \frac{b\sqrt{a}}{c} \sqrt{\tau_0} \quad (27)$$

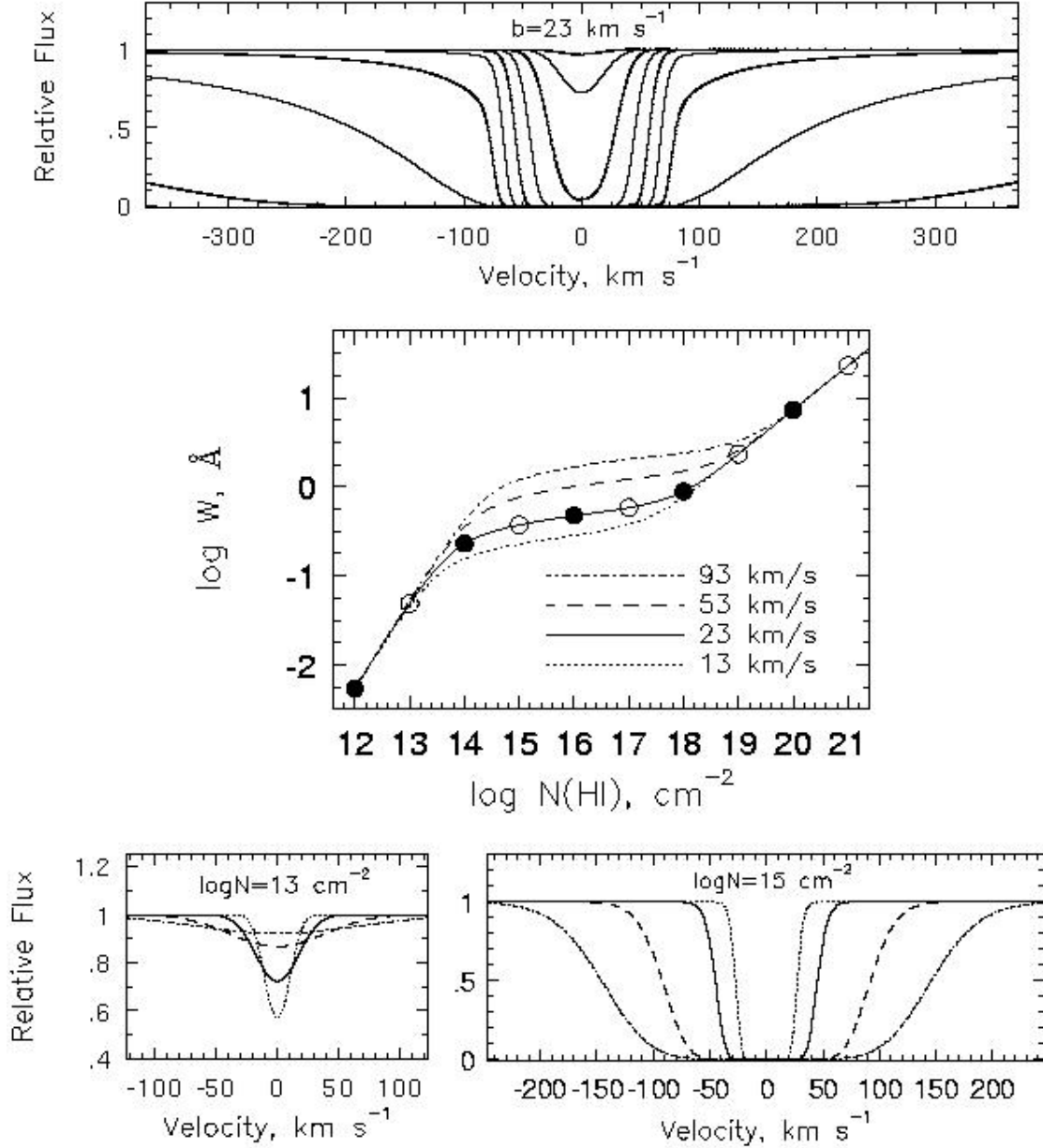


Figure 19: The figure shows the curve of growth for absorption lines of neutral hydrogen. The above figure shows all three different parts of constant Doppler parameters. The middle figure shows parts of the lines. The flat part is the beginning part of the line, which is not affected by Doppler parameter. After the flat part, the line is reaching the flat part and divided into many lines due to the dependent of Doppler parameter b . When lines are reaching at the damping part, the lines are brought back to one line of independent of Doppler parameter b . The figures below show an optically thin case(left) of the line and a damping wing(right). [of Illinois, n.d.]

A DLA is a heavily saturated line of damping wing. It is not strongly dependent on Doppler parameter. We can determine the column density by fitting Voigt profile of $e^{-\tau}$ with equation (23), (24) without strong accuracy of Doppler parameter.

4.3 Quasar classification

In section 2.1 mentioned that the $J - K_S$ versus $g - r$ colour criteria divide the candidates into two groups of the colour, as the red-coloured group and the blue coloured group. Still, the detail identification of candidates is done by spectral analysis. We are interested to identify candidate's colour, its type, BAL or DLA or containing MgII emission line. Most of MgII emission line spectra appear in low redshift quasars of $z < 2$, which should be rejected from the WISE selection. The MgII emission lines are interested in the finding of star activities of the intergalactic medium, so we will also note if the quasar has MgII emission lines.

We also noted the type of quasar by investigating sample's broad/narrow emission lines. The broad emission lines quasar into type 1 and the narrow emission lines quasar into type 2. Type 2 quasars are clouded behind in the dense gas, and it might be interesting to investigate its influence on the quasar selection.

We used the Voigt profile to identify DLA by fitting the best column density value of neutral hydrogen to the candidates with a damping wing. Some of the samples has broad absorption lines in the spectral analysis and we identified those as BAL quasars.

The direct spectral analysis of the sample can be found unwanted/not rejected stellar objects in our samples. Those stellar objects are hard to identify as photometric identification because it has passed the colour criteria to reject stellar objects. The stellar spectra are black body spectra, and they are clearly different from the quasar spectra.

The spectral colour selections are done by comparing the template of QSO with the spectrum of the sample. We plotted the spectrum of the composite template with normalized extinguished scale and redshift of the samples together with the dust extinction model in section 4.1. Some of the sample was highly extinguished so we compared samples with a logarithmic y-axis scale. The method is qualitative comparison.

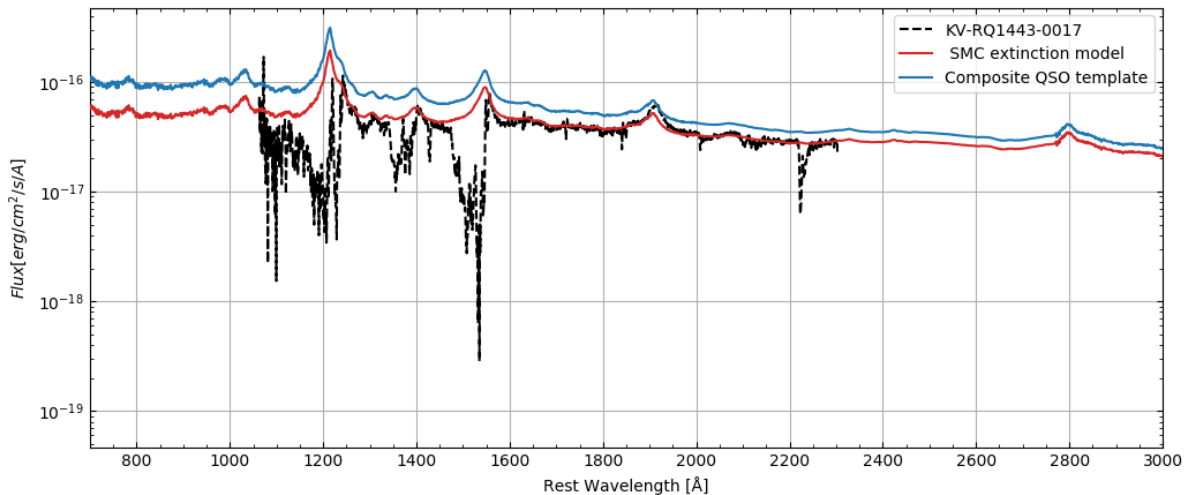


Figure 20: The figure of KV-RQ1443-00172 spectrum. The spectrum has strong absorption lines at short wavelengths. Comparing the composite template, the strength of short wavelength flux is relatively weaker than the normalized composite spectrum. The colour of the sample is red.

4.4 Stellar classification

We classified stars with the photometric comparison of the stellar characterization of SDSS [Fukugita *et al.*, 2011] and spectral comparison of the Morgan-Keenan system (O, B, A, F, G, K, and M) stars.

Table 2: SDSS colours of stars [Fukugita *et al.*, 2011].

Type	u - g	g - r	r - i	Type	u - g	g - r	r - i
B2V	-0.08	-0.50	-0.37	B2III	-0.10	-0.50	-0.35
B7V	0.49	-0.34	-0.25	B7III	0.49	-0.36	-0.26
A0V	0.98	-0.22	-0.19	A0III			
A5V	1.08	-0.04	-0.09	A5III	1.10	-0.07	-0.13
F4V	1.11	0.13	-0.11	F4III			
F9V	0.90	0.37	0.10	F9III			
G0V	1.04	0.34	0.09	G0III			
G2V	1.22	0.43	0.12	G2III			
G5V	1.29	0.48	0.14	G5III			
G8V	1.51	0.62	0.21	G8III	1.86	0.72	0.23
K0V	1.19	0.47	0.15	K0III	2.14	0.84	0.28
K4V	2.06	0.90	0.29	K4III	3.09	1.24	0.43
K7V	2.47	1.34	0.54	K7III			
M0V	2.44	1.41	0.66	M0III	3.16	1.38	0.72
M2V	2.47	1.48	0.92	M2III	3.10	1.57	1.28
M5V	2.29	1.72	2.12	M5III	2.60	1.58	1.89

We compared stellar colours of $u - g$, $g - r$ and $r - i$ in the table above and find the closest stellar types, of those three colours. If the information of colour is not strongly matched at the table above, then we directly observed the stellar spectrum to classifying the star. We compared the spectrum of our objects with spectra from University of Oregon (Department of Physics) (<http://www.eso.org/cguirao/caos/spectralclassification/SpectralClassification.html>). Those are in Appendix.

We mainly used the sodium doublet (Na D) absorption lines at 5890 Å and 5896 Å to identify the stellar objects. Sodium doublet absorption lines are easily observed at cool stars and weakly observed at hot stars. (<https://www.handprint.com/ASTRO/specclass.html> and <https://www.chem.uci.edu/unicorn/249/Handouts/RWFSodium.pdf>)

4.5 The classification/identification of the samples

The photometric colour selection has a goal to sort out stellar objects from quasar samples. The main motivation of those colour selection is to select red quasars of redshifts above $z \geq 2$, where DLA systems are found in $z \geq 2$. The dusty objects as DLA and red quasars easily resemble as the stellar spectra, and often biased in the classical selections as $u - g$ versus $r - i$ selection. Finding the DLA systems in samples is important because it is often missing in the classical selection of its reddening.

As mentioned in section 2.1, we used $g - r$ versus $r - i$ selection to include the reddest sources in the optical selection. $g - r$ versus $J - K_S$ selection to find blue/red quasars and re-

jecting the stellar objects. $W1 - W2$ versus $W2 - W3$ selection to reject the quasars below $z \leq 2$.

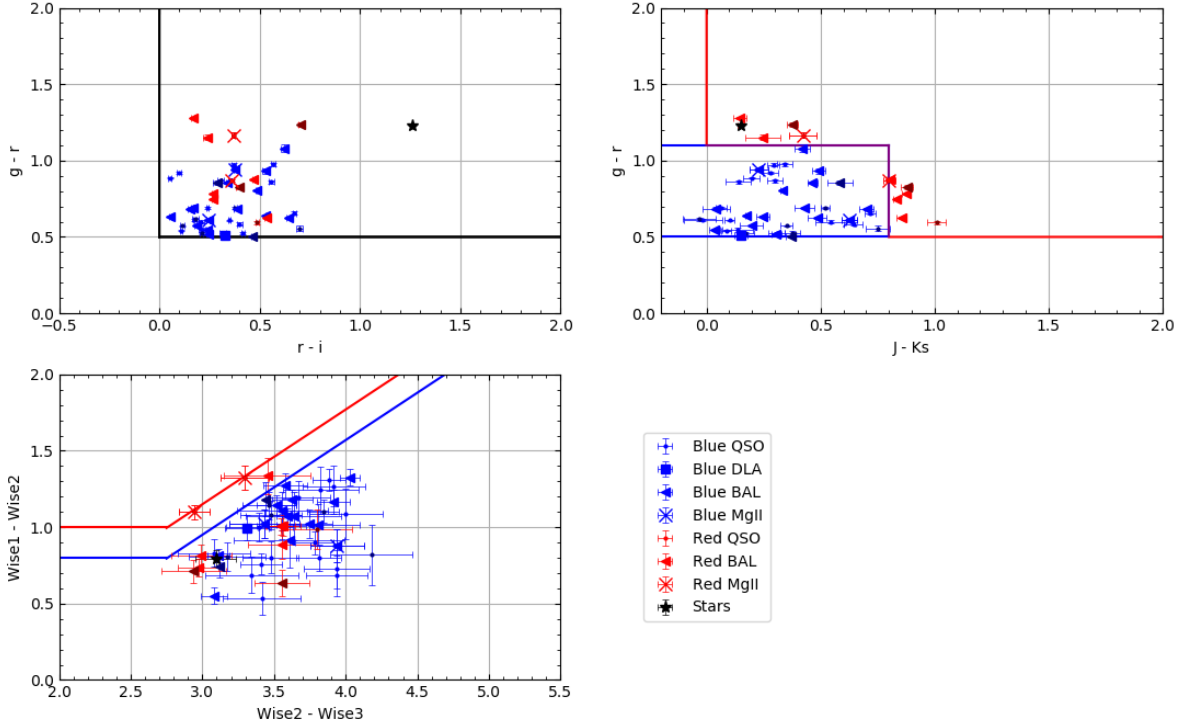


Figure 21: Three colour-colour diagrams of KV-RQ samples. Each colour represents the colour of quasars (blue quasars as blue colour, red quasars as red colour) and dark blue/ red colours marked as the type 2 (narrow and dusty emission line) quasars. The black star signs are the marks for stellar objects. The dot markers are ordinary quasars of non-DLA or BAL population. The square markers are DLA quasar population, where the triangle markers are BAL quasar populations. The x markers are quasars that contain MgII emissions. $r - i$ versus $g - r$ selection is on the above left. The black line of $g - r$ versus $r - i$ selection to collect the most redder sources. $g - r$ versus $J - K_S$ selection is on the above right. The red line is the colour criteria for the red quasar population, where the blue line is the colour criteria for the blue quasar population. $W1 - W2$ versus $W2 - W3$ selection is on the below left.

Type 2 narrow emission quasars seems to be redder than type 1 quasars. Type 2 quasars are marked as the dark-coloured objects in Figure 21. In $g - r$ versus $J - K_S$ colour diagram, the group of type 2 quasars moves at the high numbers of $g - r$ versus $J - K_S$ colours. The samples of type 2 quasars are few, the evidence of type 2 quasars is redder than type 1 quasars are not in the confidence.

The colour-colour diagrams show most of the red selected quasars are BAL quasars. The distribution of BAL quasars are well distributed around colours, that BAL quasars appear also often in blue colour selection.

We defined KV-RQ1500-0013, KV-RQ2305-3034 and KV-RQ2316-2949 as DLA systems through fitting with the Voigt profile. KV-RQ1500-0013 has relatively high extinction where KV-RQ2305-3034 and KV-RQ2316-2949 have high redshift. All of them are classified as blue

objects within colour criteria of $g - r$ versus $J - K_S$ selection.

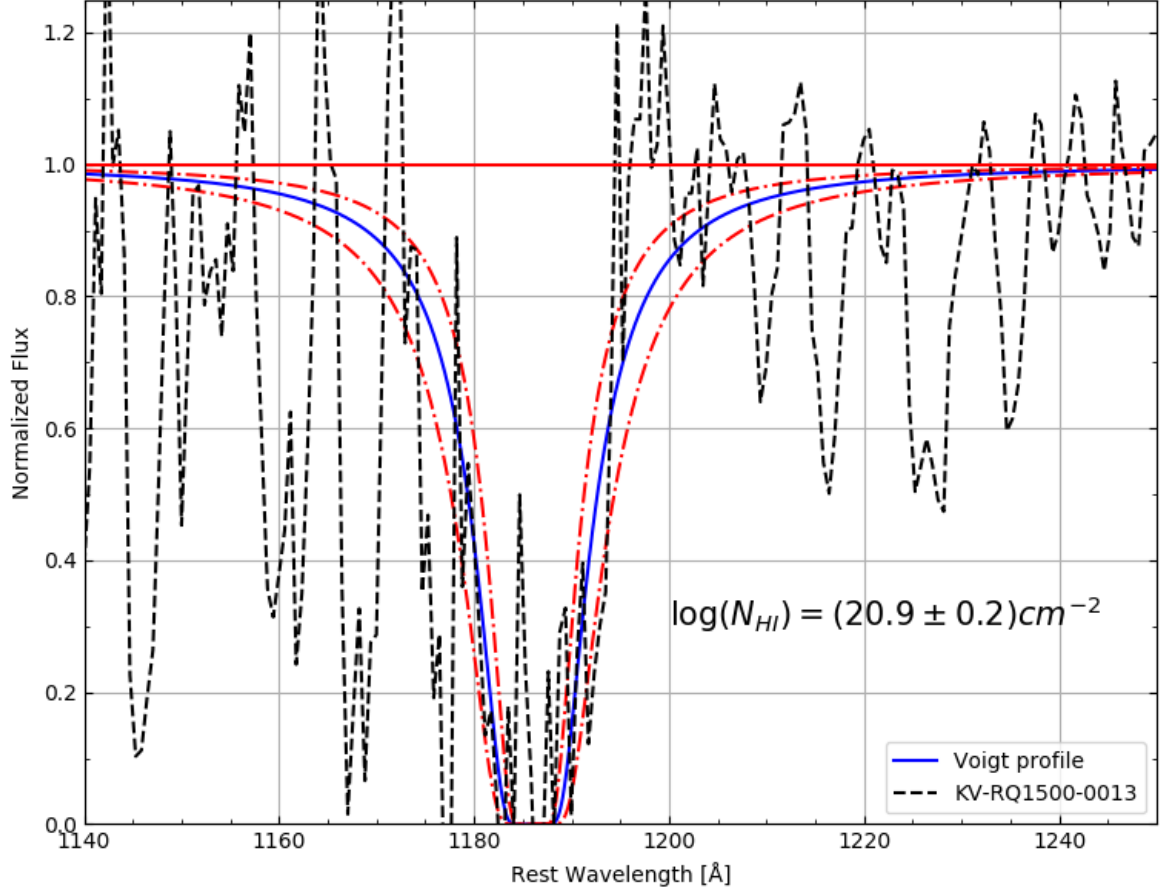


Figure 22: The Voigt profile of $\log(N_{HI}) = (20.9 \pm 0.2)cm^{-2}$ fitted in the normalized spectrum of KV-RQ1500-0013. Fitting with the Voigt profile $e^{-\tau}$ shows KV-RQ1500-0013 is the DLA system quasar. The red striped line is the Voigt profile of the lowest/highest errorbar. We noted that the neutral hydrogen absorption lines lie together with other absorption and emission lines that make it hard to determine the exact value of N_{HI} . The line of damping wing seems to appear bigger flux due to the normalization of the data.

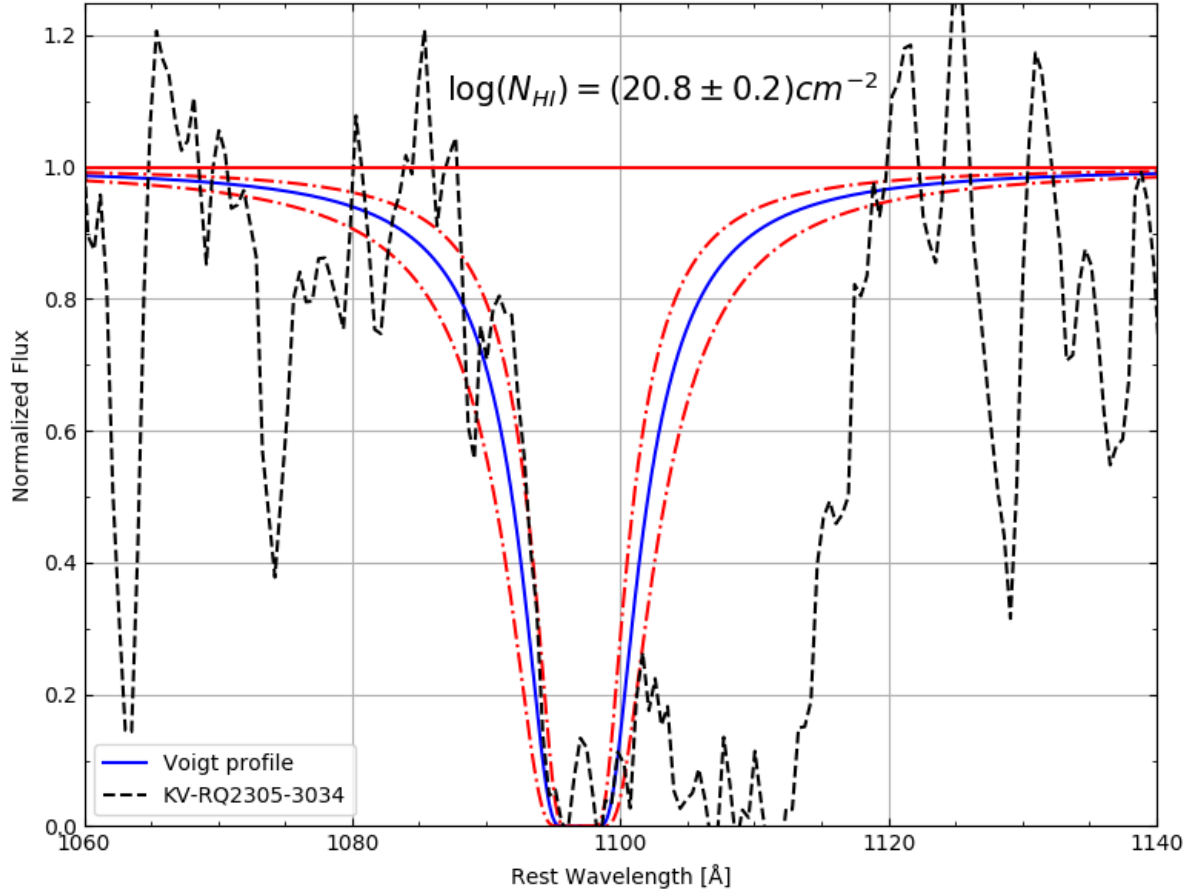


Figure 23: The first Voigt profile of $\log(N_{HI}) = (20.9 \pm 0.2)cm^{-2}$ fitted in the normalized spectrum of KV-RQ2305-3034. We found the quasar contains two DLAs in the spectrum. Absorption lines of FeII at 1608 Å and AlIII at 1670 Å are found in the redshift of 3.063 and 3.017. The line of damping wing seems to appear bigger flux due to the normalization of the data.

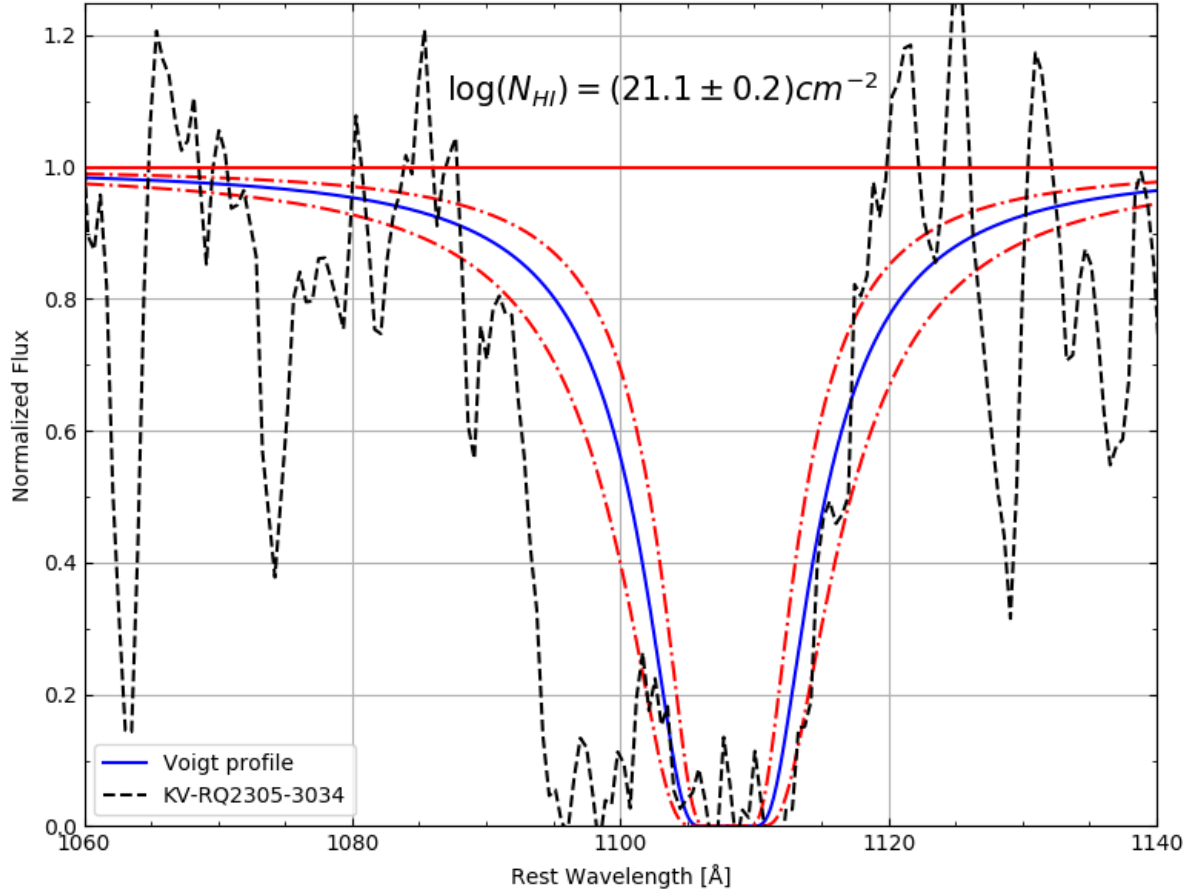


Figure 24: The second Voigt profile of $\log(N_{HI}) = (20.9 \pm 0.2)cm^{-2}$ fitted in the normalized spectrum of KV-RQ2305-3034. The peak of the left is over the continuum. The flux has been bigger by the normalization.

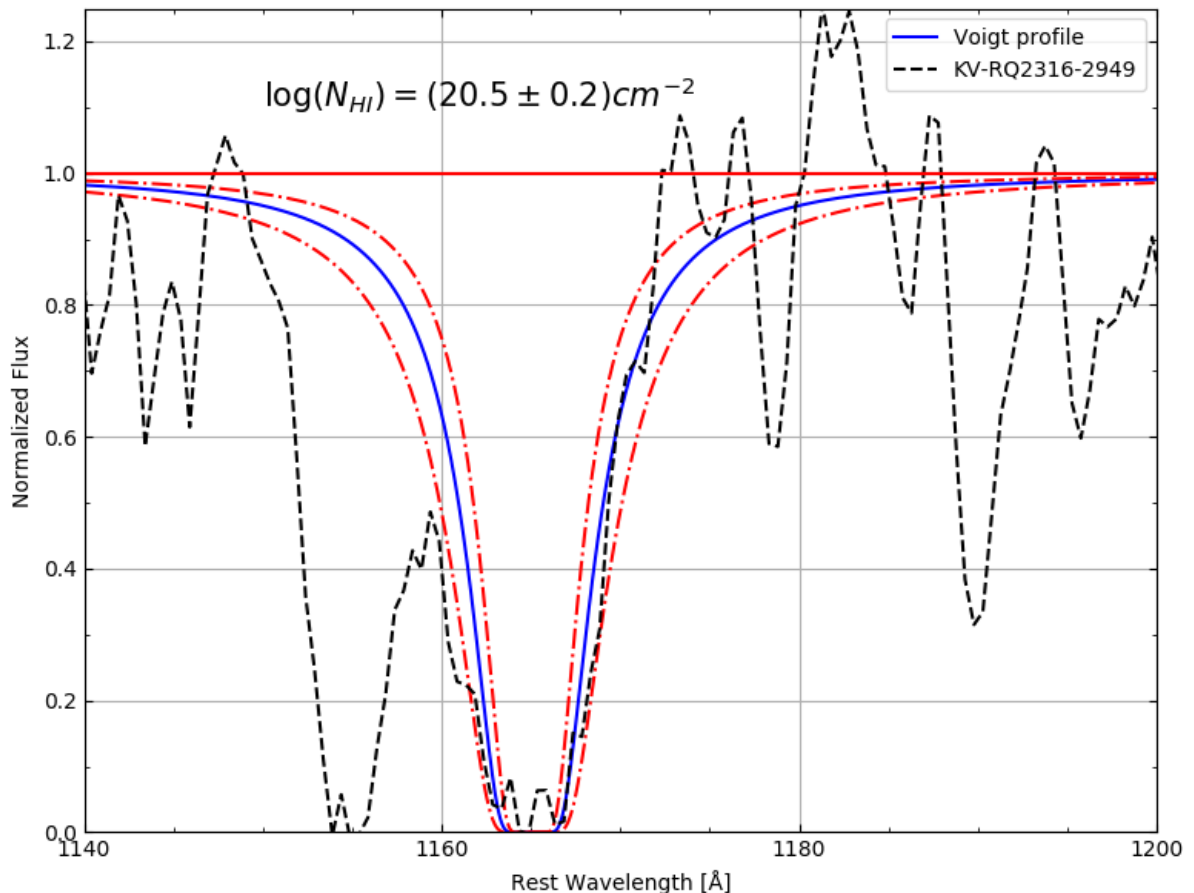


Figure 25: The Voigt profile of $\log(N_{HI}) = (20.5 \pm 0.2)cm^{-2}$ fitted in the normalized spectrum of KV-RQ2316-2949. There are other absorption lines close to the neutral hydrogen absorption line.

Our DLA samples have another emission/absorption lines around the HI absorption line. Those other lines lie together with our Voigt profile, which makes it hard to determinate the exact value of the N_{HI} . We chose the best-fitted value of Voigt profile with uncertainties of the qualitative lowest/highest values of the Voigt profile. We believe those other lines are from the intergalactic gases of low redshifts. An error of the normalization of data may effecting the determination of the exact value of the N_{HI} . The detail is written in the section 5.3

Table 3: DLA systems in KV-RQ colour selection

Name	$\log(N(HI)) \text{ cm}^{-2}$	Redshift	Redshift of DLA	Extinction
KV-RQ1500-0013	(20.9 ± 0.2)	2.52 ± 0.01	2.434 ± 0.001	0.2 ± 0.05
KV-RQ2305-3034 1	(20.8 ± 0.2)	3.45 ± 0.01	3.017 ± 0.001	0.00 ± 0.05
KV-RQ2305-3034 2	(21.1 ± 0.2)	3.45 ± 0.01	3.063 ± 0.001	0.00 ± 0.05
KV-RQ2316-2949	(20.5 ± 0.2)	3.15 ± 0.01	2.977 ± 0.001	0.05 ± 0.05

The value of extinction is A_B (the total extinction of B bands).

KV-RQ0841-0058, KV-RQ0847+0012, KV-RQ0855-0143, and KV-RQ2242-3219 found as MgII emission quasars by investigating spectra of quasars,

Table 4: MgII emission quasars in KV-RQ colour selection

Name MgII	Colour	Redshift	Extinction
KV-RQ0841-0058	Blue	2.32 ± 0.01	0.55 ± 0.05
KV-RQ0847+0012	Red	1.45 ± 0.01	0.20 ± 0.05
KV-RQ0855-0143	Red	1.22 ± 0.01	0.70 ± 0.05
KV-RQ2242-3219	Blue	1.68 ± 0.01	0.40 ± 0.05

MgII emission quasars found in both red and blue selection. Those MgII emission quasars have relatively low redshift and high extinction. We mentioned at previous sections, that the dust formation is a sign of star formation. This might be an evidence to that MgII emission quasars have a high chance to contain star formation activities.

We noted that one stellar object was not rejected after the colour rejection. It is a KV-RQ1445+0204. We tried to match the closest photometric data of SDSS to the object.

Table 5: Stellar objects in KV-RQ colour selection

Name	Type	RA(deg)	DEC(deg)	u - g	g - r	r - i
KV-RQ1445+0204	GV	221.412789	2.067483	1.545 ± 0.080	0.732 ± 0.012	0.348 ± 0.015

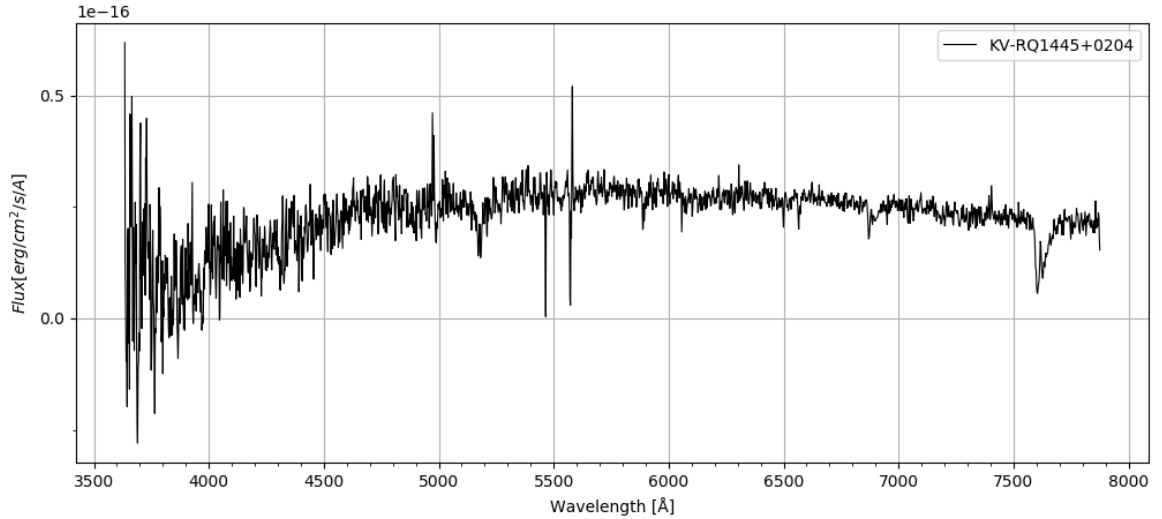


Figure 26: The figure of KV-RQ1445+0204 spectrum. The spectrum is blueshifted. The spectrum has the sodium doublet blueshifted wavelength at the 5465 Å and 5570 Å. We found G band near 3970 Å. The spectrum has noises at wavelength range around from 3600 Å to 4100 Å.

The most closest photometric data of SDSS is the GV8 main-sequence star of $u - g = 1.51$, $g - r = 0.62$ and $r - i = 0.21$. The colour of the sample is relatively redder than the SDSS main-sequence star. The spectrum of KV-RQ1445+0204 resembles to the G main-sequence.

We suspect the stellar object is a GV8 main-sequence star.

Some of the samples are rejected by the spectroscopic investigation. Those are KV-RQ1156-0212, KV-RQ1157-0039, KV-RQ1415+0154, KV-RQ1434-0238 and KV-RQ1444+0257. They are once classified as stellar objects/unknown objects in the KV-RQ photometric catalogue. The spectra of those samples are weak and hard to recognise its emission lines. The details are in the discussion in section 5.2.

4.6 $g - r$ versus $r - i$ diagram

We divided the colour-colour diagrams into redshift of $0 \leq z < 1$, $1 \leq z < 2$, $2 \leq z < 3$ and $3 \leq z$ after selection of colour criteria. This process is also done for extinction as $A_B = 0.00$, $0.00 < A_B \leq 0.25$, $0.25 < A_B \leq 0.50$ and $0.50 < A_B$. The main purpose of the division of colour diagrams are to investigate the redshift and extinction influence of colour selection. $g - r$ versus $r - i$ colour-colour diagrams has the purpose to include the reddest most sources in the optical selection

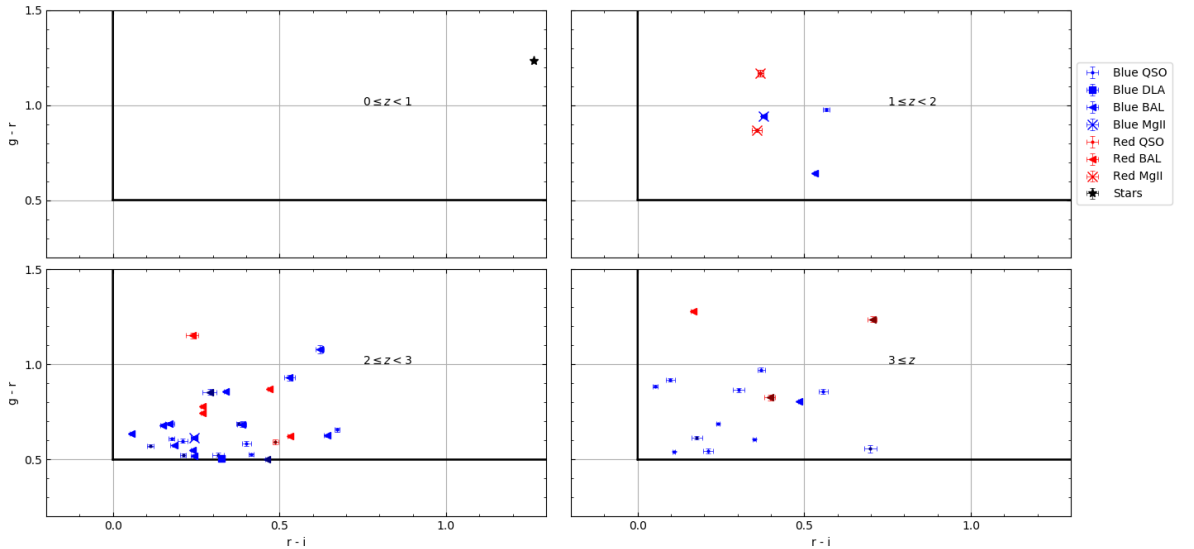


Figure 27: $g - r$ versus $r - i$ colour selection divided into redshifts of $0 \leq z < 1$ above left, $1 \leq z < 2$ above right, $2 \leq z < 3$ below left and $3 \leq z$ below right.

The colour-colour diagrams of Figure 27 show that the object below redshift 1 is the stellar object. The blue objects have low colour index for both axis. The red objects in $g - r$ versus $r - i$ colour selection has more high colour index (redder colour index) of $g - r$ versus $r - i$ diagrams. The most red population (exclude stellar objects) in this $g - r$ versus $r - i$ colour selection is the BAL population. Type 2 BAL KV-RQ1448+0222 has highest $r - i$ colour index 0.704 ± 0.0133 . Type 1 BAL KV-RQ2259-3111 has highest $g - r$ colour index of 1.281 ± 0.006 .

Few of not-rejected low redshift quasars are appeared at redshift between $1 \leq z < 2$. Most of KV-RQ samples are found in the redshift between $2 \leq z < 3$ and some samples at the redshift above $3 \leq z$.

As the Figure 27, the samples are distributed at different redshift. The redshift does not have any visible influence of colours in this selection.

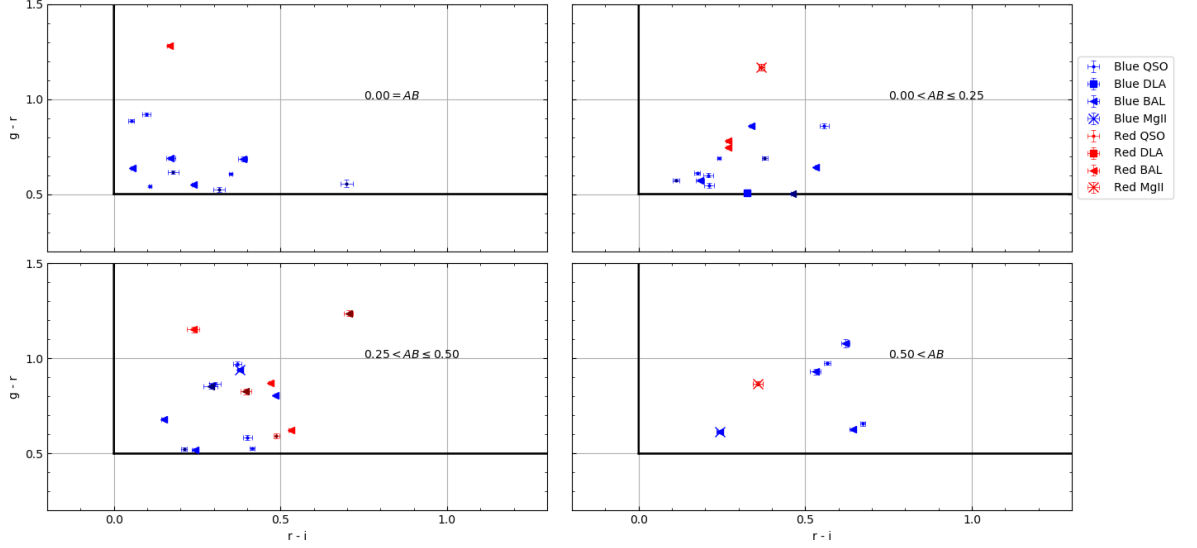


Figure 28: $g - r$ versus $r - i$ colour selection divided into extinctions of $A_B = 0.00$ above left, $0.00 < A_B \leq 0.25$ above right, $0.25 < A_B \leq 0.50$ below left and $0.50 < A_B$ below right.

The most of samples are found at the extinction below 0.50. There is only one photometric red object in $A_B = 0$. The photometric blue objects have various range value of the extinction. The most extinguished sample is DLA KV-RQ1146+0234 of 0.80. The Figure 28 suggests that typical extinguished objects $0.25 \leq A_B$ are BAL and DLA quasars.

The extinction of $g - r$ versus $r - i$ colour displays to be influenced at the $r - i$ colour index. High extinction samples tend to have a high number of $r - i$ colour index. In Figure 28 the group of samples moves to left (high $r - i$ colour index) as the number of extinction increases.

4.7 $g - r$ versus $J - K_S$ diagram

$g - r$ versus $J - K_S$ colour selection has the purpose to divide objects as blue or red colour objects.

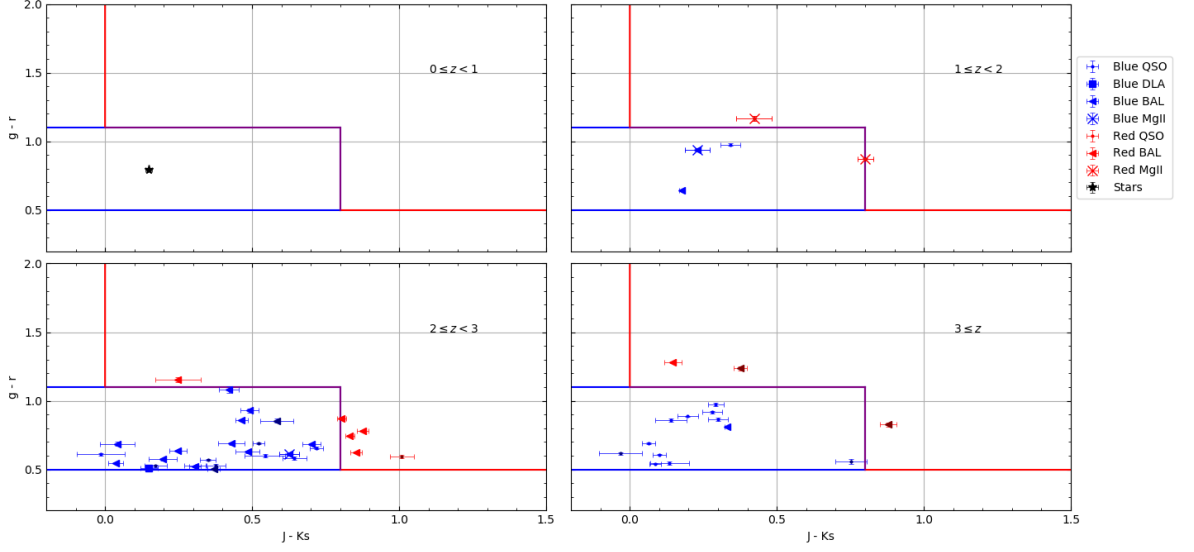


Figure 29: $g - r$ versus $J - K_S$ colour selection divided into redshifts of $0 \leq z < 1$ above left, $1 \leq z < 2$ above right, $2 \leq z < 3$ below left and $3 \leq z$ below right. The blue lines refer to blue colour criteria, the red lines refer to red colour criteria. The violet lines are the boundaries of both blue and red colour criteria.

BAL populations are dominant objects inside the red colour criteria. The colour distribution of BAL quasars are distributed at both of the red and blue colour criteria in the $g - r$ versus $J - K_S$ colour selection. The DLA systems are positioned in the blue criteria. Still, this result does not mean to be that all DLA systems in the samples are blue objects. The details are discussed in Section 5.1. Type 2 quasar population seems to be relatively redder than type 1 quasar population. A stellar object lies inside the blue colour criteria.

As the $g - r$ versus $r - i$ colour selection, redshift does not have any visible influence of colours in this selection.

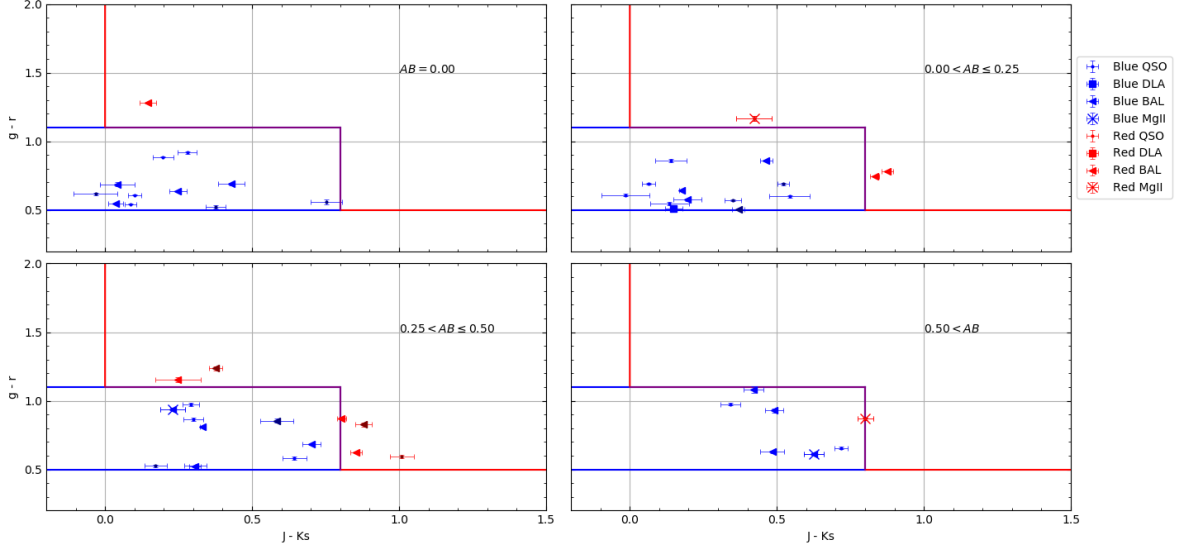


Figure 30: $g-r$ versus $J-K_S$ colour selection divided into extinctions of $A_B = 0.00$ above left, $0.00 < A_B \leq 0.25$ above right, $0.25 < A_B \leq 0.50$ below left and $0.50 < A_B$ below right.

As the $g-r$ versus $r-i$ colour selection, the extinction of $g-r$ versus $J-K_S$ colour appears to be influence at the $J-K_S$ colour index. The influence is not visible as $g-r$ versus $r-i$ colour selection in Figure 30.

4.8 $W1-W2$ versus $W2-W3$ diagram

$W1-W2$ versus $W2-W3$ colour selection has the purpose to reject the population of redshift below 2.

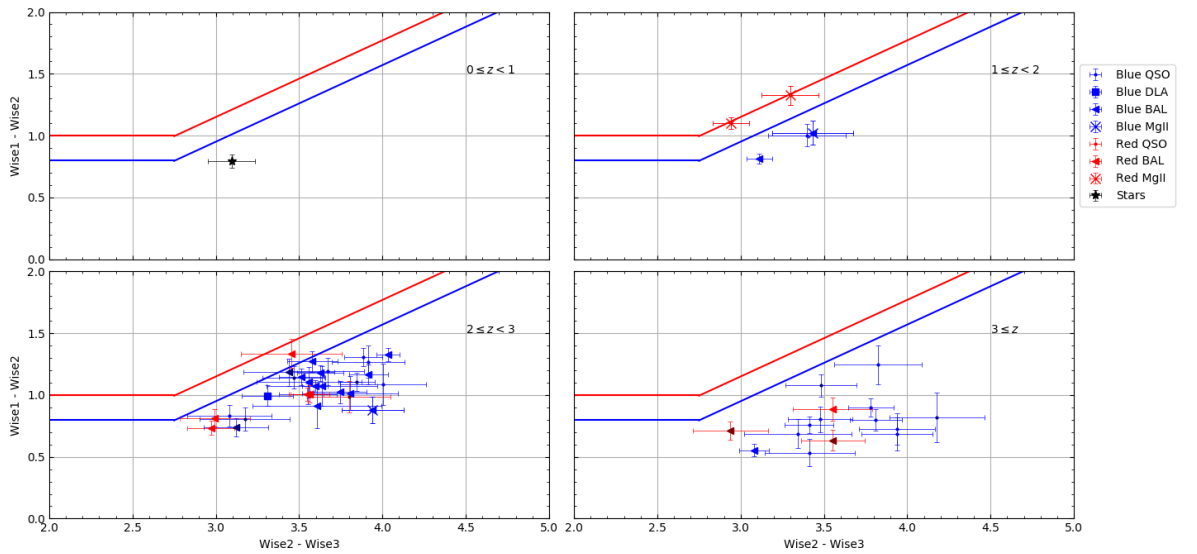


Figure 31: $W1-W2$ versus $W2-W3$ colour selection divided into redshifts of $0 \leq z < 1$ above left, $1 \leq z < 2$ above right, $2 \leq z < 3$ below left and $3 \leq z$ below right. The blue lines refers to blue colour criteria, the red lines refers to red colour criteria.

In Figure 31 the objects does not rejected in redshift $0 \leq z < 1$ and $1 \leq z < 2$ after the rejection of low redshift WISE criteria. Those objects are close to the colour limitations. In general, the WISE colours have large uncertainties than other colours. Some of the errorbars are close to the colour limitations.

Red objects gather at relatively low values of $W2 - W3$ colour index, where the blue objects appears to be at relatively high values of $W2 - W3$ index.

The redshift of $W1 - W2$ versus $W2 - W3$ colour selection has a visible influence on the samples. The group of high redshift objects has a high W2W3 colour index and low $W1 - W2$ colour index. In Figure 31 the group of objects moves at the below left in the colour diagram, proportional to redshift.

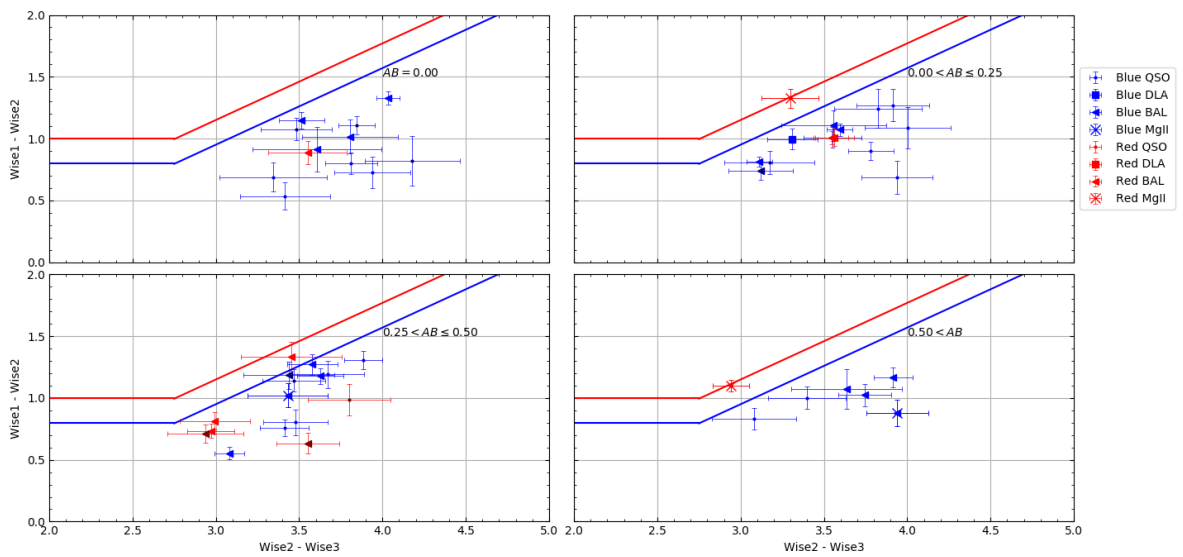


Figure 32: $W1 - W2$ versus $W2 - W3$ colour selection divided into extinctions of $A_B = 0.00$ above left, $0.00 < A_B \leq 0.25$ above right, $0.25 < A_B \leq 0.50$ below left and $0.50 < A_B$ below right.

Unlike the other two colour criteria, the extinction does not have any visible influence of the $W2 - W3$ versus $W1 - W2$ colour selection.

5 Discussion

5.1 Colour criteria

In section 4.5, the DLA systems are selected as photometric blue objects. This is the result of photometric $g-r$ versus $J-K_S$ colour selection. The colour selection has defined those objects as blue colour objects. After several spectral observations of samples, we found that there are few spectral red objects in blue selection. Those are KV-RQ1143-0118, KV-RQ1146+0234, KV-RQ1500-0013, KV-RQ2242-3219, and KV-RQ2306-3312.

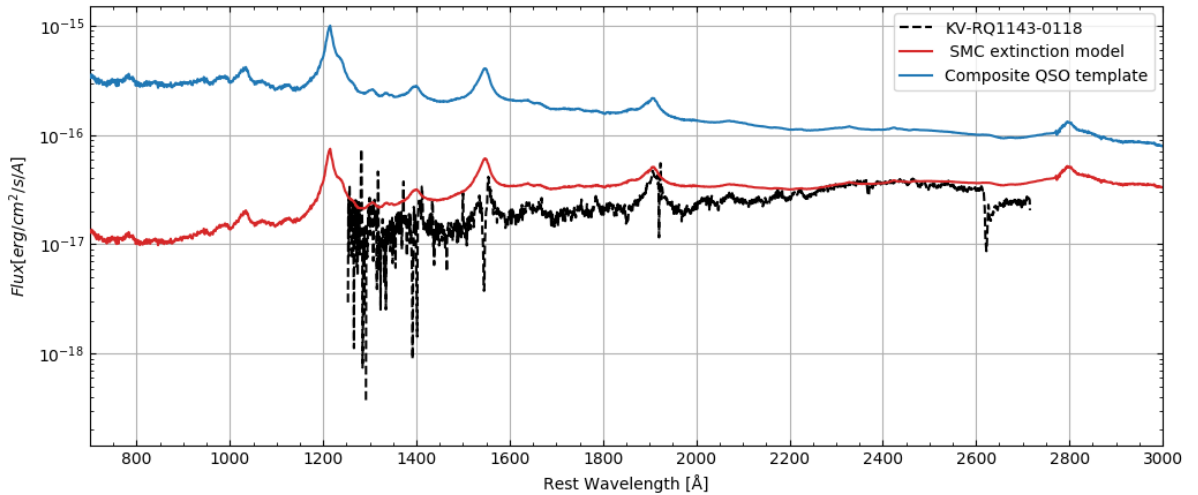


Figure 33: The figure shows KV-RQ1143-0118 as the black dashed line, SMC extinction model of composite template from [Selsing *et al.*, 2016] as the red line, where the blue line is the normalized composite template without extinction. The y-axis is the logarithmic scale of \log_{10} . The reason for logarithmic scaling is to compare non-extinction template to extinguished model of SMC of the high extinction. Remark those plots are in log scale and the model is shifted to the red wavelength compared to the normalized composite template.

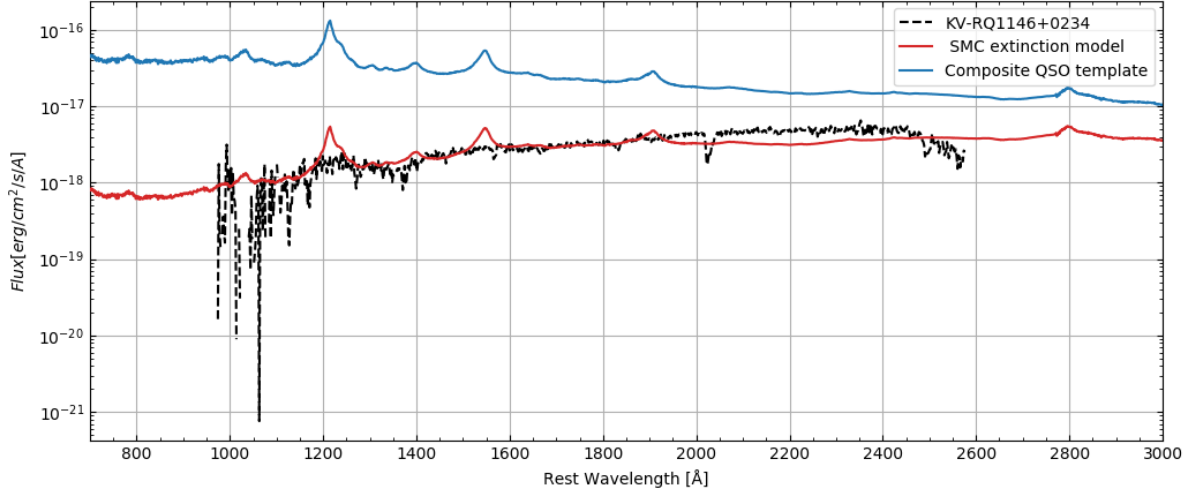


Figure 34: The figure of the KV-RQ1146+0234 spectrum. The y-axis is the logarithmic scale of \log_{10} . This DLA spectra display clearly that dominant flux is in red wavelength. The parts of flux between wavelength 1950 Å to 2480 Å exceeded the SMC extinction model. This figure shows one of the DLA object is a red object in spectral analysis, which has classified as a blue colour object by the photometric analysis.

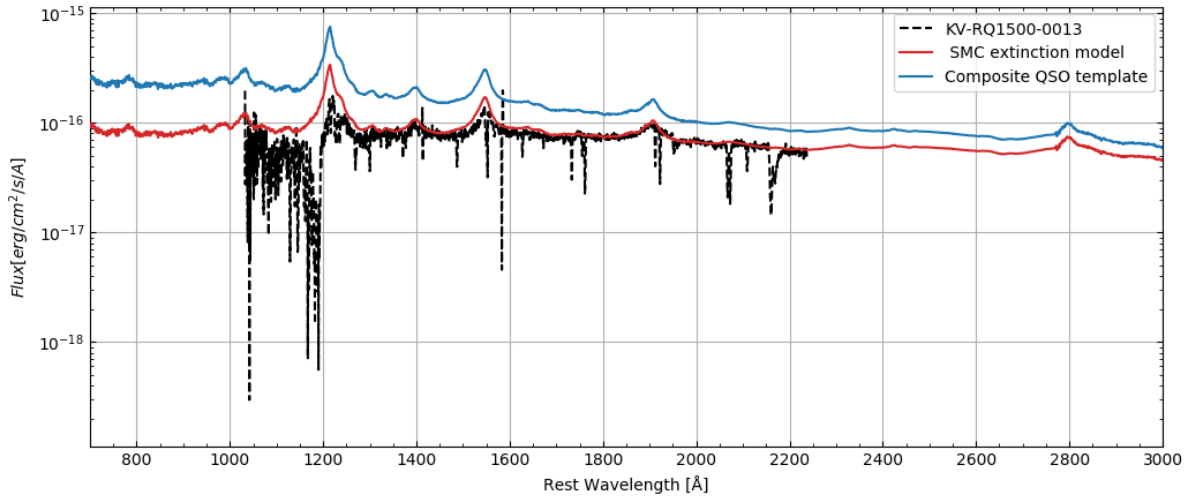


Figure 35: The figure of DLA KV-RQ1500-0013 spectrum. In [Heintz *et al.*, 2018] refers KV-RQ1500-0013 as a dusty reddened object of absorbed flux. The figure displays strong absorption in the blue wavelength. KV-RQ1500-0013 is behind in two dusty absorbers, that caused to escape the optical selection as SDSS. Note in Figure 5, KV-RQ1500-0013 is close to the main sequence stellar population in $u - g$ versus $g - r$ selection.

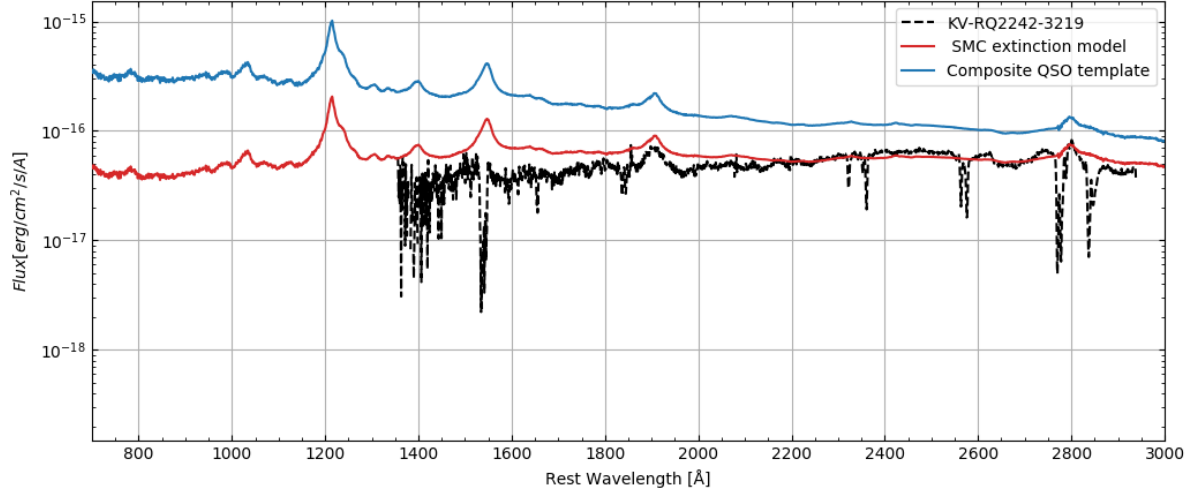


Figure 36: The figure of BAL KV-RQ2242-3219 spectrum of the MgII emission line. The spectrum has lack of hydrogen emission lines. As KV-RQ1146+0234, the parts of flux between wavelength 2200 Å to 2760 Å exceeded the SMC extinction model. The plot is displayed in log scale, and the highest emission lines are within the red wavelength.

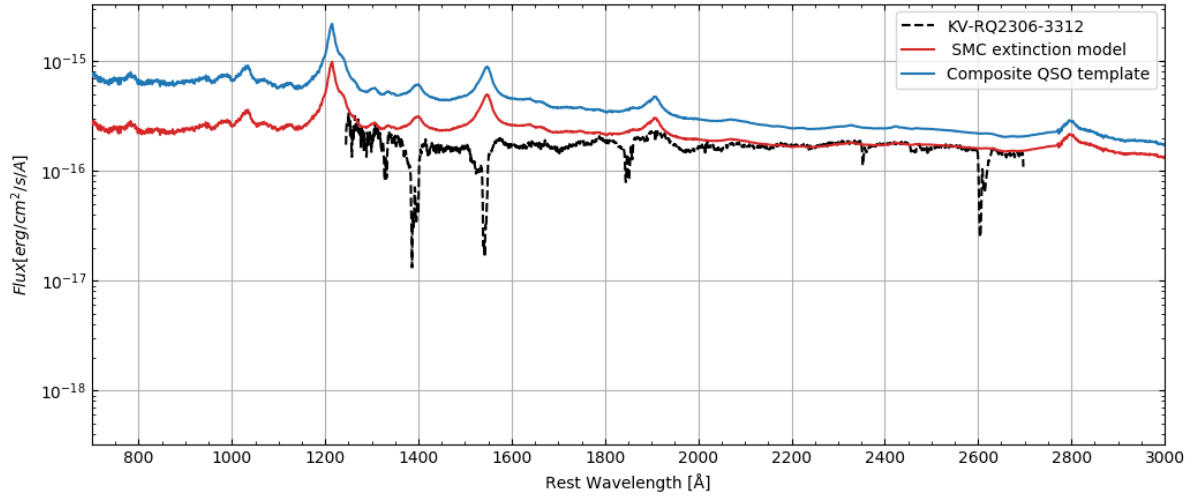


Figure 37: The figure of the BAL KV-RQ2306-3312 spectrum. The line of flux is general flat over wavelengths. The objects can be blue or red depending on the qualitative classification. In this analysis, we defined it as a red object, by its lack of hydrogen emission lines and abortion lines of short wavelengths.

The spectral analysis of the above figures, KV-RQ1143-0118, KV-RQ1146+0234, KV-RQ1500-0013 and KV-RQ2242-3219 display the objects are red objects within photometric $g-r$ versus $J-K_S$ blue classification. Two objects are DLA and two other objects are BAL quasars.

Table 6: Red objects in blue colour criteria.

Name	$g - r$	$J - K_S$	Redshift	Extinction
KV-RQ1143-0118	0.976 ± 0.010	0.976 ± 0.010	1.90 ± 0.01	0.65 ± 0.05
KV-RQ1146+0234	0.627 ± 0.007	0.485 ± 0.041	2.76 ± 0.01	0.80 ± 0.05
KV-RQ1500-0013 (DLA)	0.508 ± 0.005	0.149 ± 0.029	2.52 ± 0.01	0.20 ± 0.05
KV-RQ2242-3219 (BAL MgII)	0.940 ± 0.009	0.230 ± 0.042	1.68 ± 0.01	0.40 ± 0.05
KV-RQ2306-3312 (BAL)	0.642 ± 0.002	0.176 ± 0.007	1.92 ± 0.01	0.30 ± 0.05

Those relative red objects have dusty extinctions of minimum $0.20 \leq A_B$. This may be a sign that all those red objects in blue selection are dusty reddened objects. Those objects are often missed by traditional selection as SDSS, where our main purpose of this thesis is to select those kinds of reddened objects. Some of those reddening might come from photometric redshift extinction.

In the case of the red photometric selection, the blue spectral objects were not found in the red selection method. All of the red objects are selected as photometric and spectroscopic red objects.

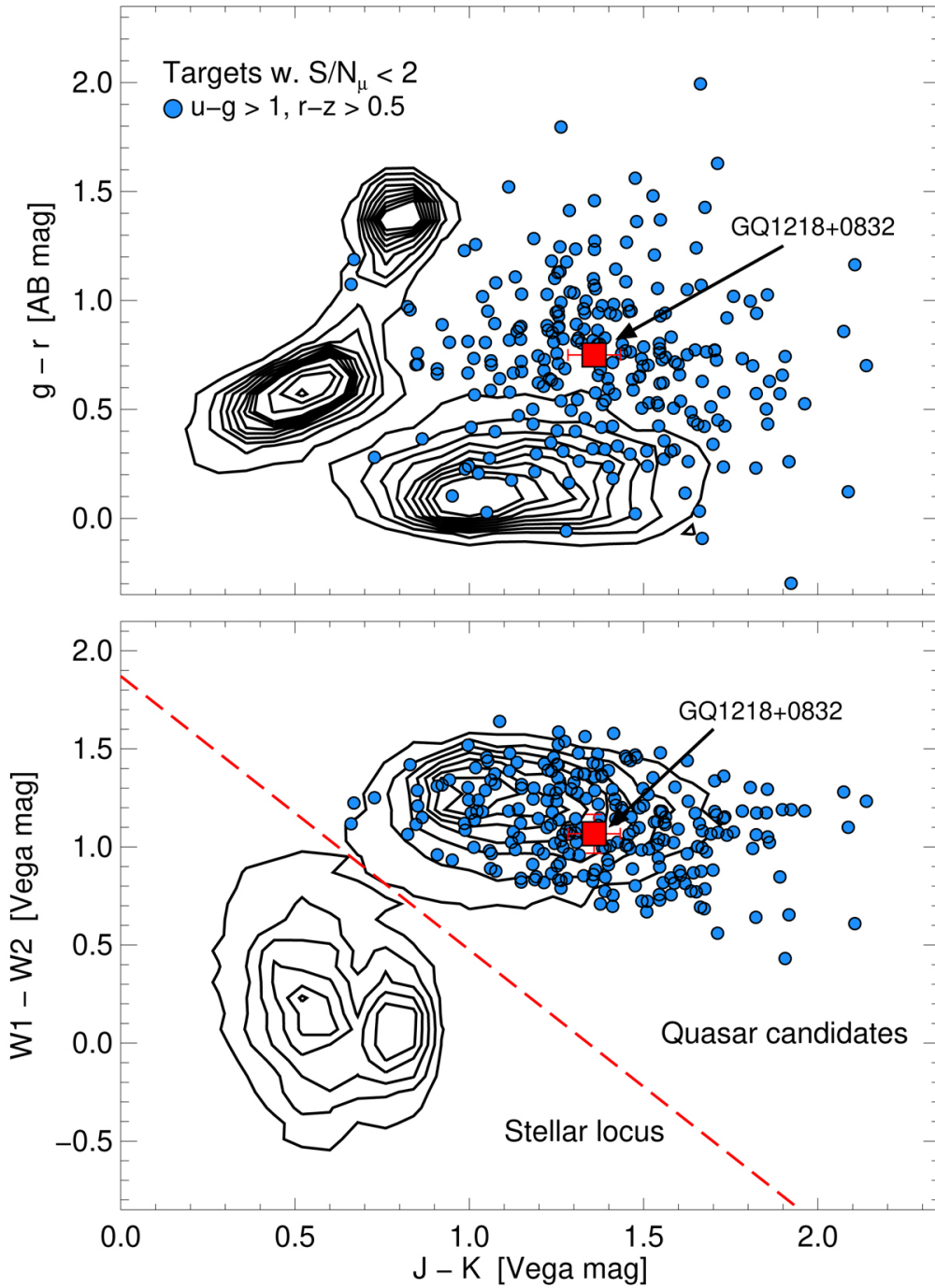


Figure 38: The colour-colour diagram from above displays the SDSS $g-r$ versus UKIDSS $J-K$ colours, and the diagram below displays the WISE $W1-W2$ vs. UKIDSS $J-K$ colours. In [Geier *et al.*, 2019], the colour selection of the optically red objects is done by $u-g > 1$ and $r-z > 0.5$ colour selection. Those selected objects are marked as blue dot, where the contour plot displays optical and near-infrared point sources at the sky of Galactic latitude $b > 60deg$ [Geier *et al.*, 2019].

In comparison of [Geier *et al.*, 2019], the colour-colour diagram of SDSS $g-r$ versus UKIDSS $J-K$ colours in Figure 38 selected the optically red objects below $g-r < 0.5$. Their colour criteria is $u-g > 1$ and $r-z > 0.5$, which displays some of normal quasars are below our colour selection. The comparison of [Geier *et al.*, 2019] and our colour criteria suggests that our photometric blue and spectral red objects may be relatively blue objects comparing to our photometric red objects.

We discussed that WISE colour criteria have a purpose to remove low redshift quasars. Still, some of samples of redshift below $z < 2$ are selected after WISE colour criteria. In Section 4.4 mentioned those objects are close to the limitation of colours and some of them have high uncertainties, which exceeds the limitation. Still, few of them are in the WISE colour limitation including their errorbars. Those are KV-RQ0847+0012, KV-RQ0848+001(Missing spectra data), KV-RQ0855-0143, KV-RQ2242-3219 and KV-RQ2306-3312.

The spectral analysis of those samples showed all of them are red objects in the spectral classification. KV-RQ2242-3219 and KV-RQ2306-3312 are classified as red spectral objects in the blue limitation of MgII lines, where KV-RQ0847+0012 and KV-RQ0855-0143 are photometric red objects. The spectral data of KV-RQ0848+0017 is missing.

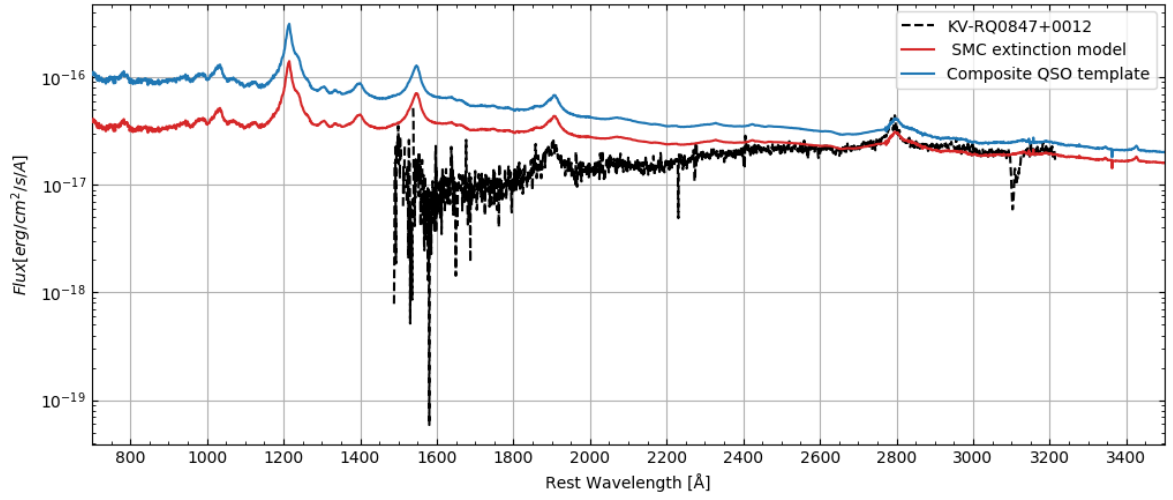


Figure 39: The figure of photometric red KV-RQ0847+0012 spectrum of emission line of MgII. KV-RQ0847+0012 has a lack of hydrogen lines and displays the emission lines of C IV, C III, and MgII elements. Those elements are suspected to be an intergalactic gas of low redshift.

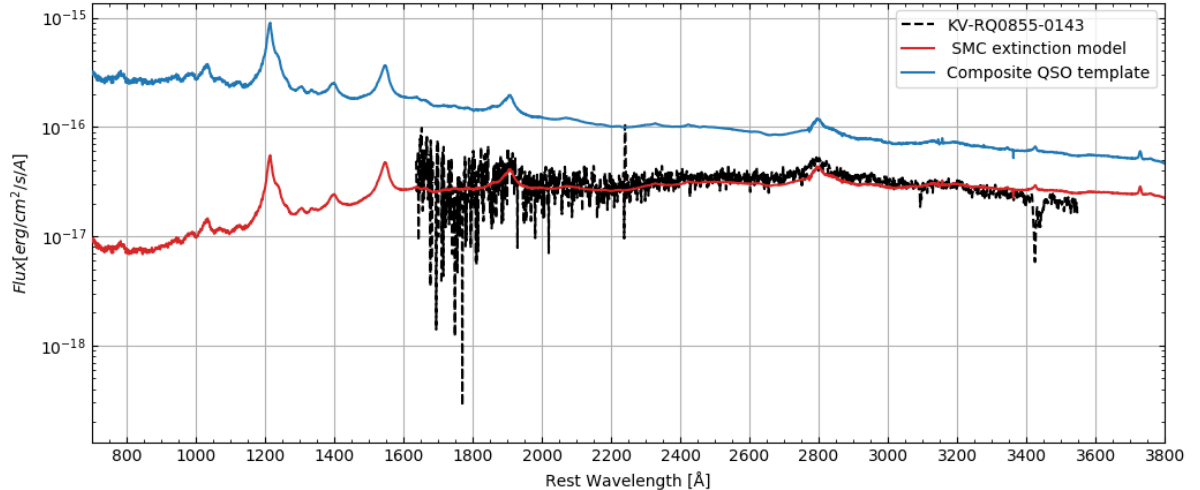


Figure 40: The figure of the photometric red KV-RQ0855-0143 spectrum of an emission line of MgII. As KV-RQ0847+0012 spectra, it has lack of hydrogen lines. The spectrum contains C III and MgII emission lines, and as KV-RQ0847+0012, KV-RQ0855-0143 suspected to contain elements of an intergalactic gas of low redshift.

KV-RQ2242-3219 and KV-RQ2306-3312 are plotted in Figure 36, 37.

Table 7: Low redshift quasars $1 \leq z < 2$ in WISE selection.

Name	$W1 - W2$	$W2 - W3$	Redshift	Extinction
KV-RQ0847+0012 (MgII)	1.325 ± 0.079	3.297 ± 0.170	1.45 ± 0.01	0.20 ± 0.05
KV-RQ0848+0017	1.048 ± 0.094	3.368 ± 0.210	1.95 ± 0.01	0.20 ± 0.05
KV-RQ0855-0143 (MgII)	1.099 ± 0.046	2.941 ± 0.108	1.22 ± 0.01	0.70 ± 0.05
KV-RQ2242-3219 (BAL MgII)	1.023 ± 0.095	3.431 ± 0.243	1.68 ± 0.01	0.40 ± 0.05
KV-RQ2306-3312 (BAL)	0.815 ± 0.041	3.112 ± 0.271	1.92 ± 0.01	0.30 ± 0.05

The minimum extinction of those objects is $0.2 \leq AB$ and most of them have MgII emission lines. All of those low redshift and not rejected samples containing the dust reddening. We believe the dust reddening of low redshift quasars causes to samples resemble dusty objects of the redshift above $z > 2$.

In this case, rejecting those low dusty objects by WISE selection is challenging. In some point, those objects are highly chance to contain intergalactic star-forming dusty regions. Those are not DLA, but interesting objects for other reasons.

5.2 Missing and unclassified objects

After all of those photometric and spectroscopic analyses of samples, we found several samples that was missing photometric/spectroscopic data. The photometric missing samples are KV-RQ0007-3223, KV-RQ1213-0038, KV-RQ1342+0013, KV-RQ1424+0040, KV-RQ2210-3259, KV-RQ1414-0049 and KV-RQ1417+0117.

The spectroscopic missing samples are KV-RQ0834+0120, KV-RQ0848+0017, KV-RQ0906-0009, and KV-RQ2328-3231.

The main colour selection of samples is done by photometric selection. We included those missing spectroscopic samples into our main selection of colours. We did not perform the detail spectroscopic investigation of those samples. The photometric missing data were not including in our investigation, because those samples are not in our colour criteria.

In KV-RQ photometric data, the objects were typed as Type: 0 = *qso*, 1 = *bal*, 2 = *star* and 3 = *unknown*. All of those 3 = *unknown* objects were investigated by spectroscopic investigations. Some of the objects were quasars and have missing redshift and extinction. We rewrote their redshift of extinction into the list, by comparing common emission lines on the composite quasar and the dust model.

We rejected KV-RQ1156-0212, KV-RQ1157-0039 , KV-RQ1415+0154, KV-RQ1434-0238, and KV-RQ1444+0257 by the spectroscopic investigation. They are typed as stellar and unknown objects in KV-RQ photometric data.

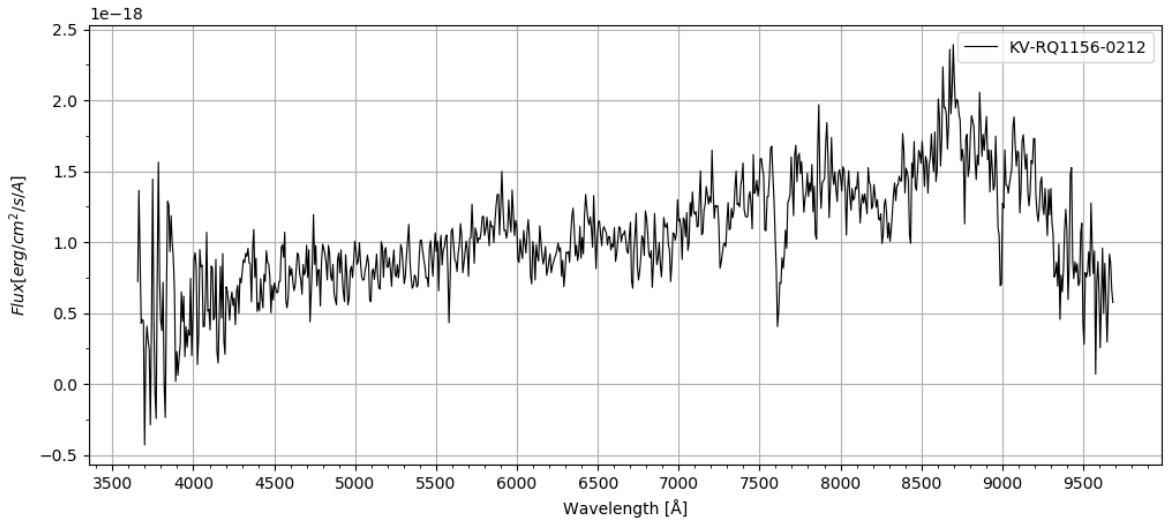


Figure 41: The figure of KV-RQ1156-0212 spectrum. The spectrum has emission lines that resemble a quasar spectrum. The emission lines are weak and hard to recognize in the spectroscopic analysis.

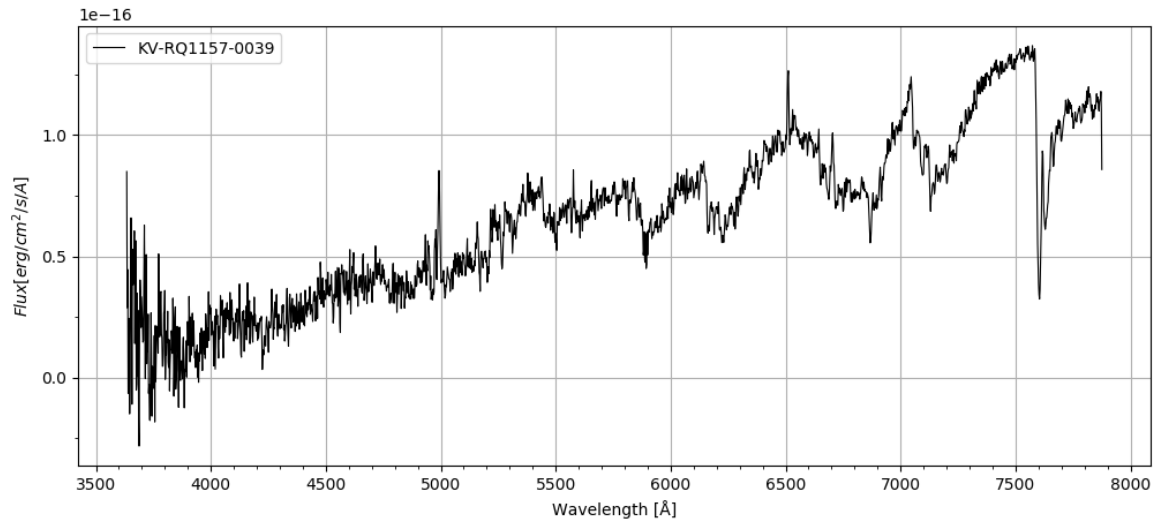


Figure 42: The figure of KV-RQ1157-039 spectrum. We are not sure what this object is.

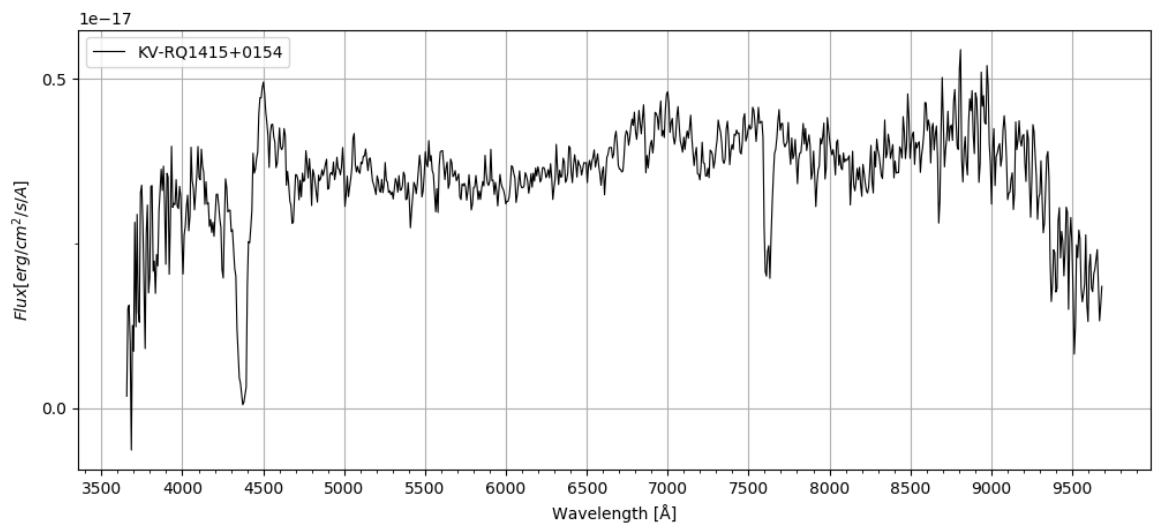


Figure 43: The figure of KV-RQ1415+0154 spectrum. The spectrum has a damping wing and suspected Lyman α emission line. The other lines are very faint and flat.

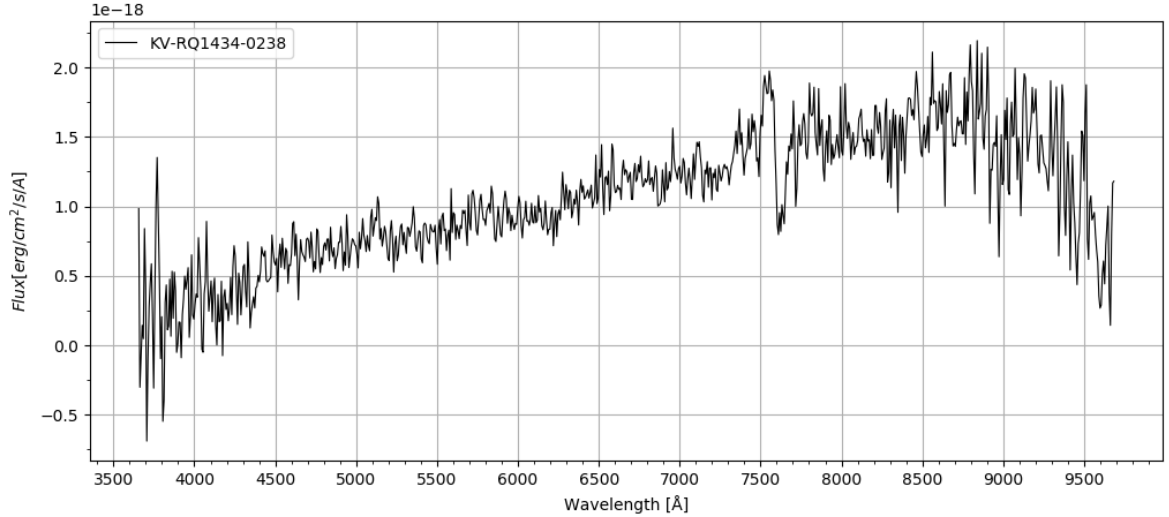


Figure 44: The figure of KV-RQ1434-0238 spectrum. We suspect the spectrum as a red quasar. Still, the spectrum is too faint to recognize any emission lines.

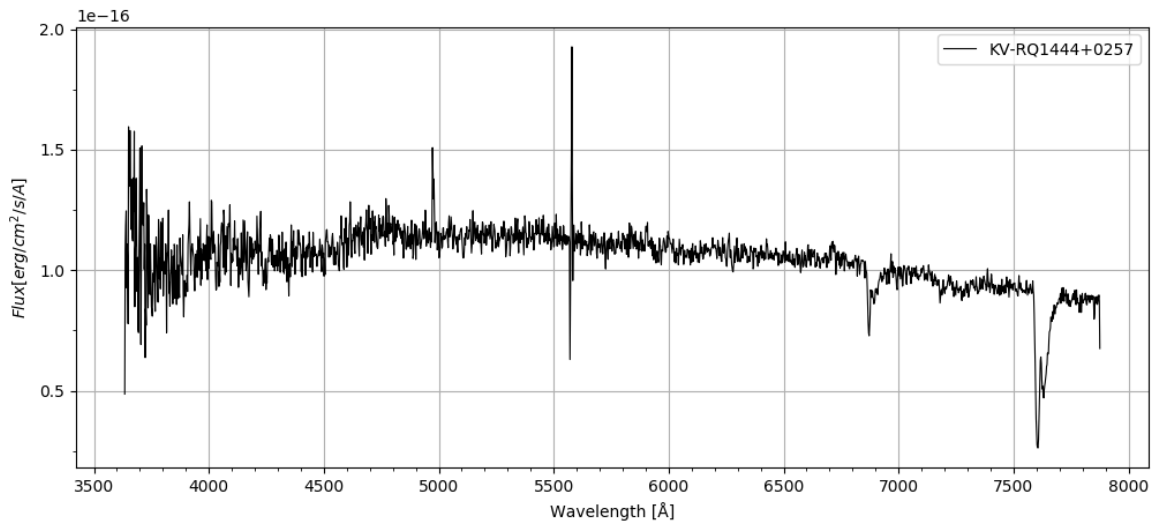


Figure 45: The figure of KV-RQ1444+0257 spectrum. We believe the beginning of the emission lines is Lyman α emissions. However, the emission lines are too faint to the spectroscopic investigation.

The most of samples are suspected to be quasar samples. The main problem of those spectra are that the lines are too flat and faint to be used in the detail spectroscopic investigation, where many emission lines are uncertain to be recognized.

5.3 DLA normalization errors

The Figure in the section 3.2 displays the normalized spectrum of KV-RQ1500-0013. The figure displays that the red markers of normalization of damping wing are not in the stable state. The red marker has a bowed continuum close to the damping wing. The normalization of DLA may have increased the flux size of the damping wing. To get an accurate value of the Voigt profile, we have to improve our normalization with the stable markers.

6 Conclusion

We have identified a sample of candidate KV-RQ quasars with the spectroscopic and photometric investigation. The photometric selection, including photometric data from the KIDS, VIKING and WISE surveys, is mainly used to reject stars and quasars of redshift below $2 \leq z$. The main purpose is to select red quasars to examine the properties of such systems. In particular, we have been interested in looking for quasars with dusty DLAs that could be missing in the traditional photometric selection based on optical colour selection.

We have selected a sample of 54 candidates into the photometric selection. Spectroscopic observations from the OSIRIS spectrograph on the GTC has been reduced and analysed in the thesis. This work led to these conclusions: Among these red quasar candidates were referred to some as the blue and some as the red. The blue population is about 76 % of the sample, where the red population is about 20 % of the sample. The most dominant population in the red population is BAL quasars. The 73 % of the red population is BAL quasars, whereas in the blue population it is about 45 %. The highest redshift found in our sample is 3.64, and the highest B -band extinction is 0.80. Spectroscopic investigation of samples identified the detail type of quasars. By using the Voigt profile, we were able to be identified three DLA systems in our samples. Most of DLA systems were found in photometric blue regions, and some of them display to be spectroscopic red quasars. Type 2 quasar groups seem to be relatively redder than type 1 group. The 46 % of the red population is type 2 quasars. The blue population has about 14 % of type 2 quasars.

One of the stellar objects and some of the low redshift quasars weren't rejected in the photometric colour criteria. Low redshift quasars had extinctions above $0.2 \leq A_B$. We believe those not rejected objects are behind gases and dust and result to resemble the relatively high redshift quasars.

The most of samples are in the redshift region of $2 \leq z < 3$ of 64.8 % of the population. Few samples at $3 \leq z$ of 27.7 % of the population. The redshift region of $1 \leq z < 2$ has rejection criteria that the population is only about 7.4 % of the population. The most of samples are in the extinction between $0.25 < A_B \leq 0.50$, 33.3 % of the population. The samples between $0.00 < A_B \leq 0.25$ are about 31.5 %, the second dominant of the population. Zero extinctions are of 25.9 % of the population, and few samples at the extinction above $0.50 < A_B$ about 11.1 % of the population. The average redshift of the samples is 2.386. The average redshift of the blue population is 2.437, where the red population is 2.111. The average redshift of the red population is lower than the blue population. The average of extinction is the opposite. The average redshift of the samples is 0.24. The average redshift of the blue population is 0.223, where the red population is 0.312.

The extinction of samples displays visible effect on colour selections of the $g - r$ versus $r - i$ selection and the $g - r$ versus $J - K_S$ selection. High extinction objects have a relatively high colour index of $r - i$ and $J - K_S$, that objects appear to be redder. In WISE selection, the redshift has visible influence in the colours. The high redshift objects have high $W2 - W3$ magnitude and low $W1 - W2$ magnitude.

We are aware that the dust reddening causes biases in the optical selection towards red quasar population. The new photometric selection can select high extinct objects without strong biases from extinctions. The question is how much we can select those biased samples.

We compared those with [Heintz *et al.*, 2016] High A_V Quasar (HAQ) selection of the same purpose to select the reddened quasars as dusty rich DLAs and mid-infrared selection of WISE.

$$\begin{aligned} J - K_S > 0.00; \quad H - K > 0.0; \quad J - H < 0.4; \\ 0.5 < g - r < 1.0; \quad 0.1 < r - i < 0.7; \end{aligned} \quad (28)$$

$$W1 - W2 = 0.315(W2 - W3) \quad (29)$$

Remark that the criteria is similar, but not fully the same as our colour criteria. The HAQ selection is the estimation of how much we are able to select those dusty biased samples, comparing to SDSS/BOSS selection.

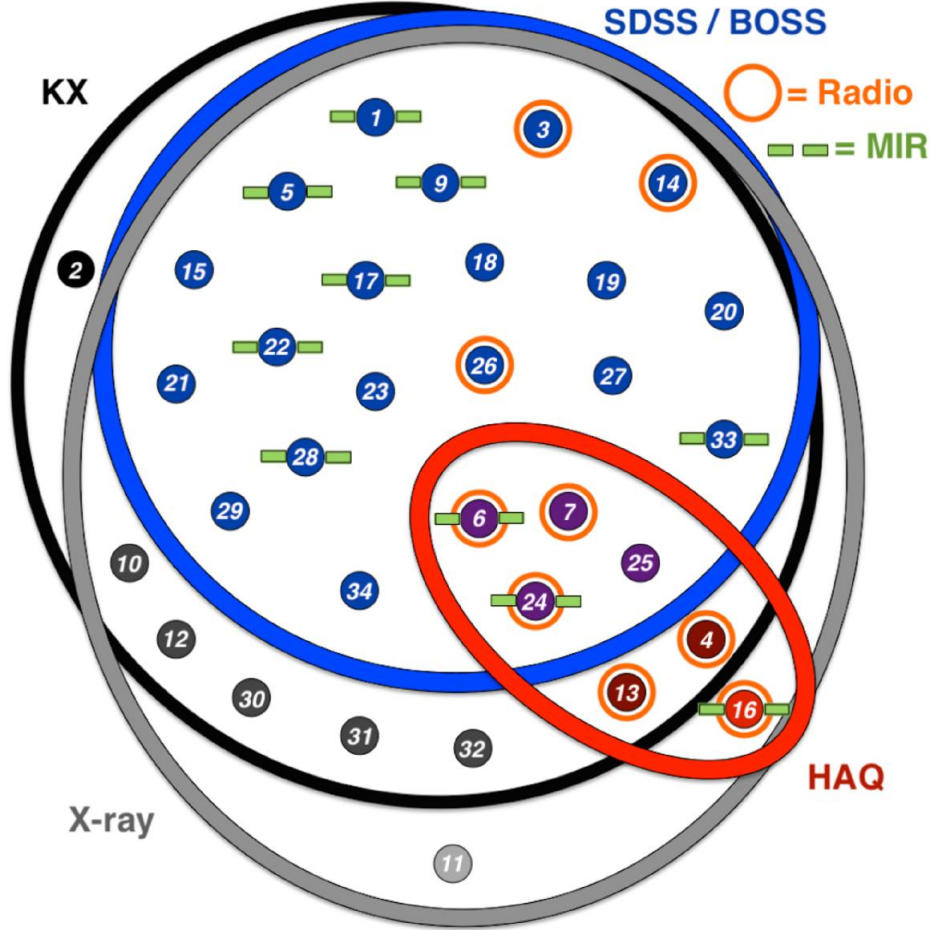


Figure 46: Quantity diagram (Venn diagram) of the 33 confirmed quasars [Heintz *et al.*, 2016]. The list of those quasars is in the Appendix. The diagram contains regions of quasar selection of SDSS/BOSS, radio, MIR, KX and X-ray. Our colour criteria are close the HAQ and MIR selection. The other colour criteria as KX selection, X-ray selection, and radio selection is in [Heintz *et al.*, 2016].

The Figure 46 displays four of seven HAQs are in SDSS/BOSS selection. The SDSS/BOSS photometric selection missed three of seven HAQ in this diagram. In [Heintz *et al.*, 2016], the

data of 409 samples are observed in the SDSS from data of 904 HAQ candidates.

Our colour selection can select high extinction quasars at a rate about twice as large as in the SDSS quasar catalogue by the estimation. It is hard to estimate the number of missing red quasars in our red colour selection. The selection is aimed at the search of the most highly obscured quasars, but we also have a flux limit. There will be many more reddened quasars than those included in our selection. We believe some of reddened quasars that are relatively blue might be missed in our colour selection. The bluest quasars in our sample are similar to some of the reddest quasars seen in the SDSS selection of quasars.

References

- [Bañados *et al.* , 2018] Bañados, Eduardo, Venemans, Bram P, Mazzucchelli, Chiara, Farina, Emanuele P, Walter, Fabian, Wang, Feige, Decarli, Roberto, Stern, Daniel, Fan, Xiaohui, Davies, Frederick B, *et al.* . 2018. An 800-million-solar-mass black hole in a significantly neutral Universe at a redshift of 7.5. *Nature*, **553**(7689), 473.
- [Blain *et al.* , 1999] Blain, A. W., Smail, Ian, Kneib, J.-P., & Ivison, R. J. 1999. The history of star formation in dusty galaxies. *Monthly Notices of the Royal Astronomical Society*, **302**(4), 632–648.
- [de Jong *et al.* , 2013] de Jong, Jelte TA, Kleijn, Gijs A Verdoes, Kuijken, Konrad H, Valentijn, Edwin A, *et al.* . 2013. The kilo-degree survey. *Experimental Astronomy*, **35**(1-2), 25–44.
- [Edge *et al.* , 2013] Edge, Alastair, Sutherland, William, Kuijken, Konrad, Driver, Simon, McMahon, Richard, Eales, Steve, & Emerson, Jim P. 2013. The VISTA kilo-degree infrared galaxy (VIKING) survey: bridging the gap between low and high redshift. *The Messenger*, **154**, 32–34.
- [Fan, 1999] Fan, Xiaohui. 1999. Simulation of stellar objects in sdss color space. *The Astronomical Journal*, **117**(5), 2528.
- [Francis *et al.* , 1991] Francis, Paul, Hewett, Paul C, Foltz, Craig B, Chaffee, Frederic H, Weymann, Ray J, Morris, Simon L, *et al.* . 1991. A high signal-to-noise ratio composite quasar spectrum.
- [Fukugita *et al.* , 2011] Fukugita, Masataka, Yasuda, Naoki, Doi, Mamoru, Gunn, James E, & York, Donald G. 2011. Characterization of sloan digital sky survey stellar photometry. *The Astronomical Journal*, **141**(2), 47.
- [Fynbo *et al.* , 2012] Fynbo, Johan Peter Uldall, Krogager, J-K, Venemans, B, Noterdaeme, P, Vestergaard, Marianne, Møller, P, Ledoux, C, & Geier, S. 2012. Optical/Near-infrared Selection of Red Quasi-stellar Objects: Evidence for Steep Extinction Curves toward Galactic Centers. *The Astrophysical Journal Supplement Series*, **204**(1), 6.
- [García, 2006] García, Thorsten Tepper. 2006. Voigt profile fitting to quasar absorption lines: an analytic approximation to the Voigt–Hjerting function. *Monthly Notices of the Royal Astronomical Society*, **369**(4), 2025–2035.
- [Geier *et al.* , 2019] Geier, SJ, Heintz, Kasper Elm, Fynbo, JPU, Ledoux, Cédric, Christensen, Lise, Jakobsson, Pall, Krogager, J-K, Milvang-Jensen, Bo, Møller, Palle, & Noterdaeme, Pasquier. 2019. Gaia-assisted selection of a quasar reddened by dust in an extremely strong damped Lyman- α absorber at $z=2.226$. *Astronomy & Astrophysics*, **625**, L9.
- [Heintz, 2019] Heintz, Kasper E. 2019. Galaxies through cosmic time illuminated by gamma-ray bursts and quasars. *arXiv preprint arXiv:1910.09849*.
- [Heintz *et al.* , 2016] Heintz, KE, Fynbo, JPU, Møller, P, Milvang-Jensen, B, Zabl, J, Maddox, N, Krogager, J-K, Geier, S, Vestergaard, M, Noterdaeme, P, *et al.* . 2016. Determining the fraction of reddened quasars in COSMOS with multiple selection techniques from X-ray to radio wavelengths. *Astronomy & Astrophysics*, **595**, A13.

- [Heintz *et al.* , 2018] Heintz, KE, Fynbo, JPU, Ledoux, C, Jakobsson, P, Møller, P, Christensen, L, Geier, S, Krogager, J-K, & Noterdaeme, P. 2018. A quasar hiding behind two dusty absorbers-Quantifying the selection bias of metal-rich, damped Ly α absorption systems. *Astronomy & Astrophysics*, **615**, A43.
- [Hewett *et al.* , 2006] Hewett, Paul C, Warren, Stephen J, Leggett, Sandy K, & Hodgkin, Simon T. 2006. The UKIRT Infrared Deep Sky Survey ZY JHK photometric system: passbands and synthetic colours. *Monthly Notices of the Royal Astronomical Society*, **367**(2), 454–468.
- [Hjerting, 1938] Hjerting, F. 1938. Tables facilitating the calculation of line absorption coefficients. *The Astrophysical Journal*, **88**, 508.
- [Krogager *et al.* , 2016] Krogager, J-K, Fynbo, Johan Peter Uldall, Heintz, Kasper Elm, Geier, S, Ledoux, C, Møller, P, Noterdaeme, P, Venemans, BP, & Vestergaard, M. 2016. The Extended High A (V) Quasar Survey: Searching for Dusty Absorbers toward Mid-infrared-selected Quasars. *The Astrophysical Journal*, **832**(1), 49.
- [of Illinois, n.d.] of Illinois, University. *Astro501: Radiative Processes Lecture26*.
- [Pei, 1992] Pei, Yichuan C. 1992. Interstellar dust from the Milky Way to the Magellanic Clouds. *The Astrophysical Journal*, **395**, 130–139.
- [Peterson, 1997] Peterson, Bradley M. 1997. *An introduction to active galactic nuclei*. Cambridge University Press.
- [Petitjean, 1995] Petitjean, Patrick. 1995. Qso absorption line systems. *Pages 339–348 of: Science with the VLT*. Springer.
- [Richards *et al.* , 2002] Richards, Gordon T, Fan, Xiaohui, Newberg, Heidi Jo, Strauss, Michael A, Berk, Daniel E Vanden, Schneider, Donald P, Yanny, Brian, Boucher, Adam, Burles, Scott, Frieman, Joshua A, *et al.* . 2002. Spectroscopic target selection in the sloan digital sky survey: The quasar sample. *The Astronomical Journal*, **123**(6), 2945.
- [Richards *et al.* , 2003] Richards, Gordon T, Hall, Patrick B, Berk, Daniel E Vanden, Strauss, Michael A, Schneider, Donald P, Weinstein, Michael A, Reichard, Timothy A, York, Donald G, Knapp, GR, Fan, Xiaohui, *et al.* . 2003. Red and reddened quasars in the Sloan Digital Sky Survey. *The Astronomical Journal*, **126**(3), 1131.
- [Sandage, 1965] Sandage, Allan. 1965. The Existence of a Major New Constituent of the Universe: the Quasistellar Galaxies. *The Astrophysical Journal*, **141**, 1560.
- [Schmidt, 1963] Schmidt, Maarten. 1963. 3C 273: a star-like object with large red-shift. *Nature*, **197**(4872), 1040–1040.
- [Selsing *et al.* , 2016] Selsing, Jonatan, Fynbo, Johan PU, Christensen, Lise, & Krogager, J-K. 2016. An X-Shooter composite of bright $1 < z < 2$ quasars from UV to infrared. *Astronomy & Astrophysics*, **585**, A87.
- [Shaver *et al.* , 1996] Shaver, Peter Albert, Wall, JV, Kellermann, KI, Jackson, CA, & Hawkins, MRS. 1996. Decrease in the space density of quasars at high redshift. *Nature*, **384**(6608), 439.
- [Sparke & Gallagher III, 2007] Sparke, Linda S, & Gallagher III, John S. 2007. *Galaxies in the universe: an introduction*. Cambridge University Press.

- [Strauss *et al.* , 2002] Strauss, Michael A, Weinberg, David H, Lupton, Robert H, Narayanan, Vijay K, Annis, James, Bernardi, Mariangela, Blanton, Michael, Burles, Scott, Connolly, AJ, Dalcanton, Julianne, *et al.* . 2002. Spectroscopic target selection in the Sloan Digital Sky Survey: the main galaxy sample. *The Astronomical Journal*, **124**(3), 1810.
- [Tepper-García, 2007] Tepper-García, Thorsten. 2007. Erratum: Voigt profile fitting to quasar absorption lines: an analytic approximation to the Voigt–Hjerting function. *Monthly Notices of the Royal Astronomical Society*, **382**(3), 1375–1375.
- [Venemans *et al.* , 2013] Venemans, BP, Findlay, JR, Sutherland, WJ, De Rosa, G, McMahon, RG, Simcoe, R, González-Solares, EA, Kuijken, K, & Lewis, JR. 2013. Discovery of three $z \approx 6.5$ quasars in the VISTA kilo-degree infrared galaxy (VIKING) survey. *The Astrophysical Journal*, **779**(1), 24.

7 Appendix

7.1 The list of chemical emissions of arc lamp

3600.169	NeI
3606.522	Ar
3610.32	XeI
3613.06	XeI
3633.06	XeI
3650.153	HgI
3654.836	HgI
3663.279	HgI
3669.91	XeI
3685.90	XeI
3693.49	XeI
3701.224	NeI
3770.369	ArI
3834.678	Ar
3948.979	ArI
4044.418	ArI
4046.563	HgI
4077.831	Hg
4158.590	ArI
4164.180	ArI
4181.884	ArI
4190.713	ArI
4191.029	ArI
4198.317	ArI
4200.674	ArI
4251.185	ArI
4259.362	ArI
4266.286	ArI
4272.169	ArI
4300.101	ArI
4333.561	ArI
4335.338	ArI
4339.223	HgI
4347.494	HgI
4345.168	ArI
4358.328	HgI
4500.977	Xe
4510.733	ArI
4522.323	ArI
4524.680	Xe
4537.755	NeI
4582.747	Xe
4589.289	Ar
4596.097	Ar
4624.276	Xe
4628.441	Ar
4671.226	Xe
4697.020	Xe
4702.316	Ar
4704.395	NeI
4708.859	NeI
4710.065	NeI
4712.063	NeI
4715.344	NeI
4734.152	XeI
4752.732	NeI
4788.926	NeI
4790.219	NeI
4792.619	XeI
4807.019	XeI
4827.338	NeI
4829.709	XeI
4843.294	XeI
4884.917	NeI
4916.510	XeI
4923.152	XeI
5005.159	NeI
5028.280	XeI
5037.751	NeI
4144.938	NeI
5162.285	Ar
5187.746	ArI
5221.270	Ar
5252.787	Ar
5330.778	NeI
5341.094	NeI
5343.283	NeI
5392.800	XeI
5400.562	NeI
5421.351	NAr
5451.652	Ar
5460.735	HgI
5495.874	ArI
5558.702	ArI
5562.766	NeI
5566.62	XeI
5606.733	ArI
5650.704	ArI
5656.659	NeI
5695.75	XeI
5719.225	NeI
5739.519	Ar
5748.299	NeI

5764.419	NeI
5769.598	HgI
5790.663	HgI
5804.450	NeI
5820.156	NeI
5823.89	XeI
5824.80	XeI
5834.264	Ar
5852.488	NeI
5860.310	Ar
5872.828	NeI
5881.895	NeI
5888.584	ArI
5894.99	XeI
5902.462	NeI
5906.429	NeI
5912.085	ArI
5934.17	XeI
5944.834	NeI
5965.471	NeI
5974.627	NeI
5975.534	NeI
5987.907	NeI
6029.997	NeI
6032.127	ArI
6043.223	ArI
6059.372	ArI
6074.338	NeI
6096.163	NeI
6105.635	Ar
6128.450	NeI
6143.063	NeI
6163.594	NeI
6173.096	Ar
6178.30	XeI
6179.66	XeI
6182.146	NeI
6182.42	XeI
6198.26	XeI
6215.939	Ar
6217.281	NeI
6266.495	NeI
6286.01	XeI
6304.789	NeI
6318.06	XeI
6328.16	NeI
6334.428	NeI
6382.992	NeI
6384.717	ArI
6402.248	NeI
6416.307	ArI
6469.70	XeI
6472.84	XeI
6487.76	XeI
6498.72	XeI
6504.18	XeI
6506.528	NeI
6532.882	NeI
6533.16	XeI
6538.112	Ar
6598.953	NeI
6604.853	Ar
6652.093	NeI
6668.92	XeI
6677.282	ArI
6678.276	NeI
6682.960	HgI ₂
6717.043	NeI
6728.01	XeI
6752.834	ArI
6827.32	XeI
6871.289	ArI
6872.11	XeI
6882.16	XeI
6903.380	HgI ₂
6925.53	XeI
6929.467	NeI
6937.664	ArI
6965.431	ArI
6976.18	XeI
7024.050	NeI
7030.251	ArI
7032.413	NeI
7051.292	NeI
7059.107	NeI
7067.218	ArI
7068.736	ArI
7081.900	HgI
7107.478	ArI
7119.60	XeI
7125.820	ArI
7147.042	ArI
7173.938	NeI
7206.980	ArI
7245.167	NeI
7272.936	ArI
7300.306	HgI ₂ (3650.153)
7311.716	ArI
7316.005	ArI
7353.293	ArI
7372.118	ArI
7383.980	ArI
7386.00	XeI

7392.980	ArI
7393.79	XeI
7435.368	ArI
7472.439	NeI
7488.871	NeI
7503.869	ArI
7514.652	ArI
7535.774	NeI
7544.044	NeI
7584.68	XeI
7635.106	ArI
7642.02	XeI
7643.91	XeI
7723.761	ArI
7724.207	ArI
7724.623	NeI
7839.053	NeI
7927.118	NeI
7936.996	NeI
7943.181	NeI
7948.176	ArI
7802.65	XeI
7881.32	XeI
7887.40	XeI
7967.34	XeI
8006.157	ArI
8014.786	ArI
8029.67	XeI
8057.26	XeI
8061.34	XeI
8082.458	NeI
8093.126	HgI2 (4046.563)
8101.98	XeI
8103.693	ArI
8115.311	ArI
8118.549	NeI
8128.911	NeI
8136.405	NeI
8171.02	XeI
8171.311	ArI
8206.34	XeI
8231.635	XeI
8259.379	NeI
8264.522	ArI
8266.077	NeI
8266.52	XeI
8267.116	NeI
8280.117	XeI
8300.326	NeI
8346.823	XeI
8365.747	NeI
8377.608	NeI
8392.270	ArI
8408.210	ArI
8409.191	XeI
8417.161	NeI
8418.427	NeI
8424.648	ArI
8463.358	NeI
8484.444	NeI
8495.356	NeI
8521.442	ArI
8544.696	NeI
8571.352	NeI
8576.01	XeI
8591.258	NeI
8634.647	NeI
8647.041	NeI
8648.54	XeI
8654.383	NeI
8655.522	NeI
8667.944	ArI
8679.492	NeI
8681.921	NeI
8692.20	XeI
8696.86	XeI
8704.112	NeI
8716.654	HgI2 (4358.328)
8739.39	XeI
8758.20	XeI
8771.656	NeI
8780.623	NeI
8783.753	NeI
8819.411	XeI
8830.907	NeI
8849.910	ArI
8853.867	NeI
8865.306	NeI
8865.755	NeI
8908.73	XeI
8919.501	NeI
8930.83	XeI
8952.252	XeI
8962.32	XeI
8981.05	XeI
8987.57	XeI
8988.556	NeI
9045.45	XeI
9075.394	ArI
9122.967	ArI
9148.672	NeI
9162.65	XeI
9167.52	XeI

9194.638	ArI
9201.759	NeI
9220.060	NeI
9221.580	NeI
9224.499	ArI
9226.690	NeI
9275.529	NeI
9291.531	ArI
9300.853	NeI
9310.584	NeI
9313.973	NeI
9326.507	NeI
9354.220	ArI
9373.308	NeI
9374.76	XeI
9425.379	NeI
9459.209	NeI
9486.682	NeI
9513.38	XeI
9534.163	NeI
9547.405	NeI
9657.786	ArI
9665.420	NeI
9685.32	XeI
9718.16	XeI
9799.70	XeI
9784.503	ArI
9923.19	XeI
10052.06	ArI
10139.76	HgI

7.2 Spectral Classification of stars

The information of those pictures is borrowed from the University of Oregon (Department of Physics).

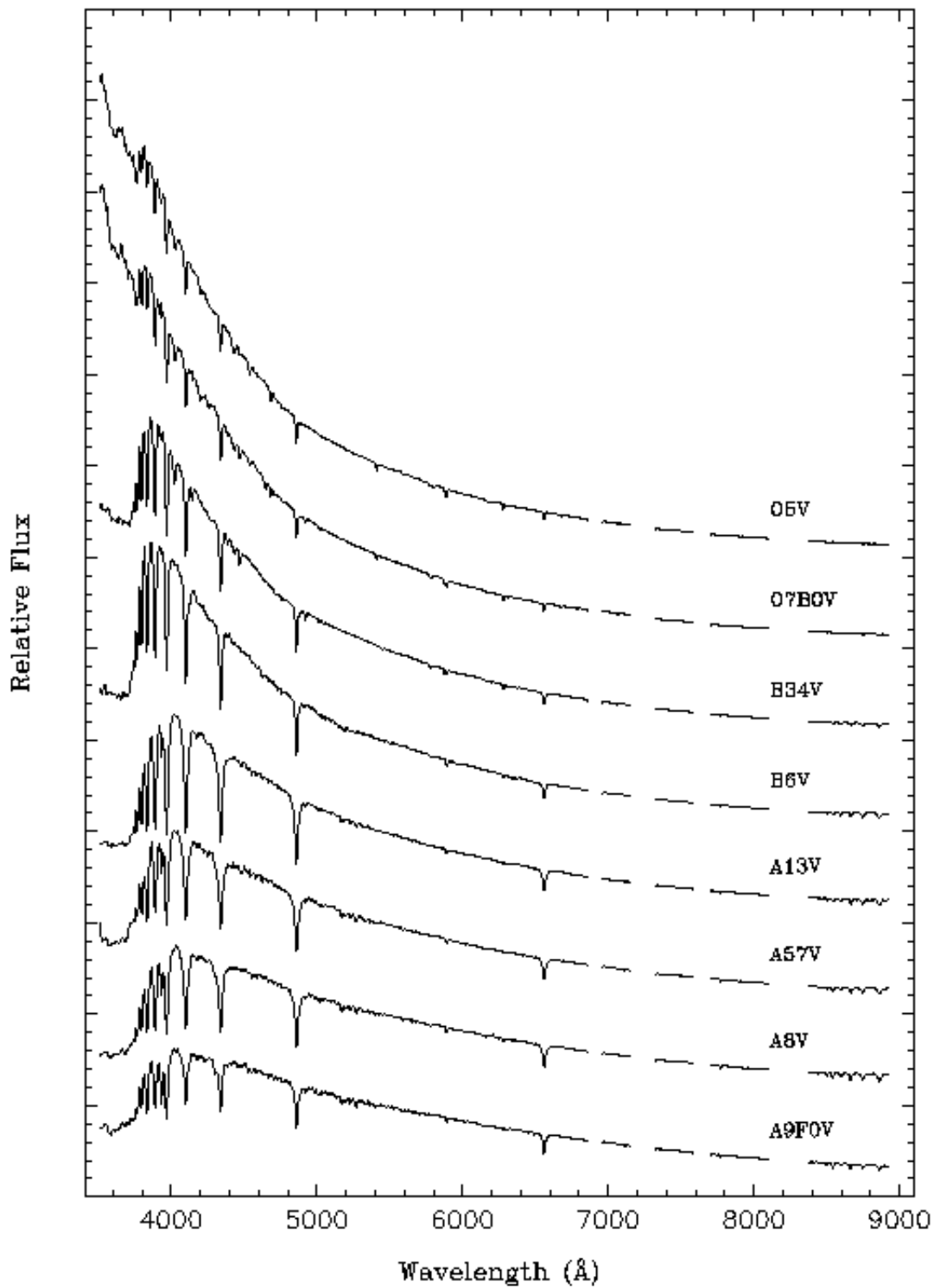


Figure 47: A9 - O5 main sequence stars

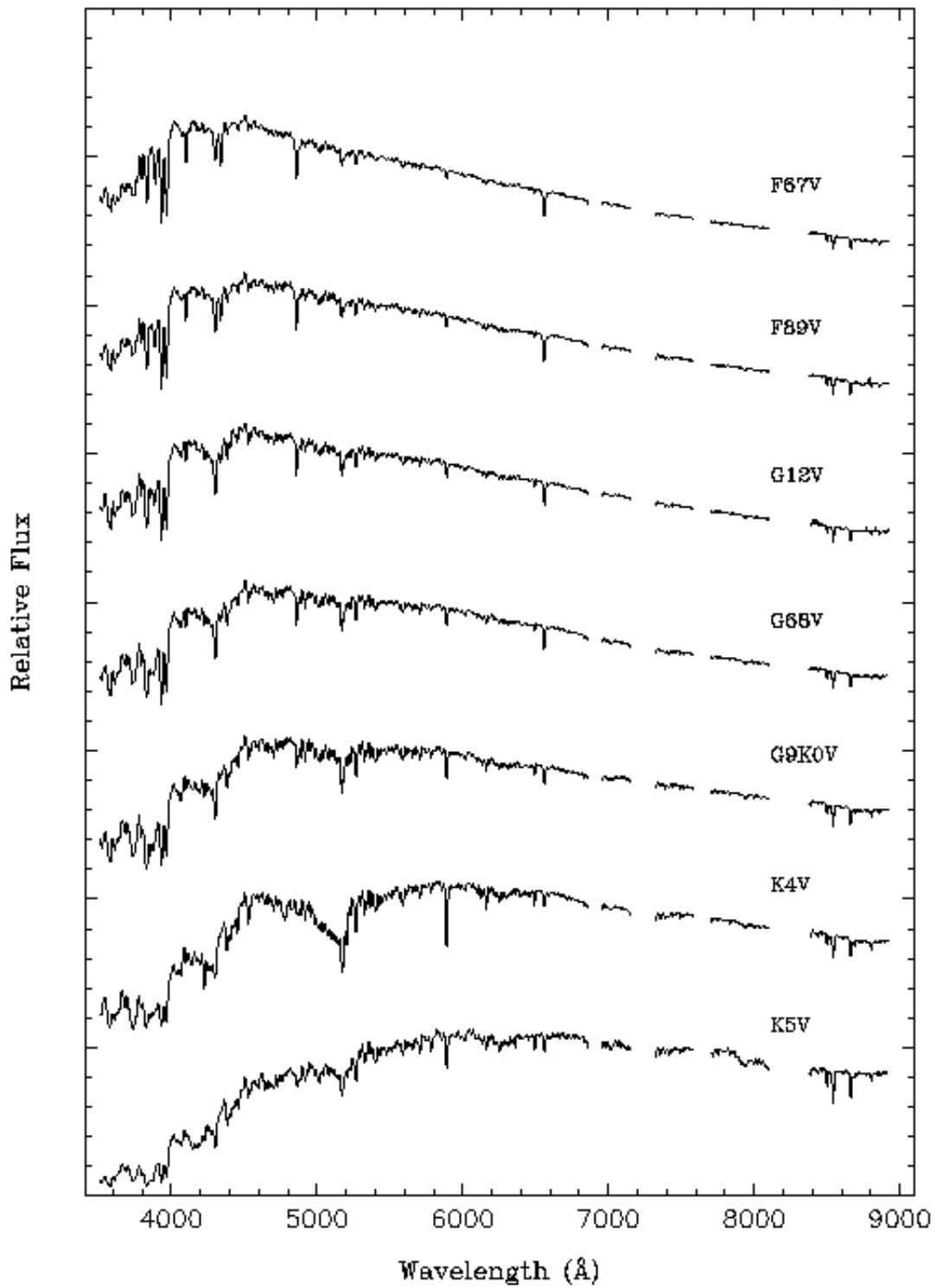


Figure 48: K5 - F7 main sequence stars.

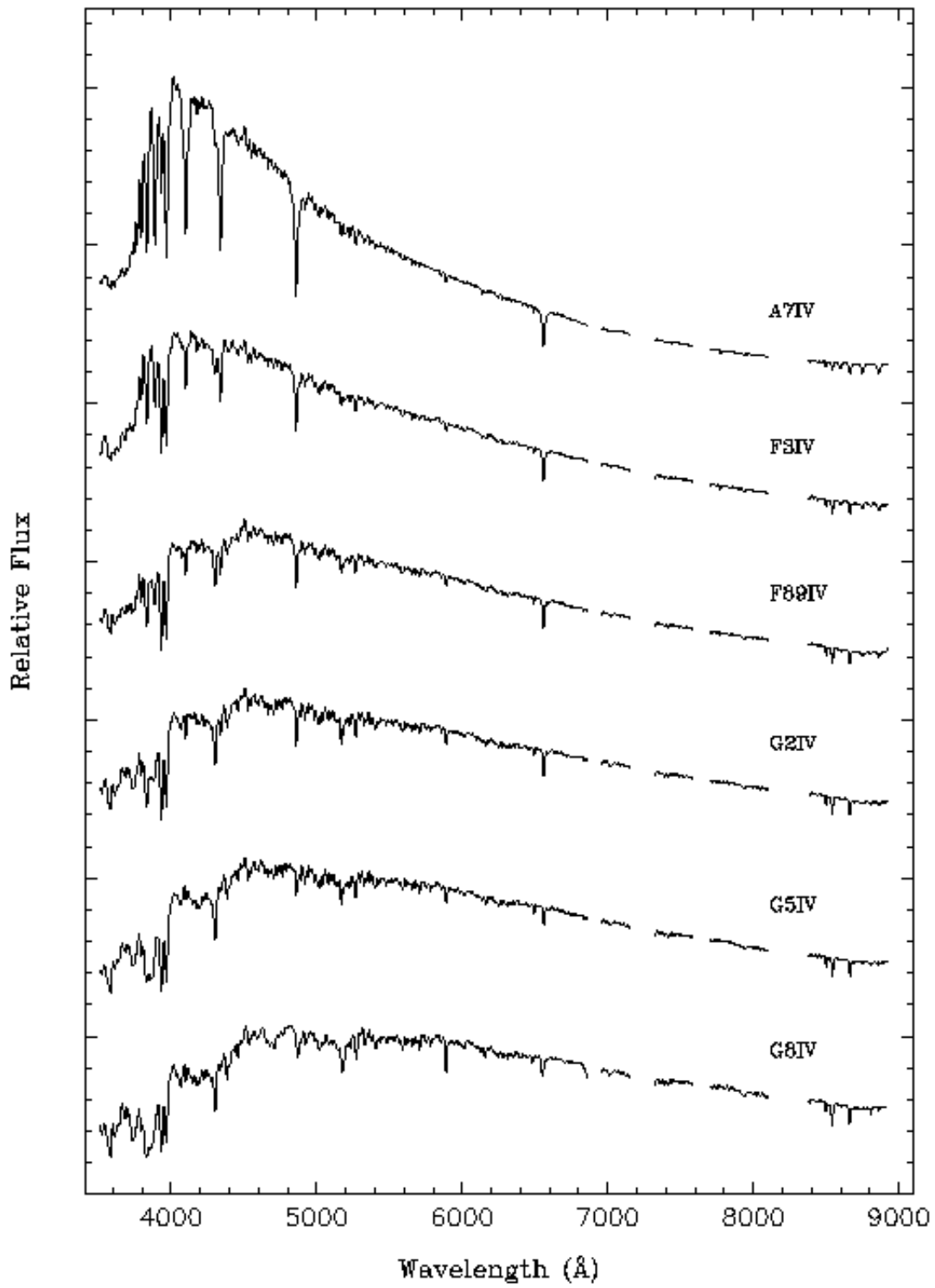


Figure 49: G8 - A7 main sequence stars.

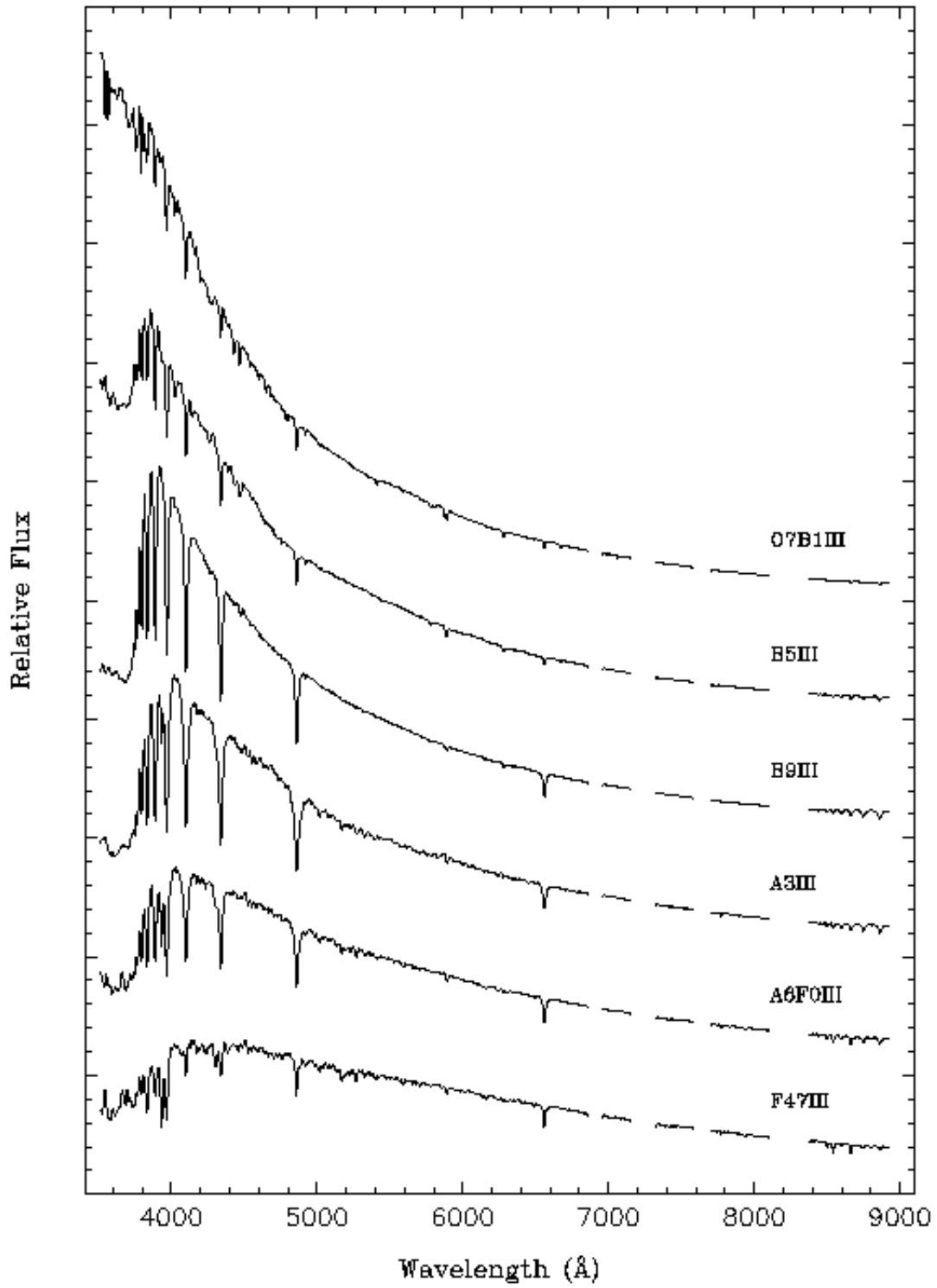


Figure 50: Blue Giants.

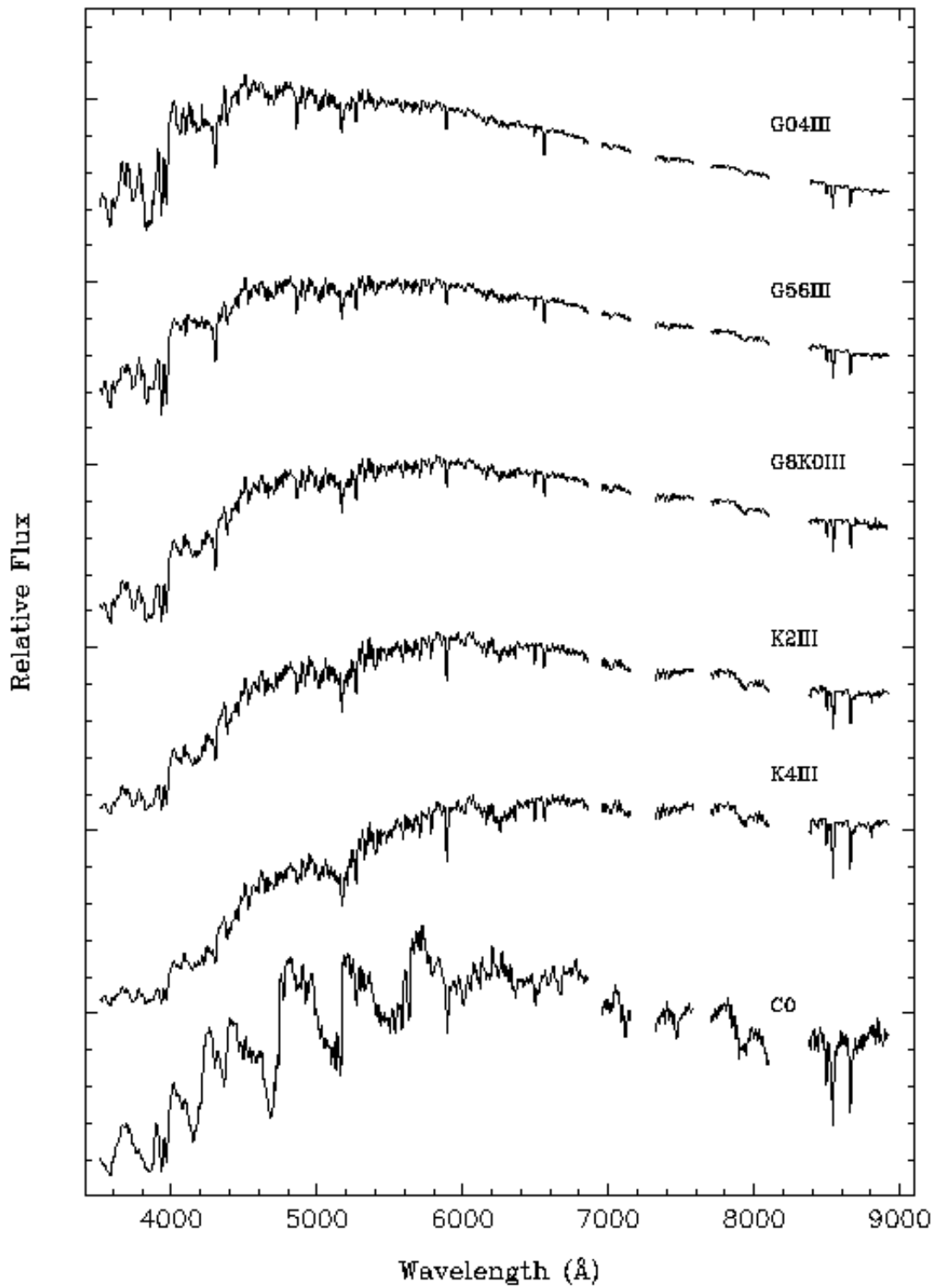


Figure 51: Red Giants.

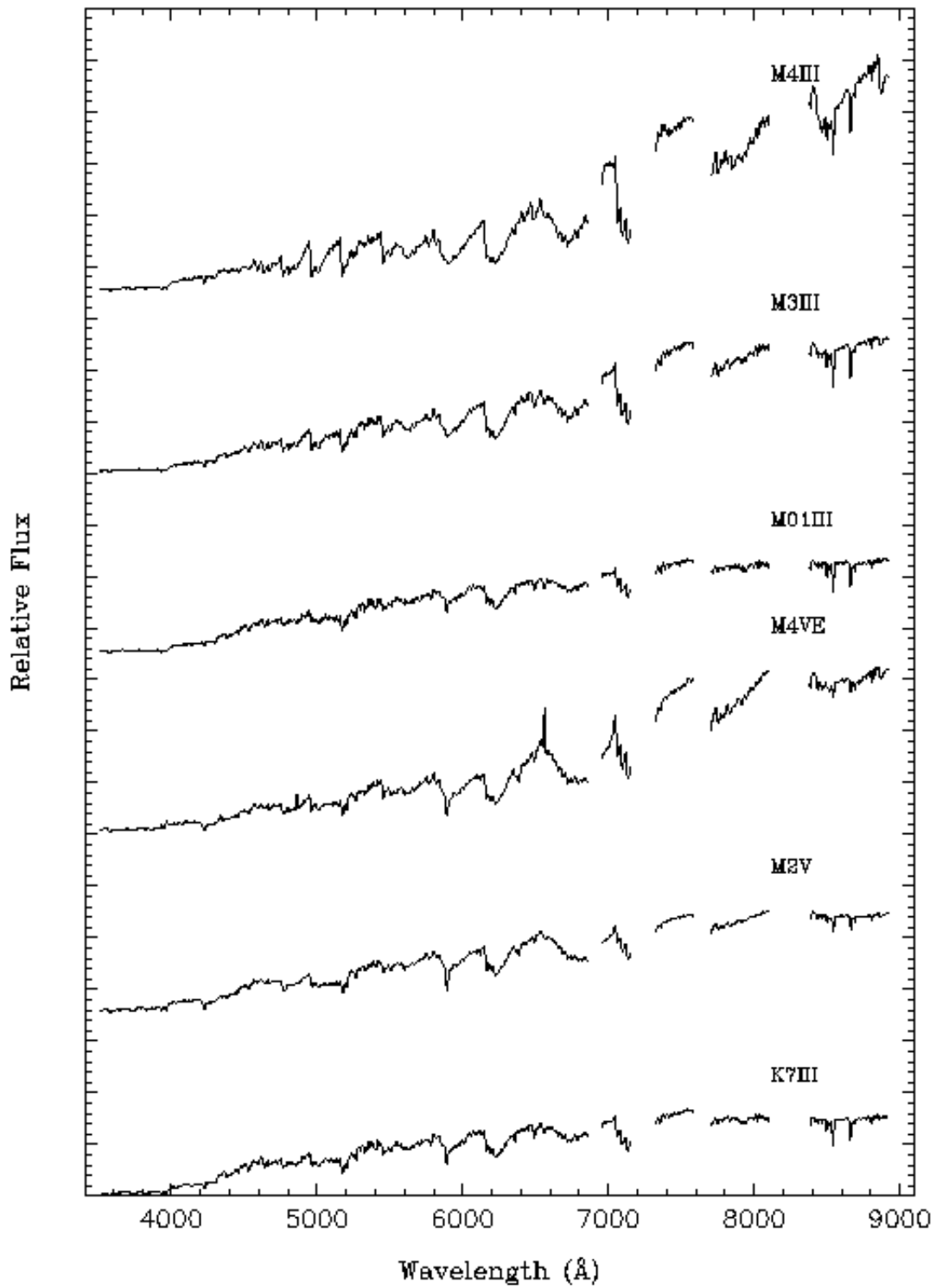


Figure 52: Very Cool Giants.

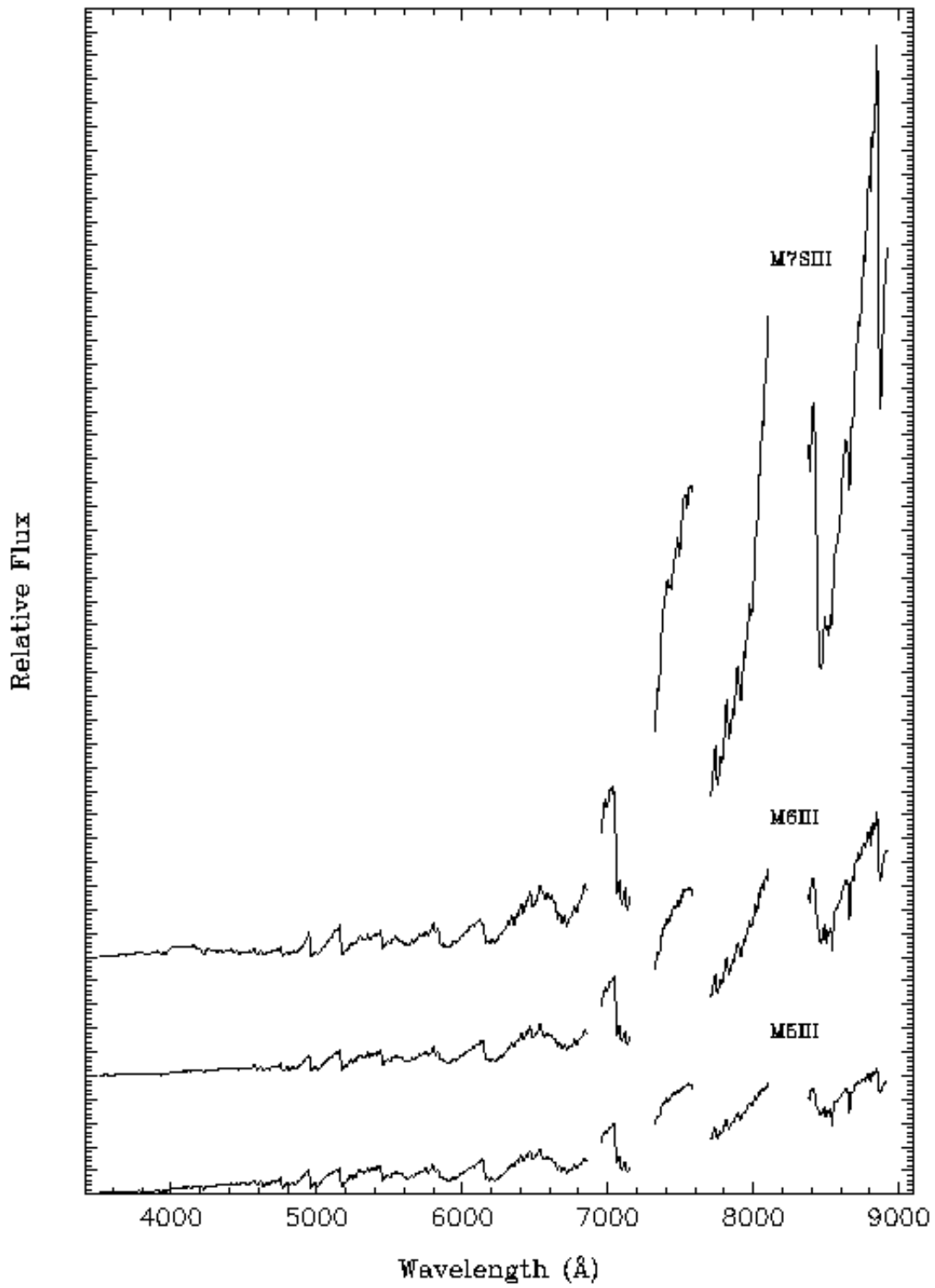


Figure 53: Extreme Molecular Band Heads.

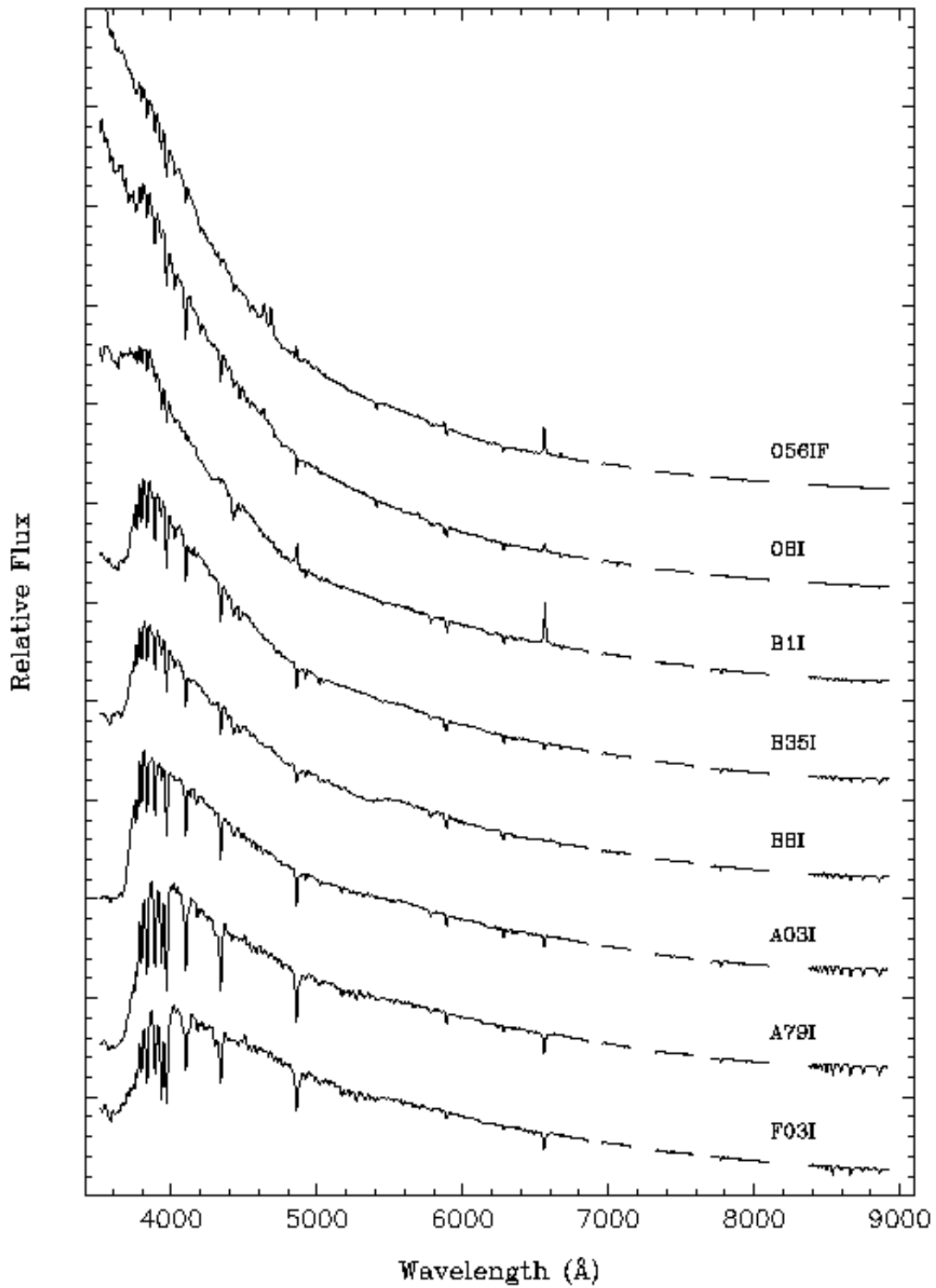


Figure 54: Blue Supergiants.

Some missing flux in these spectra is due to calibration problems associated with sky subtraction. (<http://www.eso.org/cguirao/caos/spectralclassification/SpectralClassification.html>).

7.3 Table of photometric data of [Heintz *et al.* , 2016]

#	Object	Selection	z_{spec}	z_{phot}	A_V (SMC)	A_V (Zafar+15)	J -band (mag)	Notes
(1)	(2)	(3)	(4)	(5)	(6)	(7)	(8)	(9)
1	Q 095820.5+ 020304.1	KXMS	1.356	1.462	0.00	0.00	19.70	$g-r, r-i$
2	CQ 095833.3+ 021720.4	K	1.910	1.750	0.23	0.23	19.99	$g-r$
3	Q 095836.0+015157.1	KXRB	2.935	2.919	0.00	0.00	19.32	$g-r$
4	Q 095857.4+ 021314.5	KXRH	1.024	1.043	0.38	0.30	19.41	
5	Q 095858.7+ 020139.1	KXMB	2.448	2.418	0.00	0.00	18.70	$g-r, r-i$
6	Q 095918.7+ 020951.7	KXRMSH	1.156	1.181	0.30	0.15	19.72	
7	Q 095921.3+ 024412.4	KXRBH	1.004	0.030	0.98	0.60	19.37	
8	CQ 095924.4+ 020842.6	K	-	1.150	-	-	19.43	$g-r$, blended SED, non-quasar
9	Q 095924.5+015954.3	KXMS	1.241	1.281	0.00	0.00	18.49	$g-r, r-i$
10	Q 095938.3+ 020450.1	KX	2.802	2.779	0.23	0.08	19.74	$H-K_s$
11	CQ 095938.6+ 023316.7	X	0.740	0.742	1.21	0.68	19.47	$g-r$
12	Q 095940.1+ 022306.7	KX	1.131	1.110	0.15	0.15	19.93	$g-r, r-i$
13	Q 095940.8+ 021938.7	KXRH	1.454	1.465	0.30	0.30	19.74	
14	Q 095943.4+ 020707.4	KXRB	2.194	2.306	0.00	0.00	19.45	$g-r, r-i$
15	Q 095949.4+ 020141.0	KXS	1.753	1.753	0.00	0.00	18.99	$g-r$
16	CQ 100008.9+021440.7	XRMSH	2.680	2.663	0.15	0.15	18.96	
17	Q 100012.9+ 023522.8	KXMS	0.698	0.702	0.00	0.08	18.47	$g-r$
18	Q 100014.1+ 020054.5	KXS	2.498	2.469	0.00	0.00	19.45	$g-r, r-i$
19	Q 100024.4+015054.0	KXS	1.661	1.669	0.30	0.30	19.61	$g-r, H-K_s$
20	Q 100024.5+ 020619.8	KXB	2.288	2.287	0.00	0.00	19.51	$g-r, r-i$
21	Q 100024.6+ 023149.1	KXS	1.319	1.362	0.00	0.00	19.36	$g-r, r-i, H-K_s$
22	Q 100025.3+015852.1	KXMS	0.372	0.372	0.00	0.00	19.07	$g-r$
23	Q 100047.8+ 020756.8	KXB	2.159	2.177	0.00	0.00	19.67	$g-r, r-i$
24	Q 100049.9+ 020500.0	KXRMBH	1.236	1.272	0.30	0.30	19.04	
25	Q 100050.1+ 022854.8	KXBH	3.365	3.378	0.00	0.00	19.64	
26	Q 100055.4+ 023441.4	KXRS	1.402	1.414	0.08	0.08	19.74	$g-r, r-i$
27	Q 100058.8+015400.3	KXS	1.560	1.557	0.00	0.00	19.87	$g-r, r-i$
28	Q 100114.3+ 022356.7	KXMS	1.802	1.777	0.00	0.00	19.38	$g-r$
29	Q 100116.8+014053.6	KXS	2.055	2.050	0.00	0.00	19.76	$g-r$
30	Q 100120.3+ 020341.2	KX	0.903	0.906	0.00	0.00	19.77	$g-r, r-i$
31	Q 100151.1+ 020032.5	KX	0.967	1.000	0.23	0.11	19.79	$g-r, r-i$
32	Q 100159.8+ 022641.7	KX	2.030	2.011	0.00	0.00	19.27	$g-r$
33	Q 100201.5+ 020329.4	KXMS	2.016	1.880	0.23	0.23	18.30	$g-r$
34	Q 100210.7+ 023026.2	KXS	1.160	1.340	0.00	0.00	19.17	$g-r, r-i$, XMM-COSMOS source

Figure 55: Note for the selection techniques; K = KX selection, X = X-ray detection, R = radio detection, M = MIR selection, S/B = SDSS/BOSS photometric selection, and H = HAQ selection. Directed copied from (<https://www.aanda.org/articles/aa/fullhtml/2016/11/aa28836-16/T1.html>)

7.4 Spectra of KV-RQ

KVRQ - blue observed:

The spectrum of KV-RQ0841-0058 is missing.

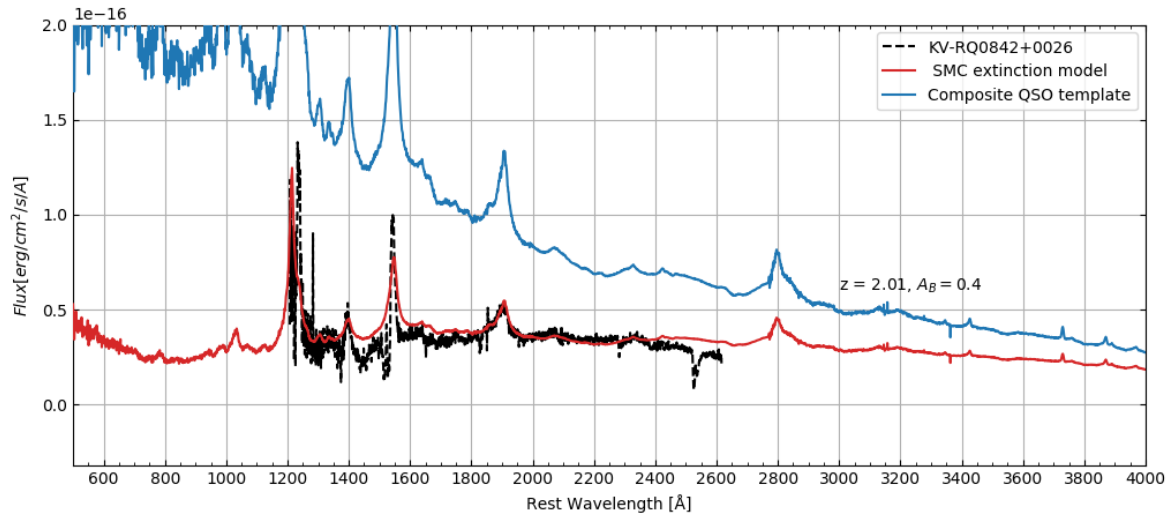


Figure 56: Figure of the spectrum of KV-RQ0842+0026.

The spectrum of KV-RQ0848+0017 is missing.

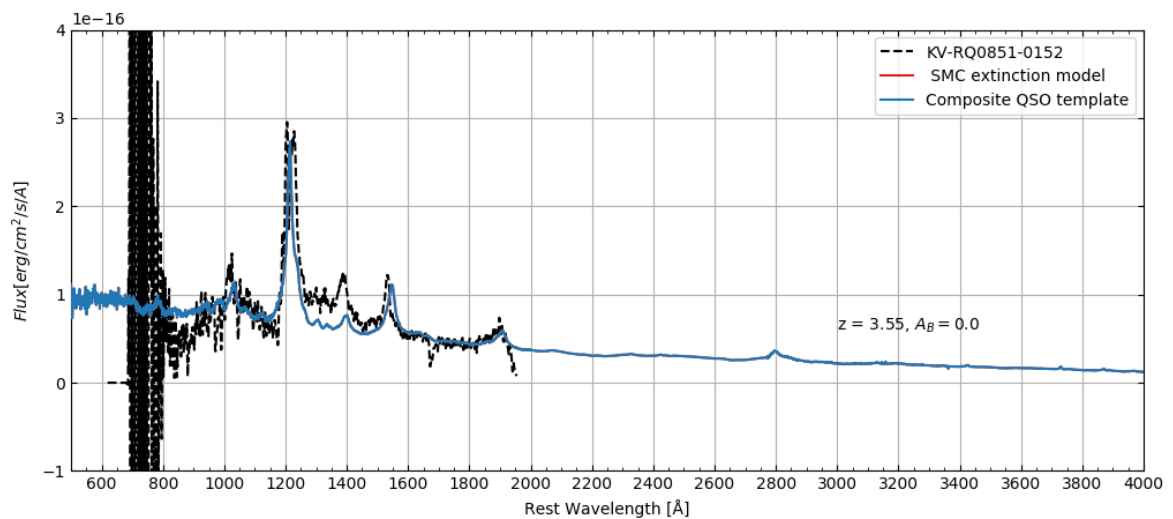


Figure 57: Figure of the spectrum of KV-RQ0851-0152.

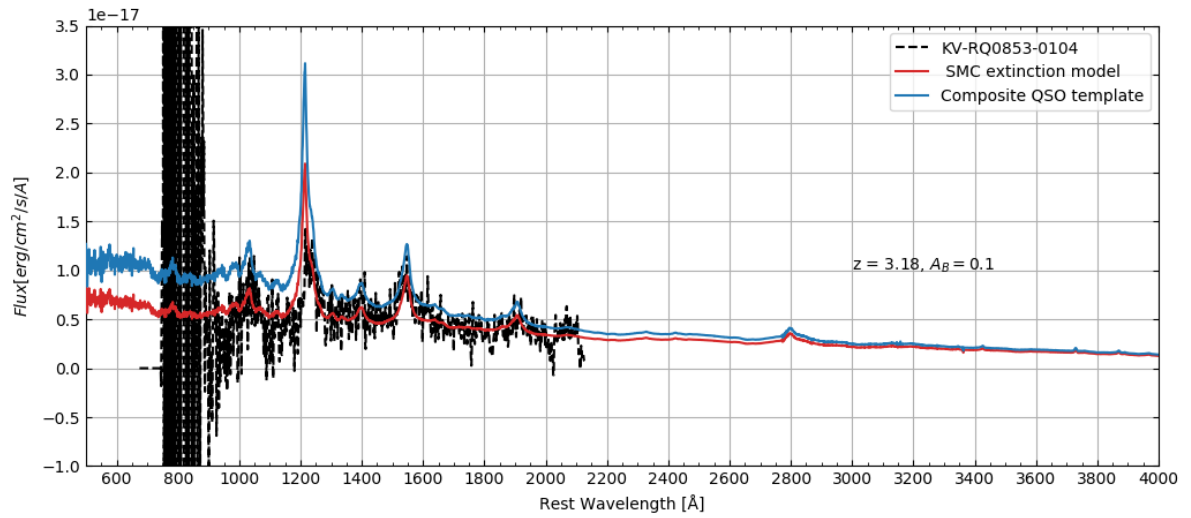


Figure 58: Figure of the spectrum of KV-RQ0853-0104.

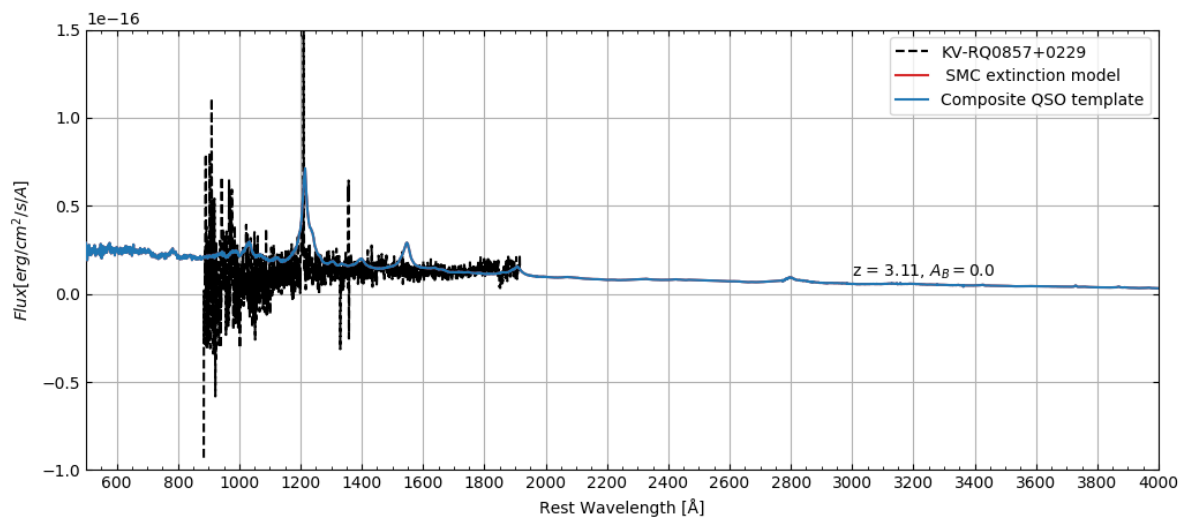


Figure 59: Figure of the spectrum of KV-RQ0857+0229.

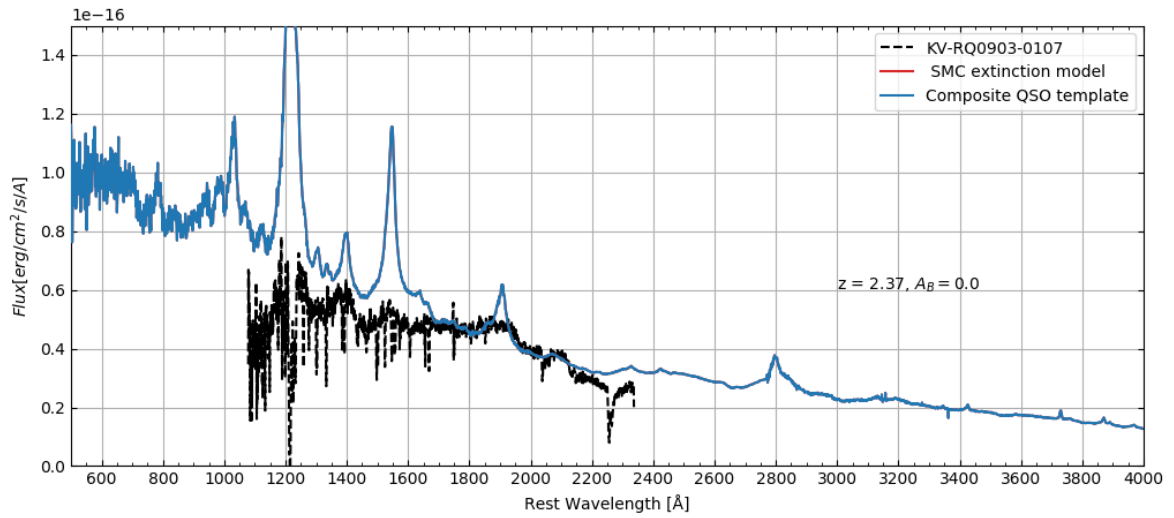


Figure 60: Figure of the spectrum of KV-RQ0903-0107.

The spectrum of KV-RQ0906-0009 is missing.

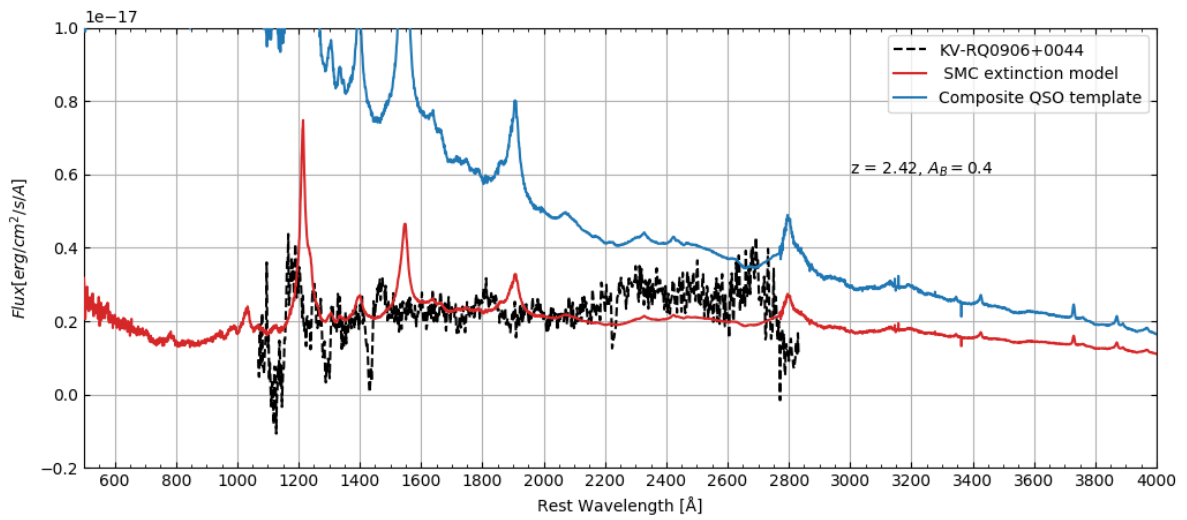


Figure 61: Figure of the spectrum of KV-RQ0906+0044.

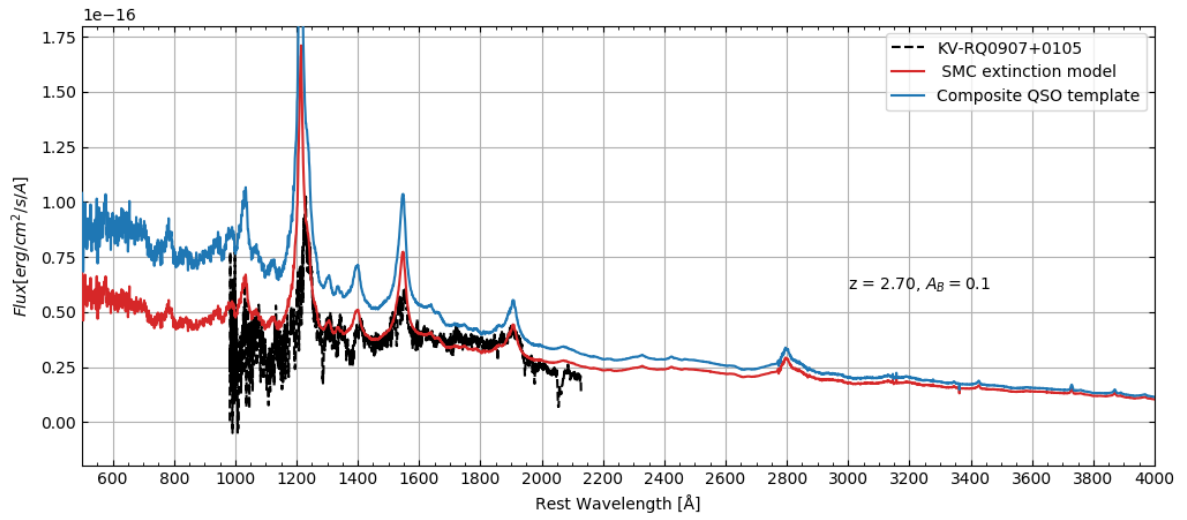


Figure 62: Figure of the spectrum of KV-RQ0907+0105.

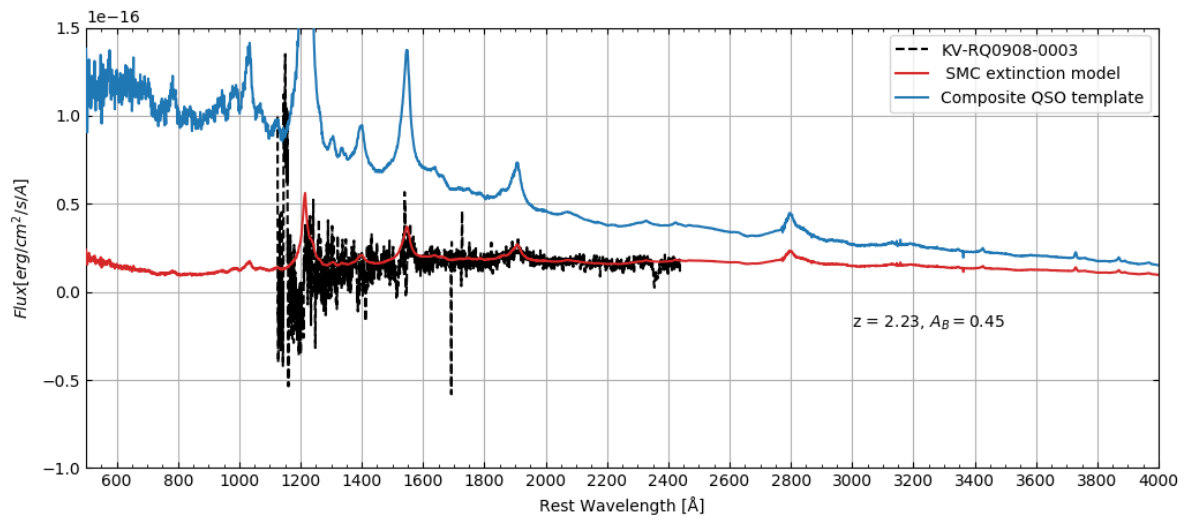


Figure 63: Figure of the spectrum of KV-RQ0908-0003.

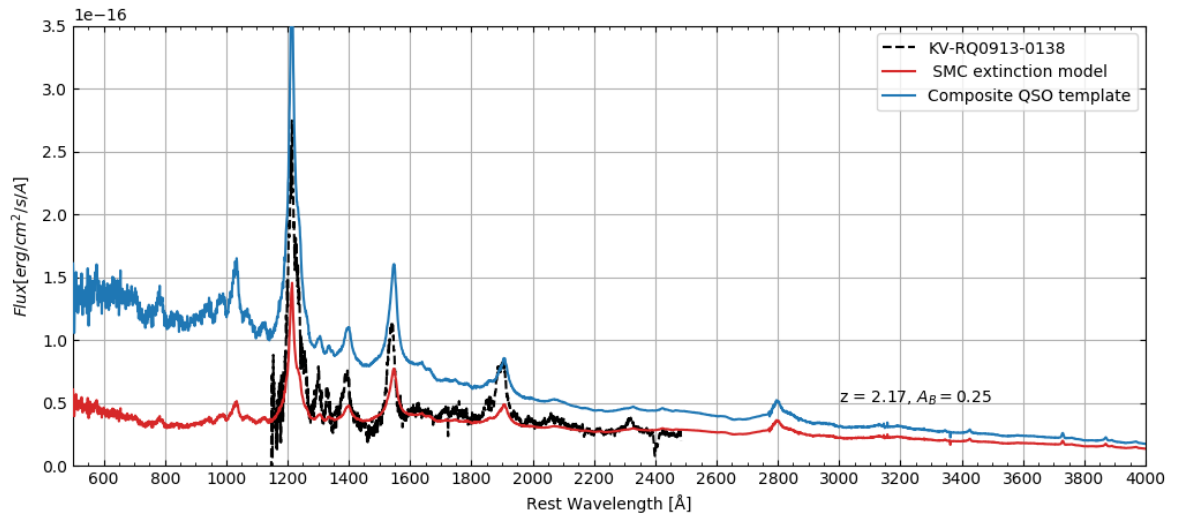


Figure 64: Figure of the spectrum of KV-RQ0913-0138.

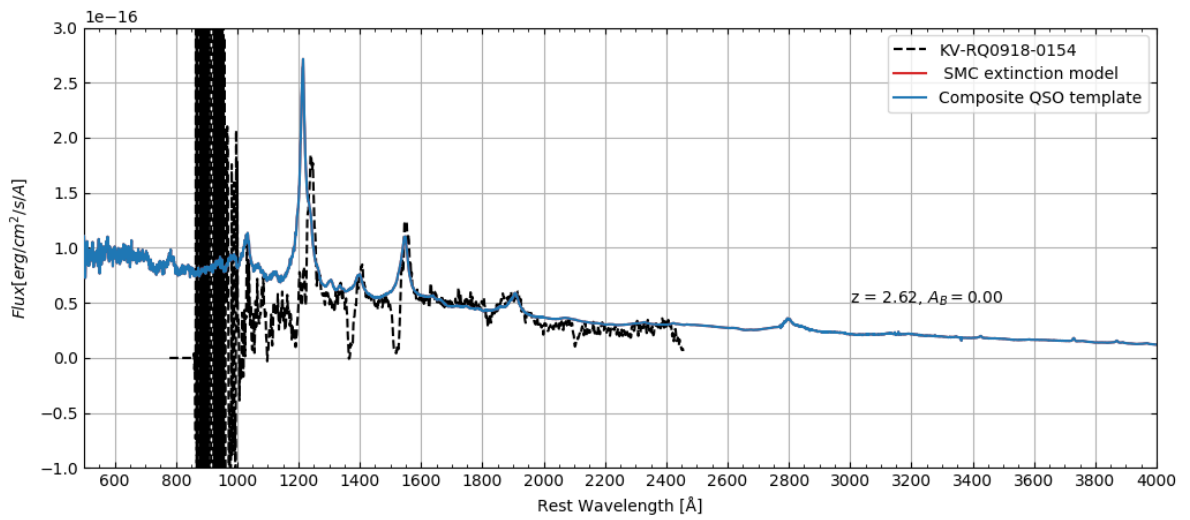


Figure 65: Figure of the spectrum of KV-RQ0918-0154.

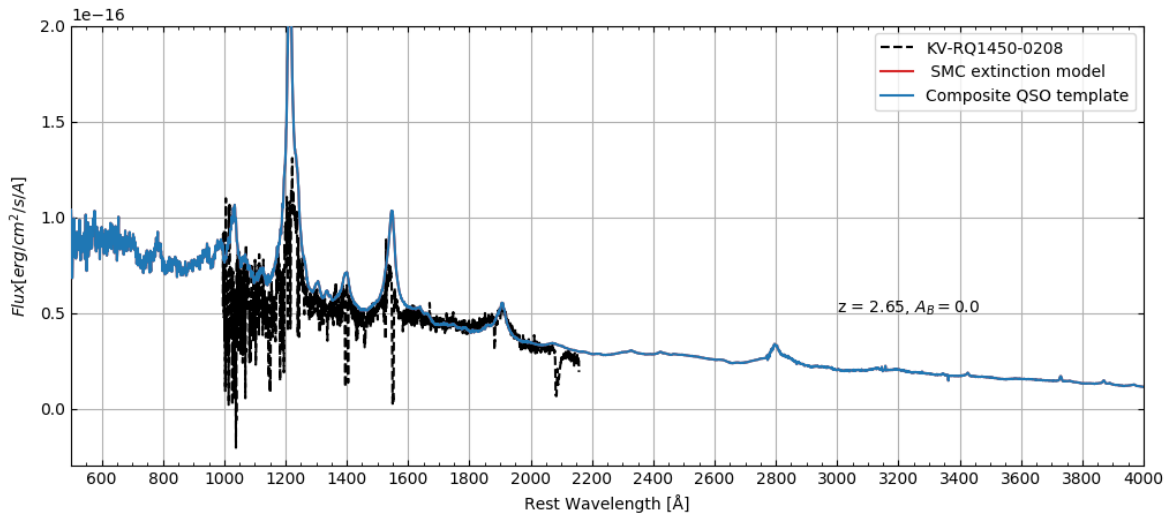


Figure 66: Figure of the spectrum of KV-RQ1143-0118.

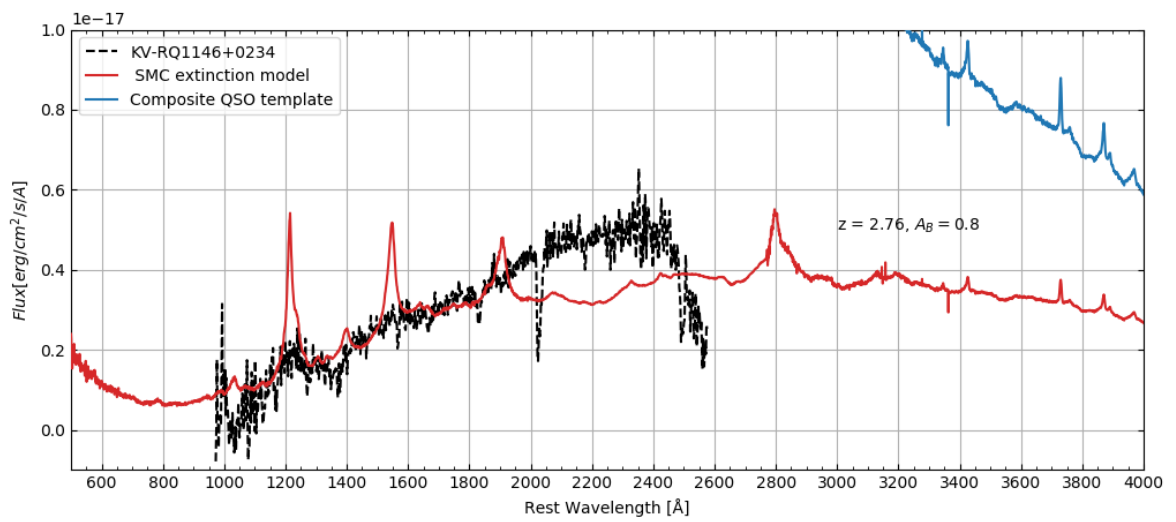


Figure 67: Figure of the spectrum of KV-RQ1146+0234.

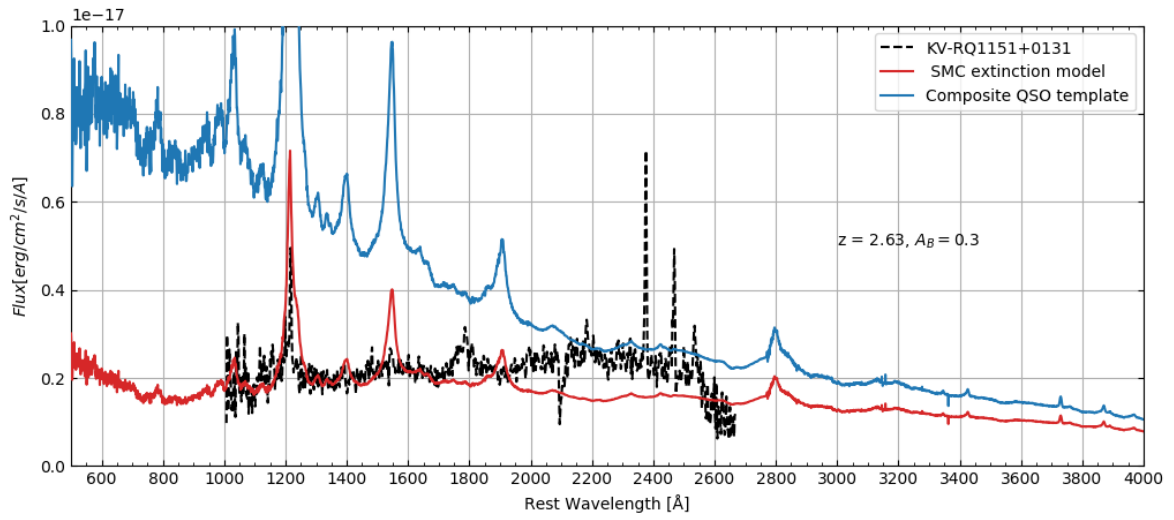


Figure 68: Figure of the spectrum of KV-RQ1151+0131.

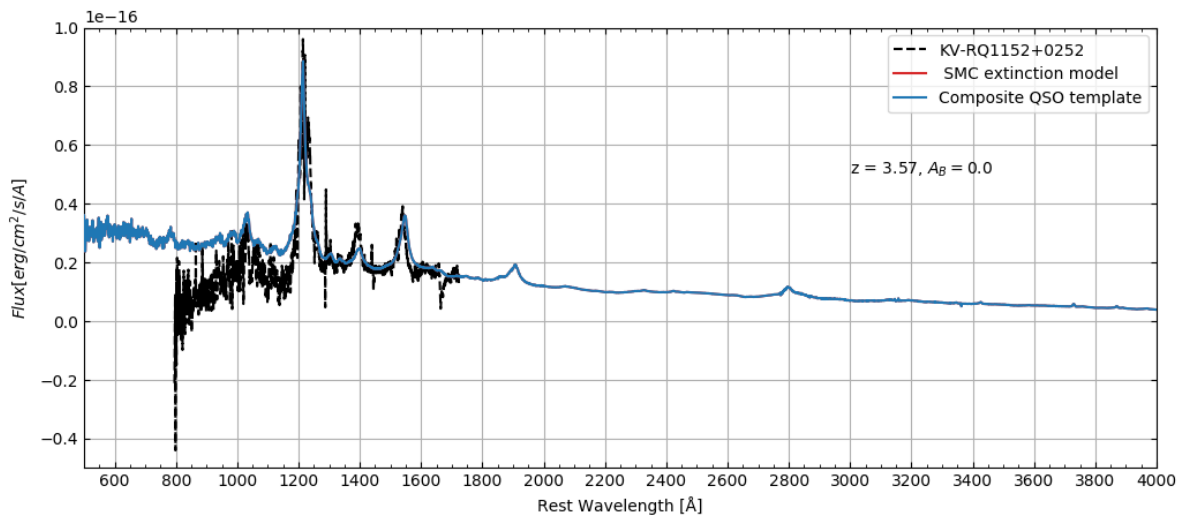


Figure 69: Figure of the spectrum of KV-RQ1152+0252.

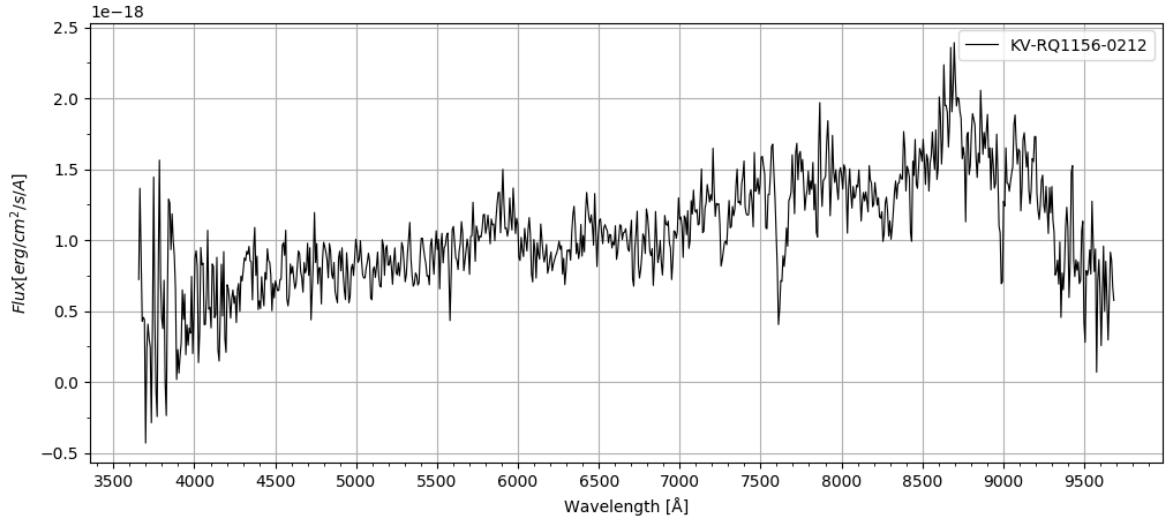


Figure 70: Figure of the spectrum of KV-RQ1156-0212.

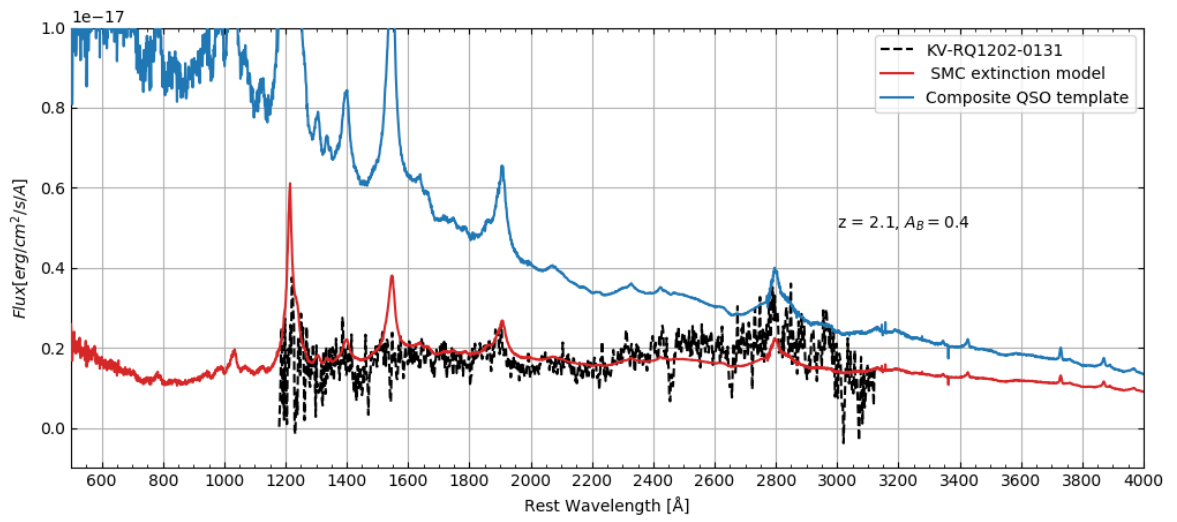


Figure 71: Figure of the spectrum of KV-RQ1202-0131.

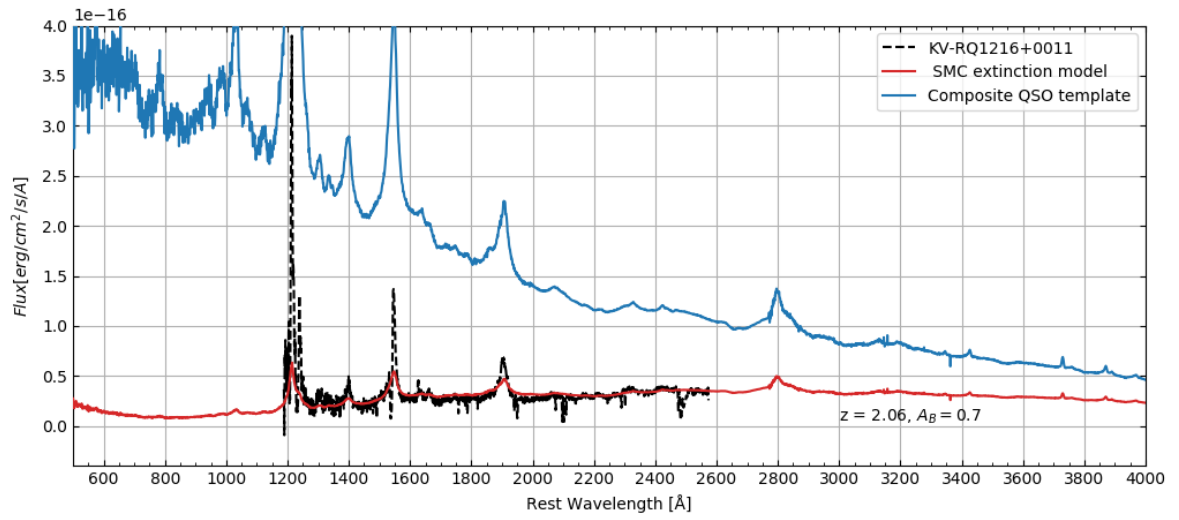


Figure 72: Figure of the spectrum of KV-RQ1216+00111.

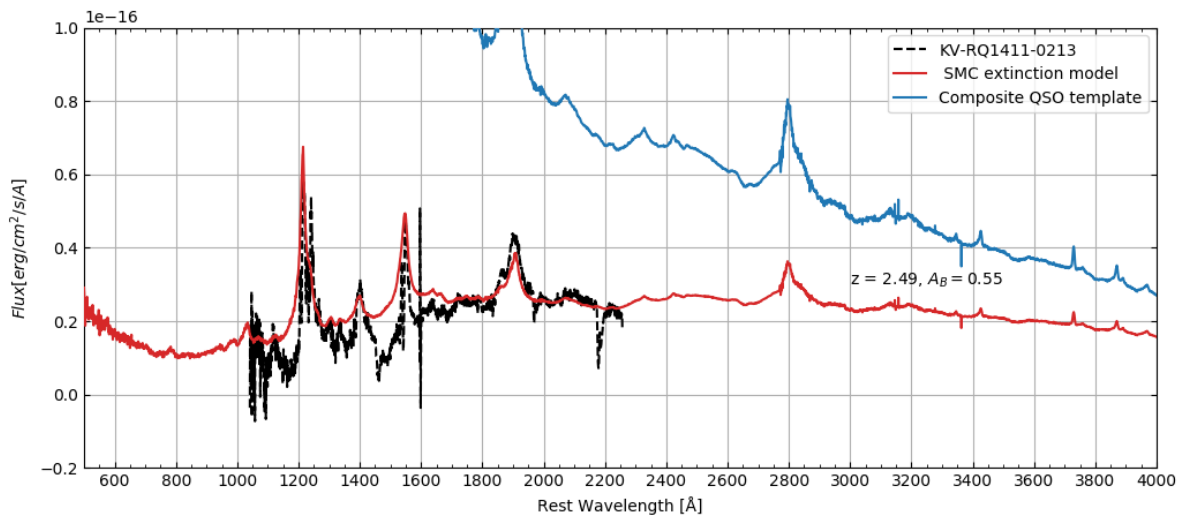


Figure 73: Figure of the spectrum of KV-RQ1411-0213.

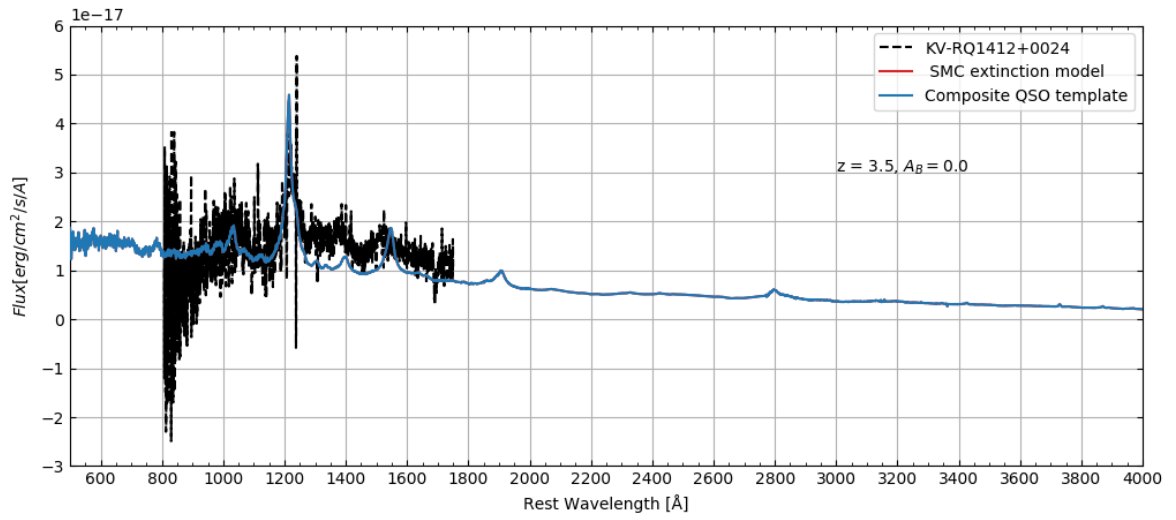


Figure 74: Figure of the spectrum of KV-RQ1412+0024.

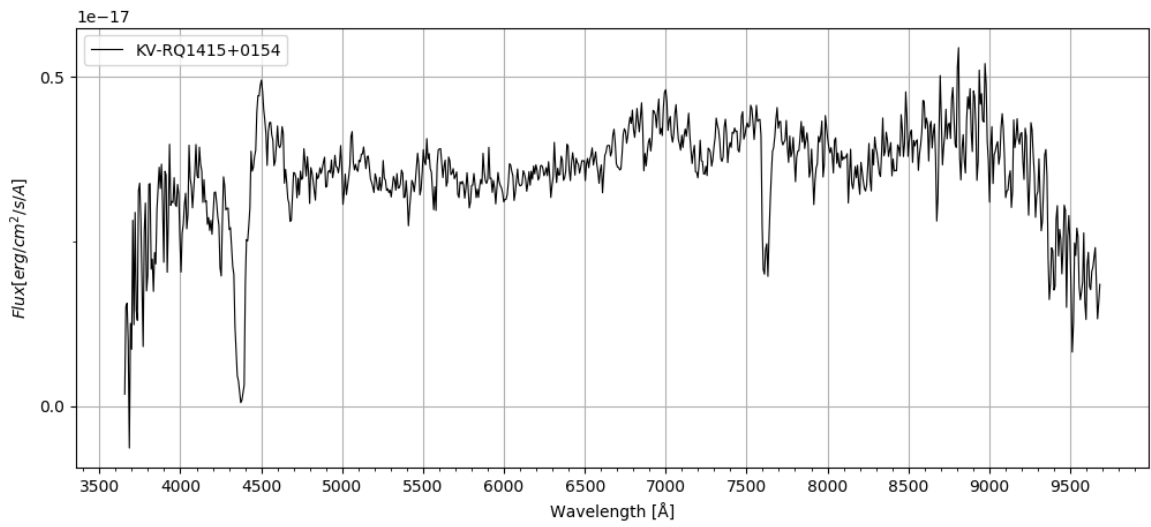


Figure 75: Figure of the spectrum of KV-RQ1415+0154.

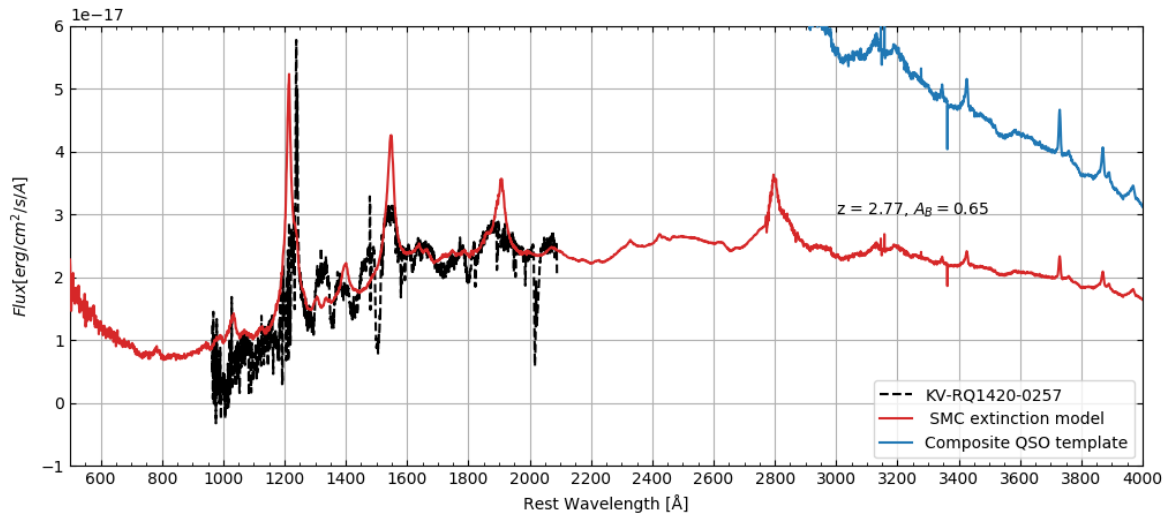


Figure 76: Figure of the spectrum of KV-RQ1420-0257.

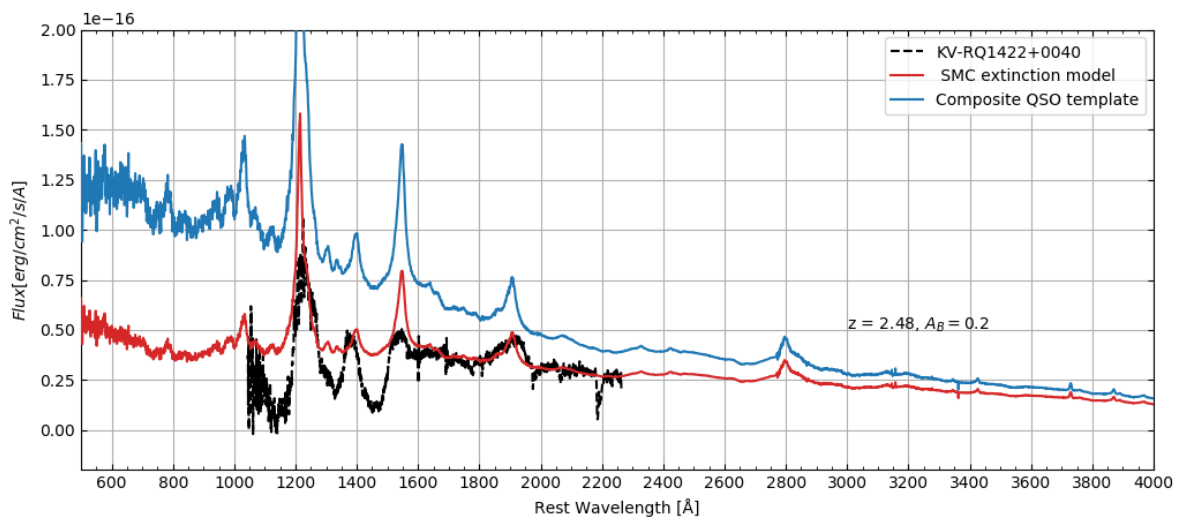


Figure 77: Figure of the spectrum of KV-RQ1422+0040.

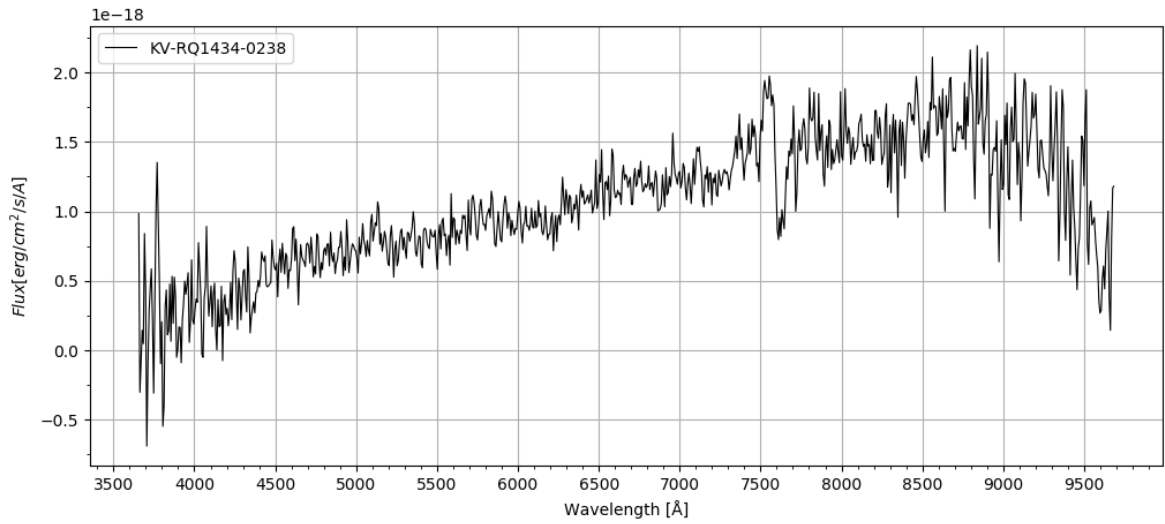


Figure 78: Figure of the spectrum of KV-RQ1434-0238.

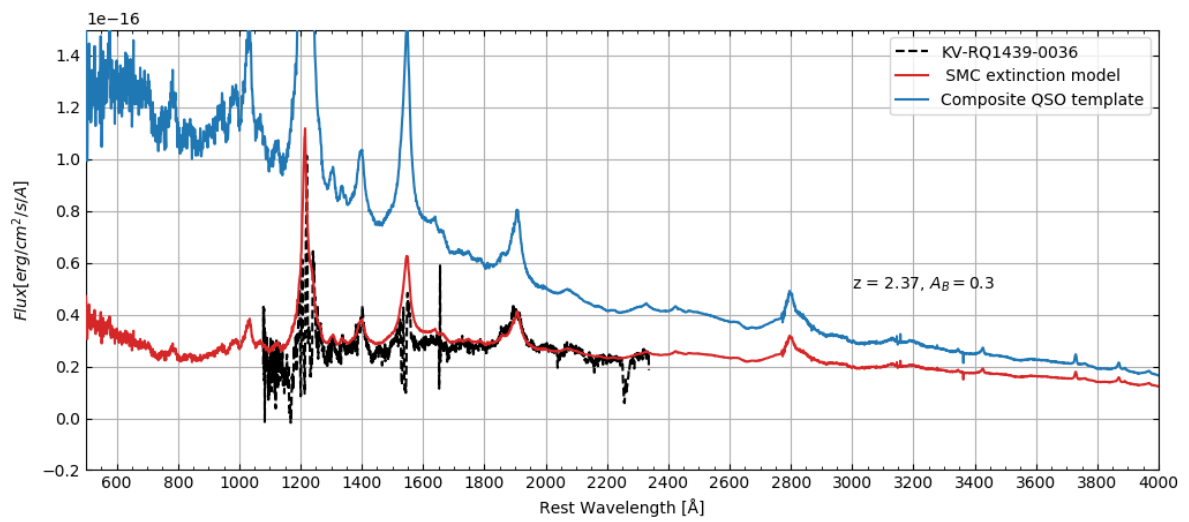


Figure 79: Figure of the spectrum of KV-RQ1439-0036.

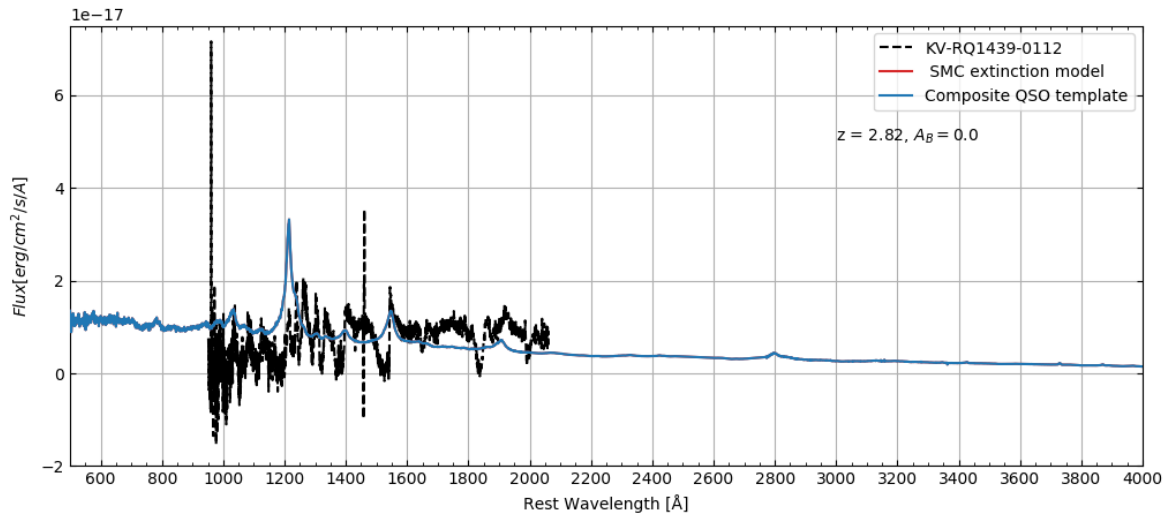


Figure 80: Figure of the spectrum of KV-RQ1439-0112.

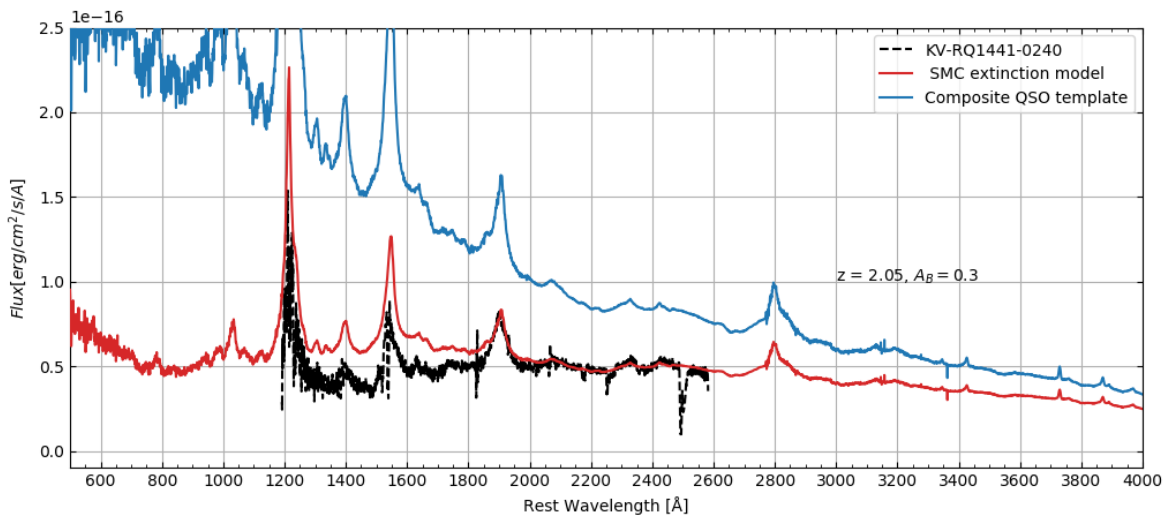


Figure 81: Figure of the spectrum of KV-RQ1441-0240.

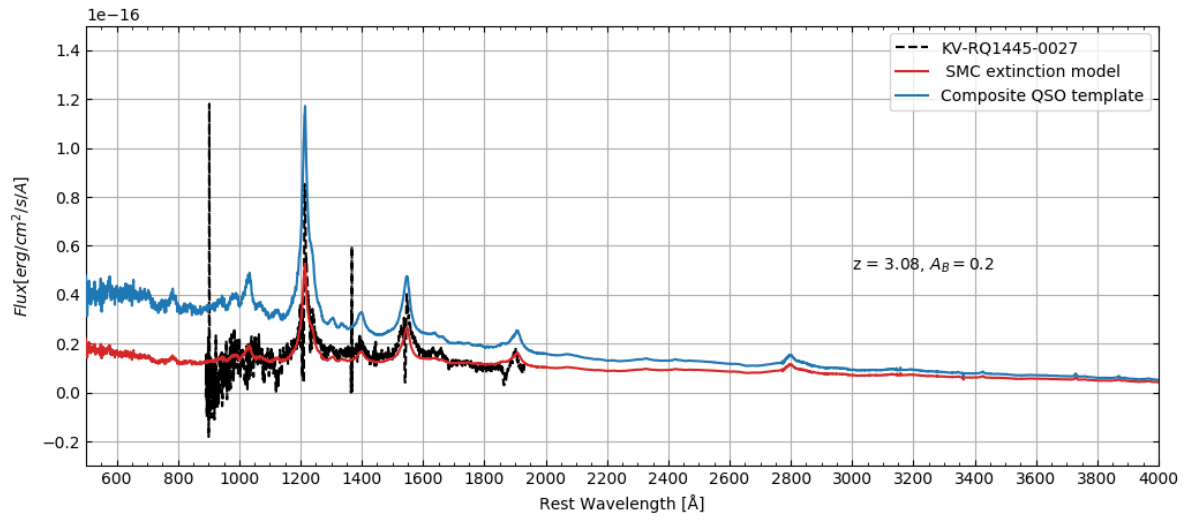


Figure 82: Figure of the spectrum of KV-RQ1445-0027.

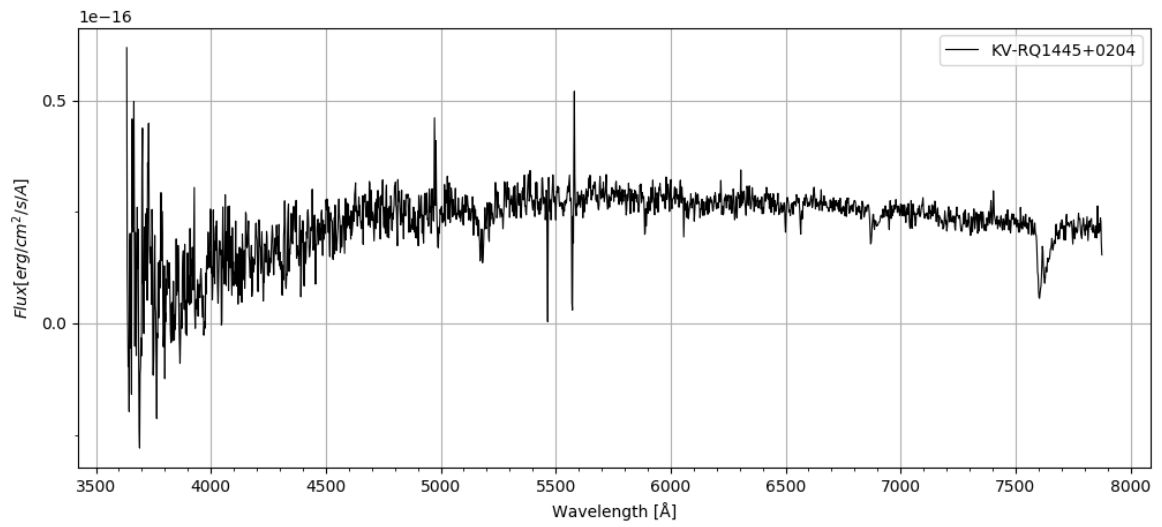


Figure 83: Figure of the spectrum of KV-RQ1445+0204.

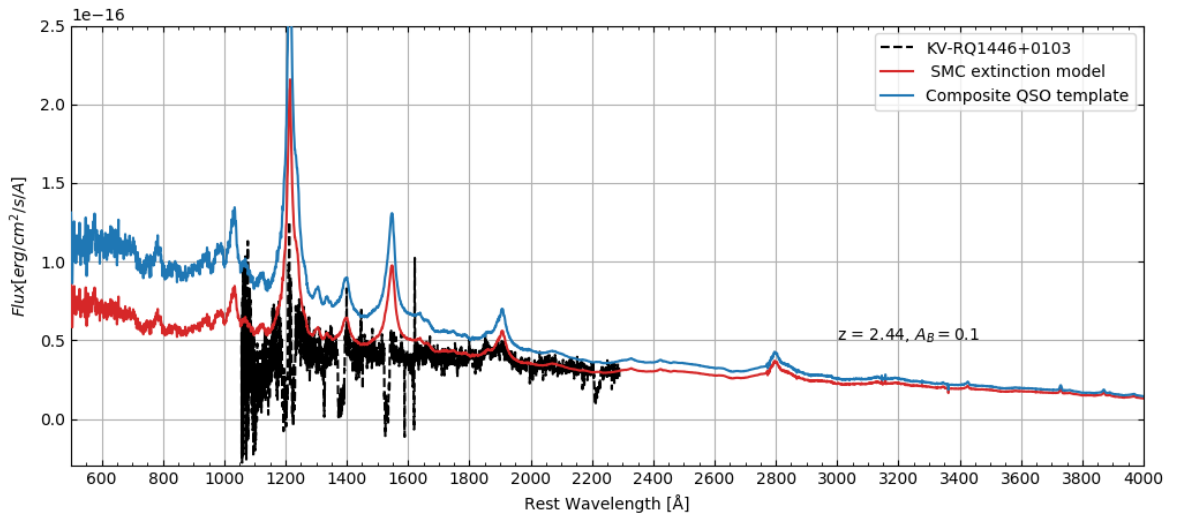


Figure 84: Figure of the spectrum of KV-RQ1446+0103.

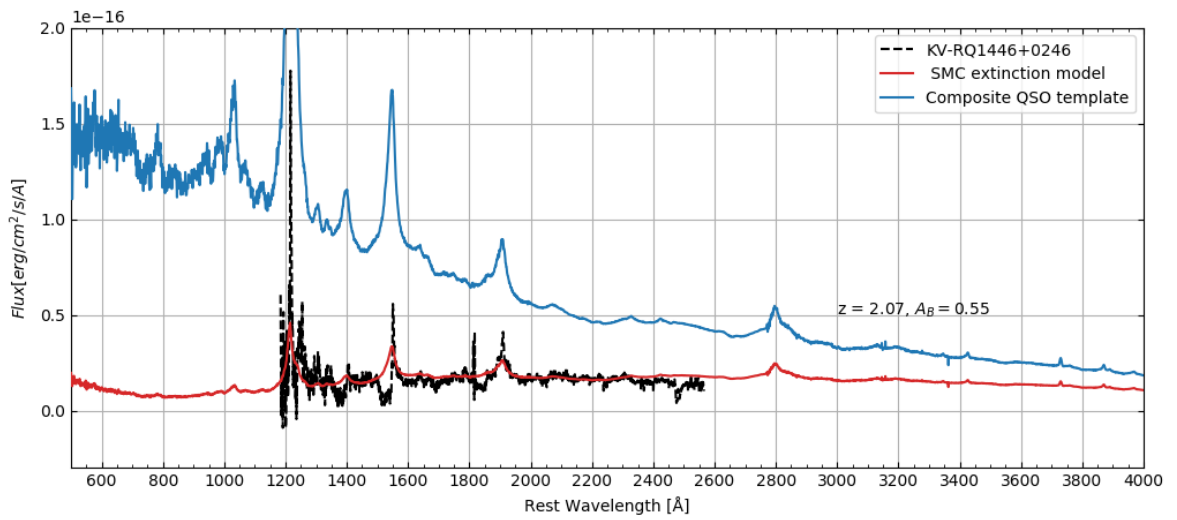


Figure 85: Figure of the spectrum of KV-RQ1446+0246.

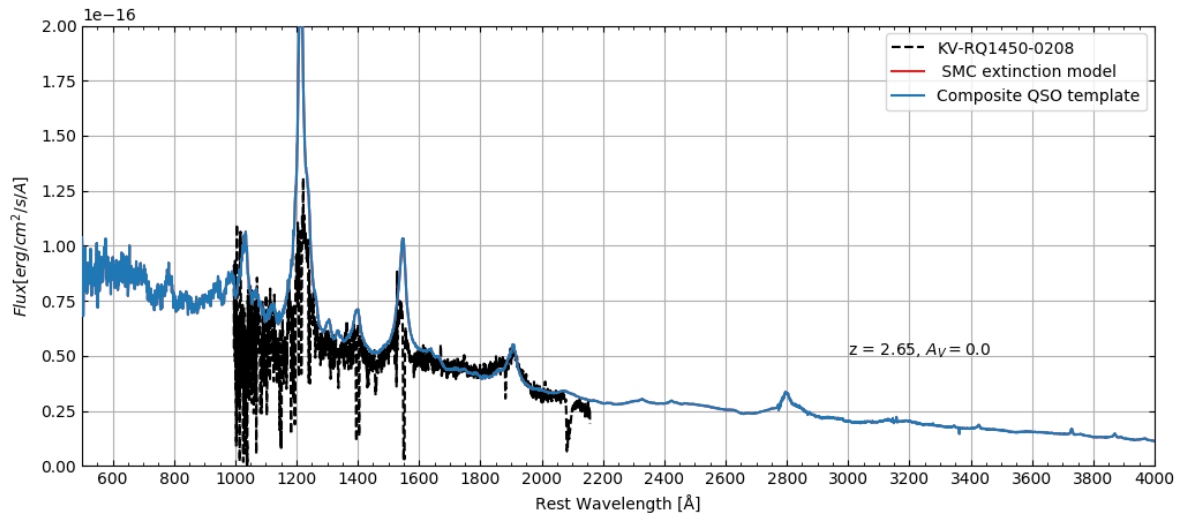


Figure 86: Figure of the spectrum of KV-RQ1450-0208 .

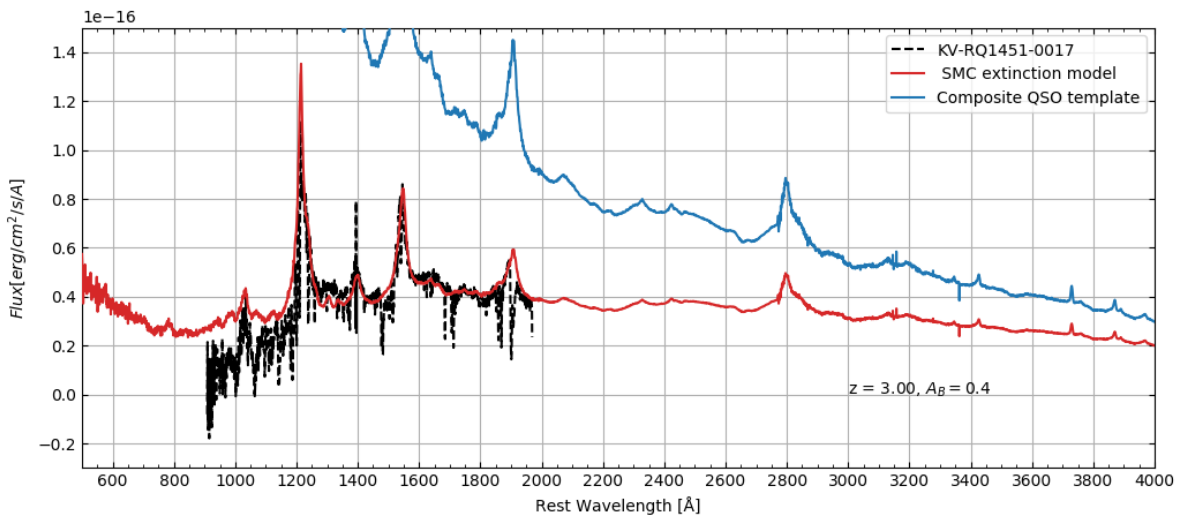


Figure 87: Figure of the spectrum of KV-RQ1451-0017.

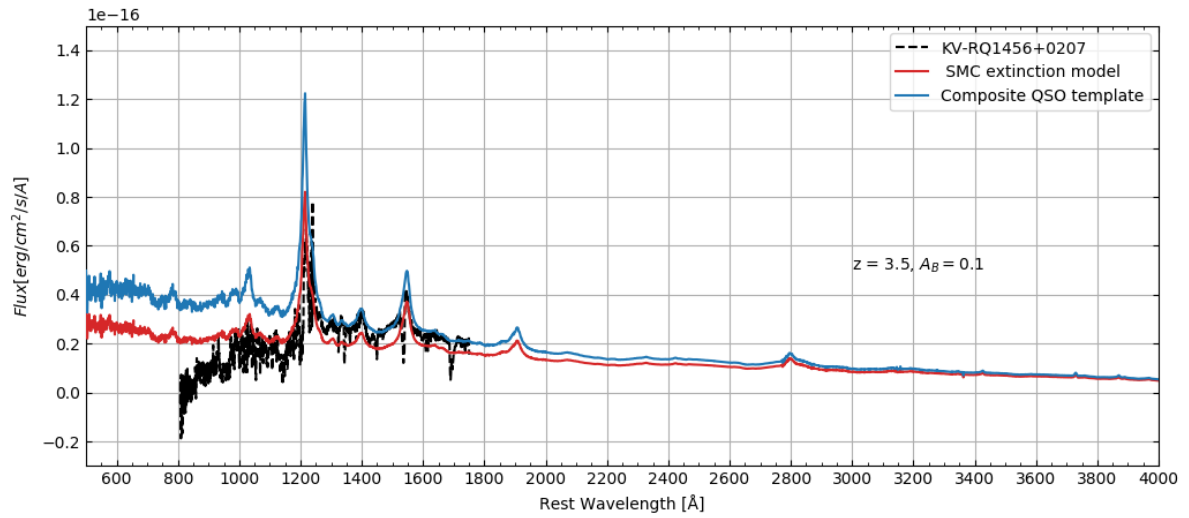


Figure 88: Figure of the spectrum of KV-RQ1456+0207.

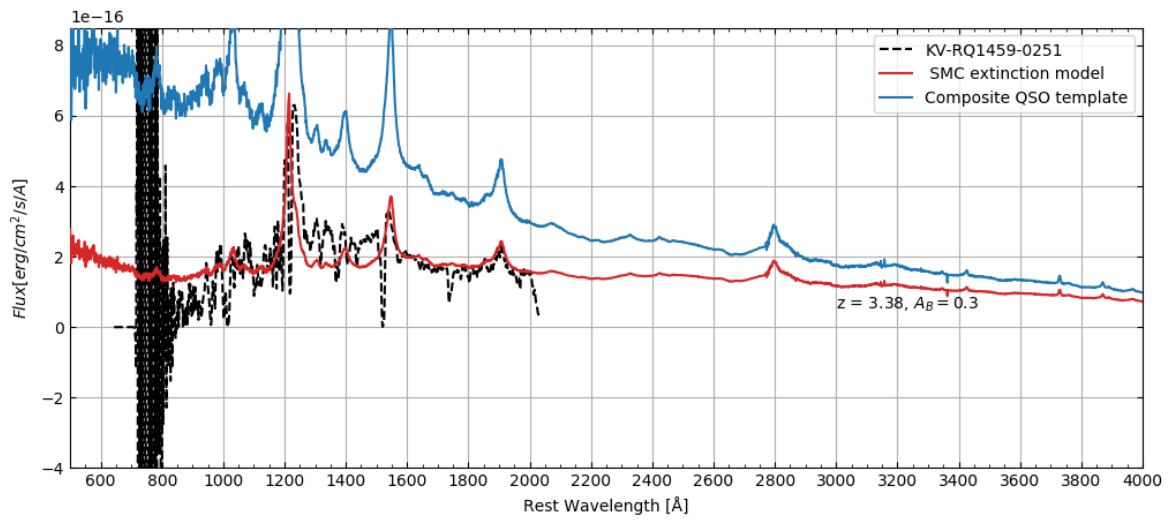


Figure 89: Figure of the spectrum of KV-RQ1459-0251.

The spectrum data of KV-RQ1459-0258 has a problem with flux scales.

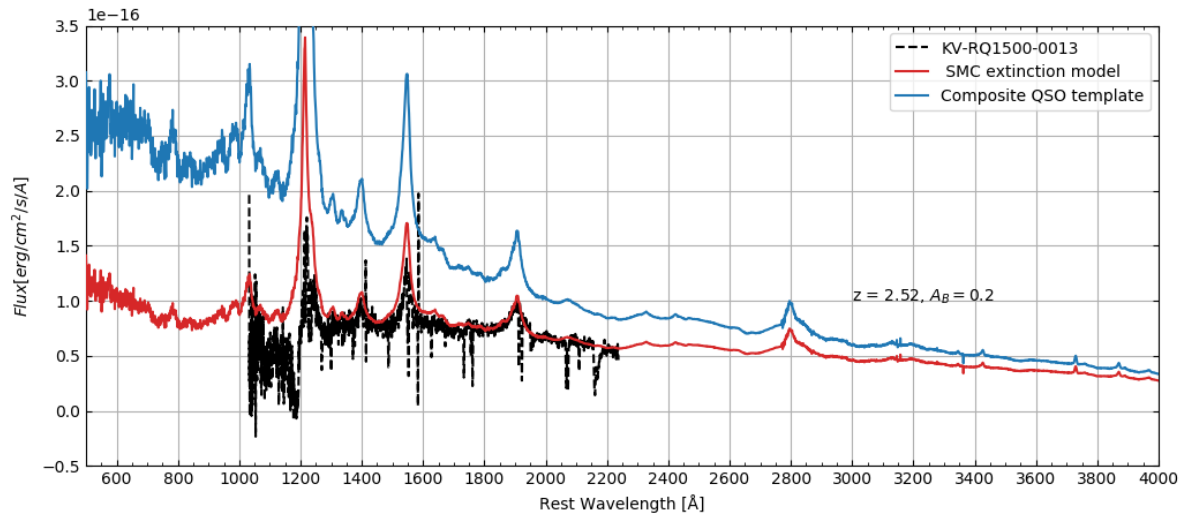


Figure 90: Figure of the spectrum of KV-RQ1500-0013.

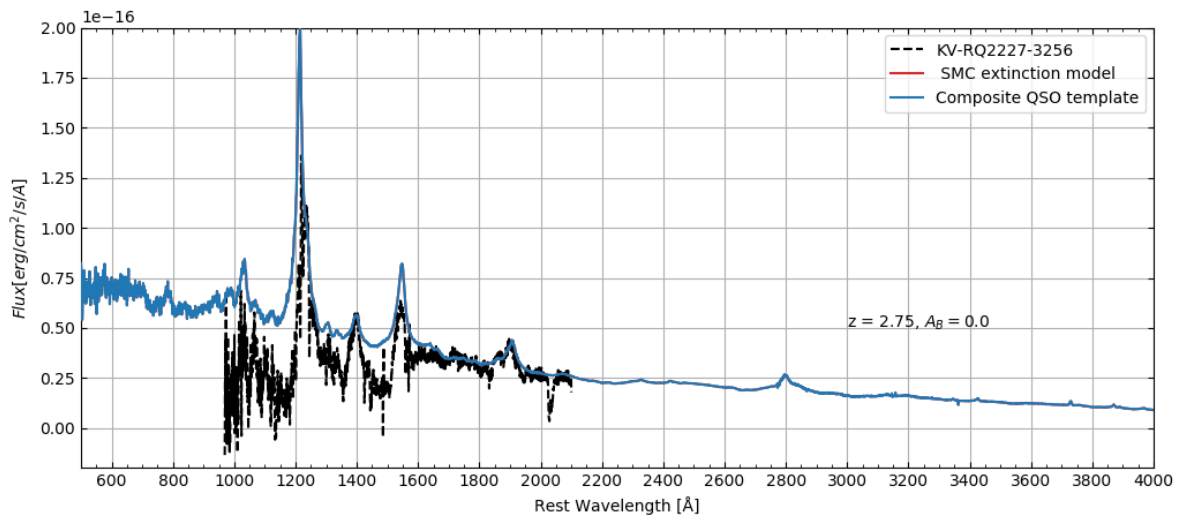


Figure 91: Figure of the spectrum of KV-RQ2227-3256.

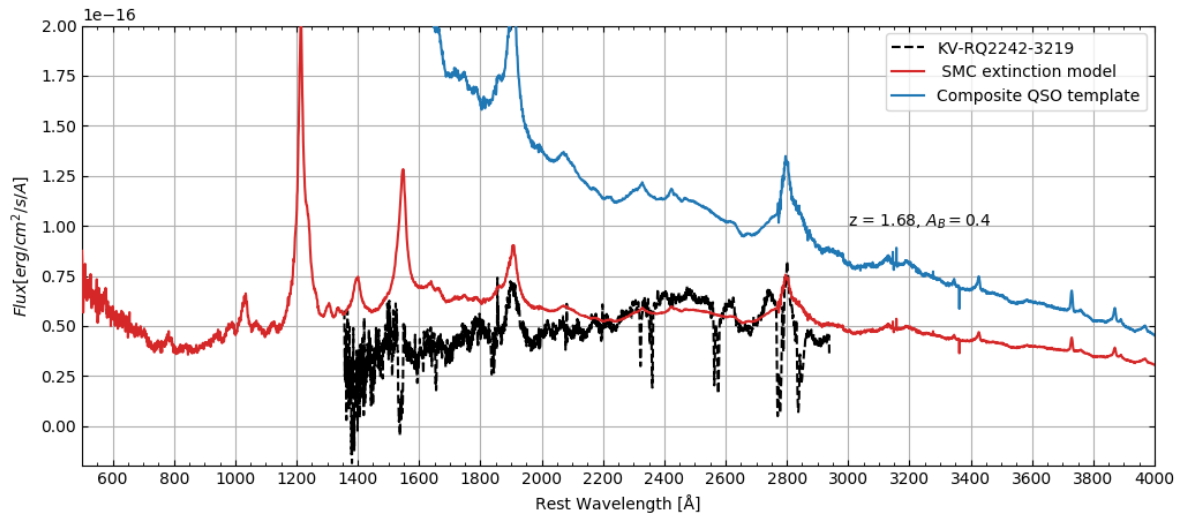


Figure 92: Figure of the spectrum of KV-RQ2242-3219.

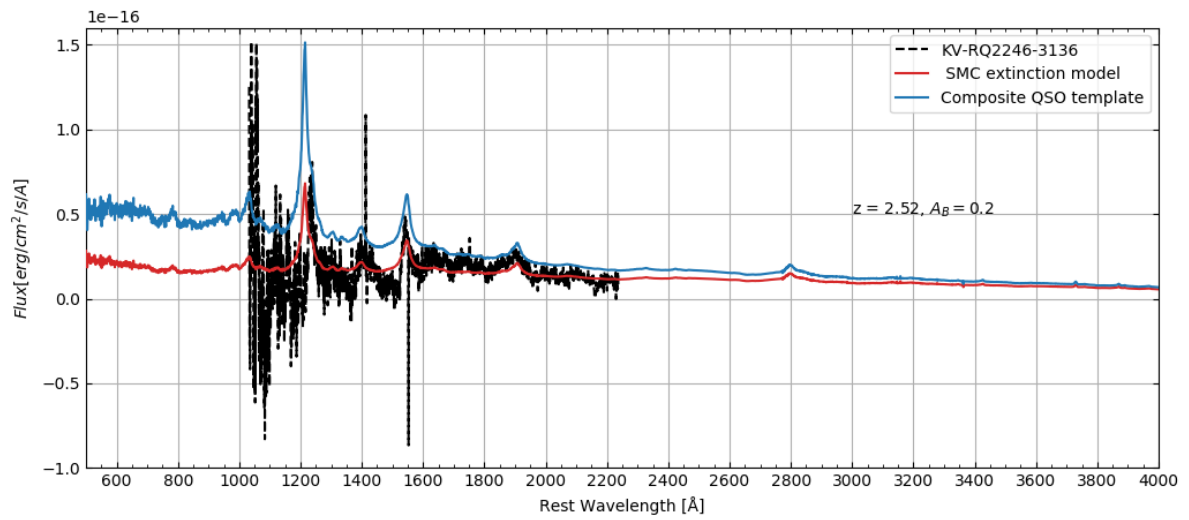


Figure 93: Figure of the spectrum of KV-RQ2246-3136.

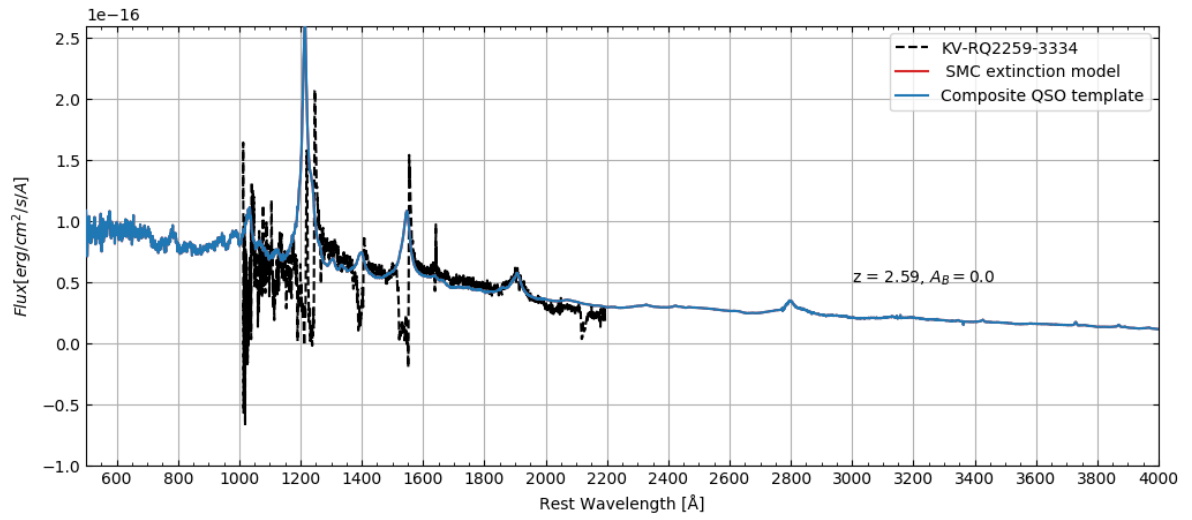


Figure 94: Figure of the spectrum of KV-RQ2259-3334.

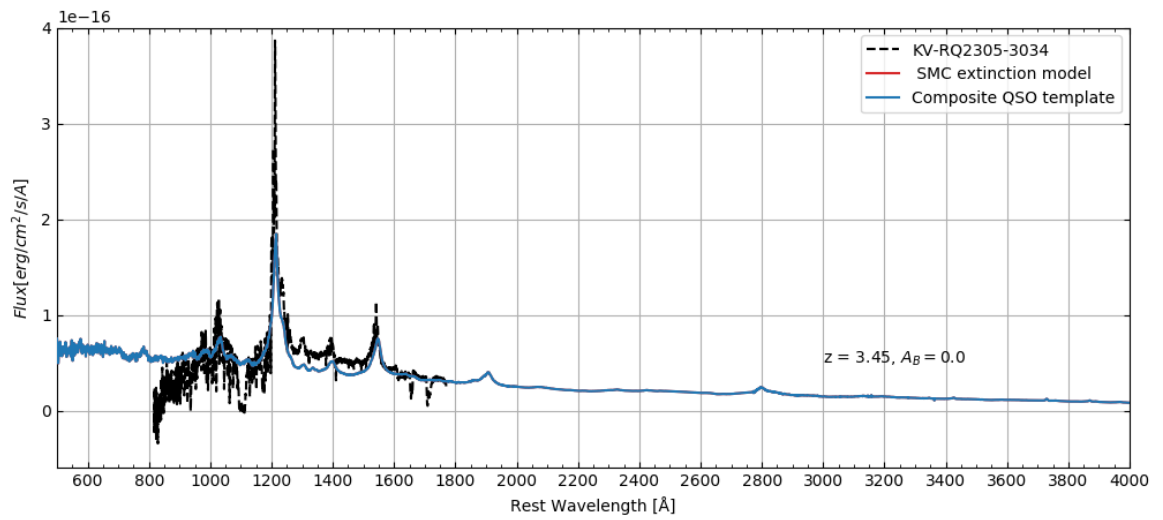


Figure 95: Figure of the spectrum of KV-RQ2305-3034.

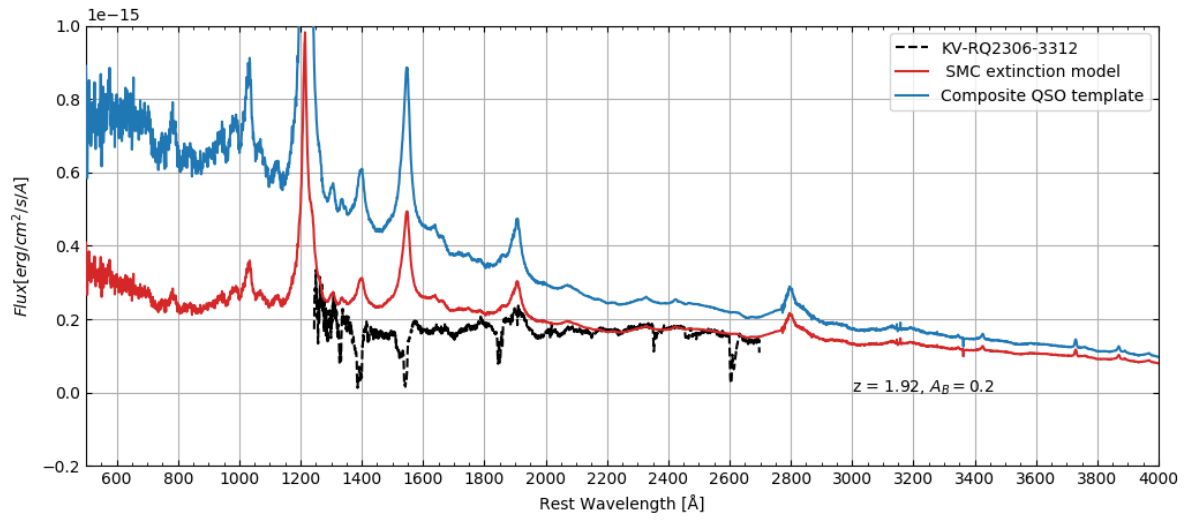


Figure 96: Figure of the spectrum of KV-RQ2306-3312.

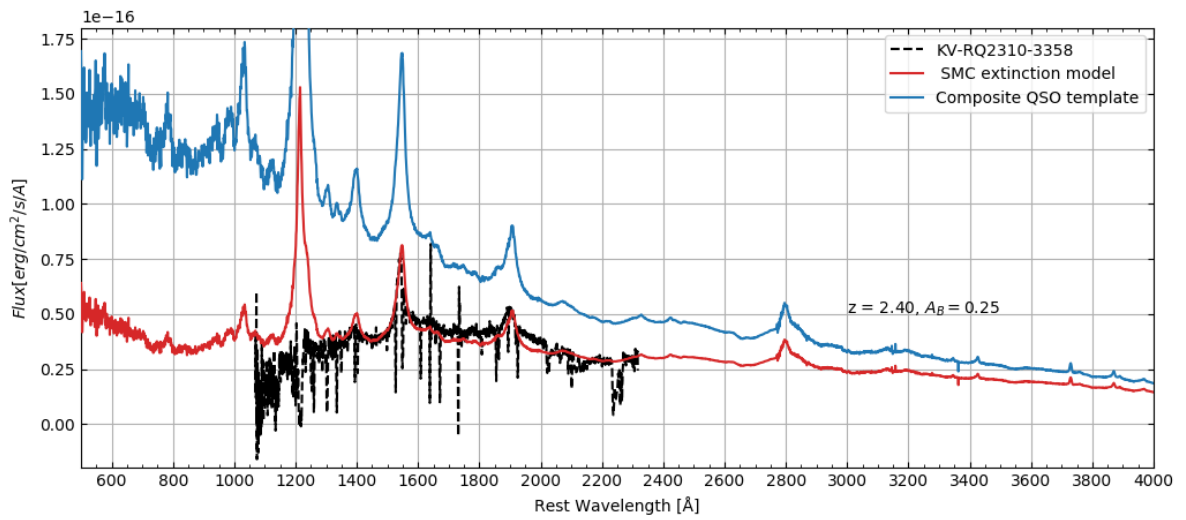


Figure 97: Figure of the spectrum of KV-RQ2310-3358.

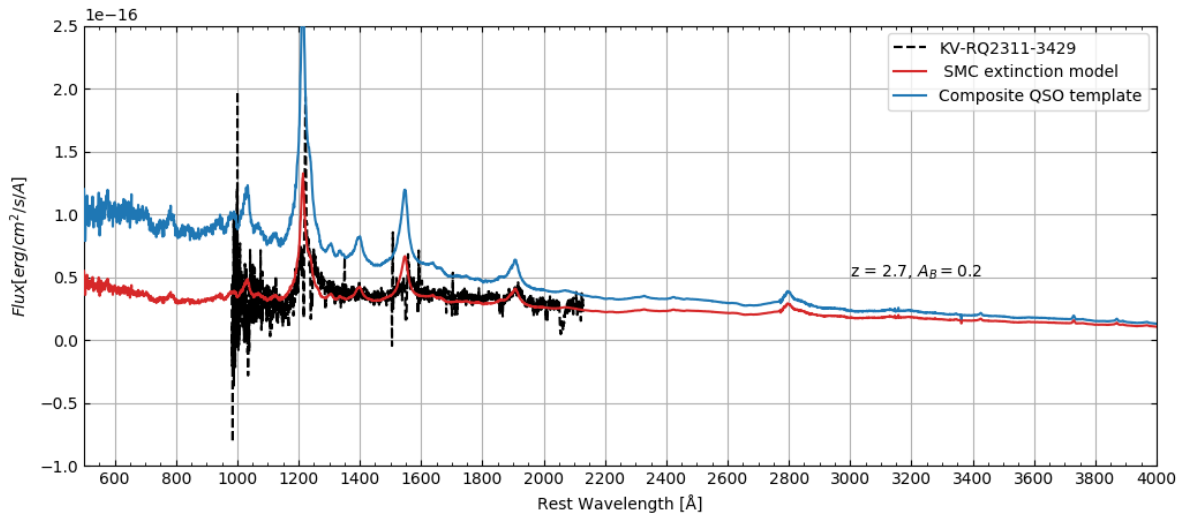


Figure 98: Figure of the spectrum of KV-RQ2311-3429.

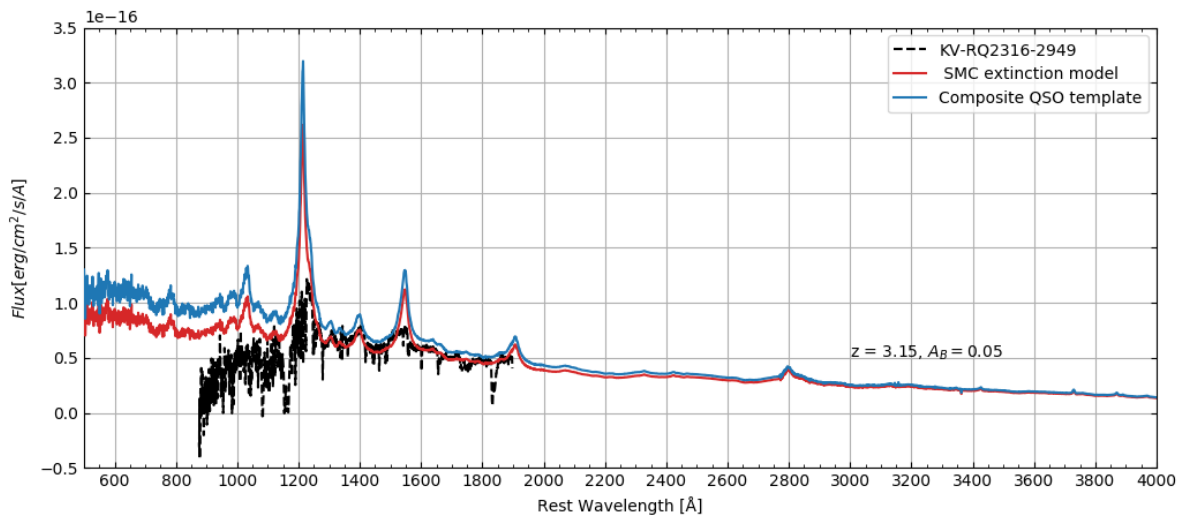


Figure 99: Figure of the spectrum of KV-RQ2316-2949.

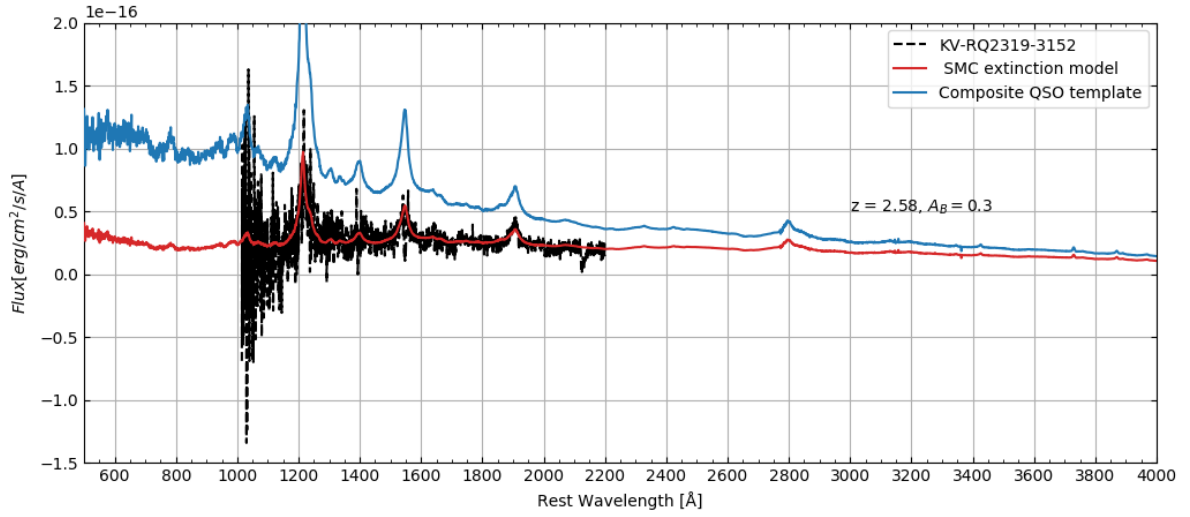


Figure 100: Figure of the spectrum of KV-RQ2319-3152.

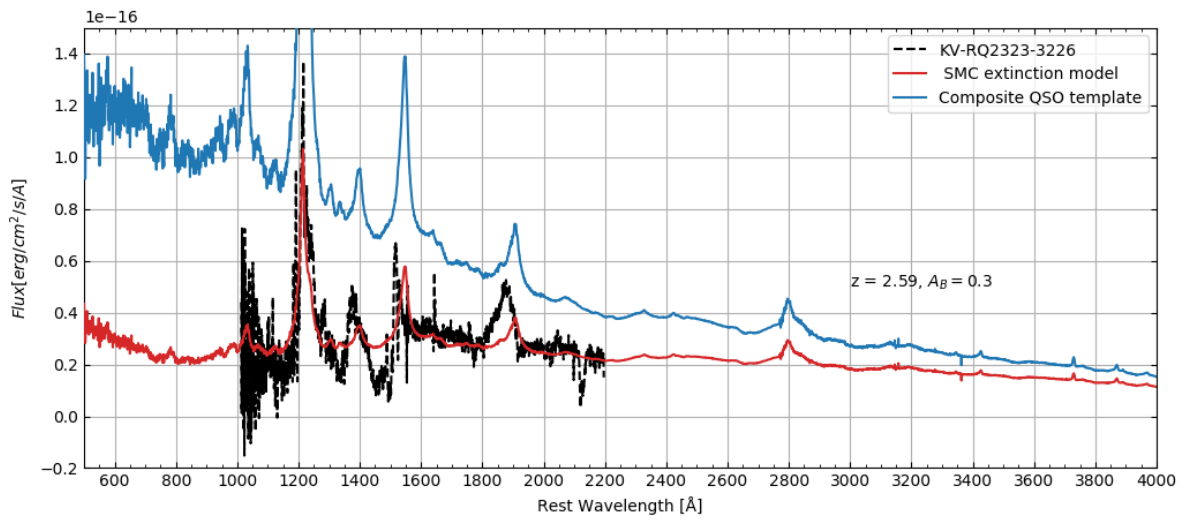


Figure 101: Figure of the spectrum of KV-RQ2323-3226.

The spectrum of KV-RQ2328-3231 is missing.

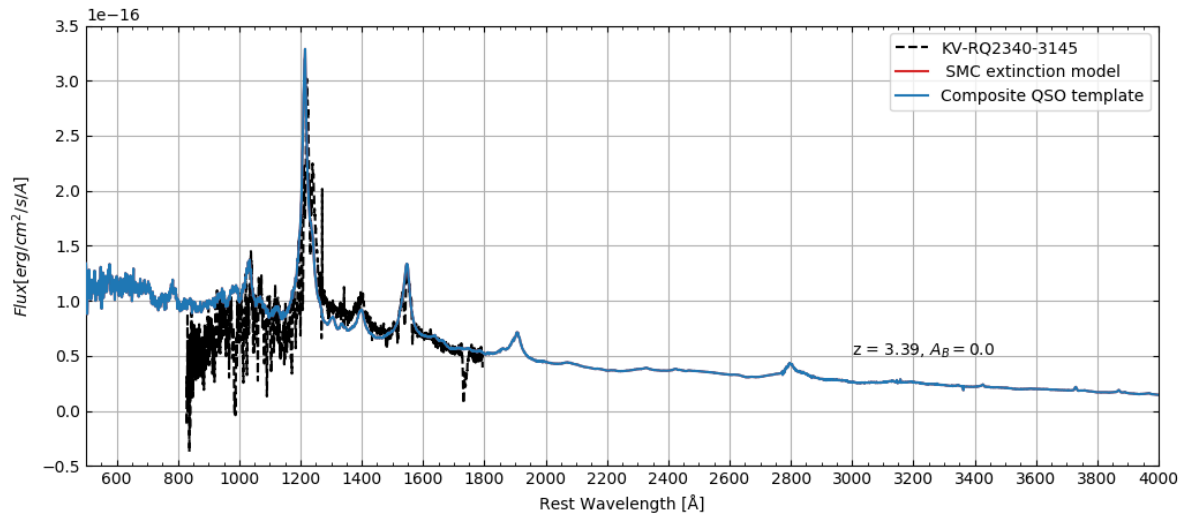


Figure 102: Figure of the spectrum of KV-RQ2340-3145.

KVRQ - red observed:
 The spectrum of KV-RQ0834+012 is missing.

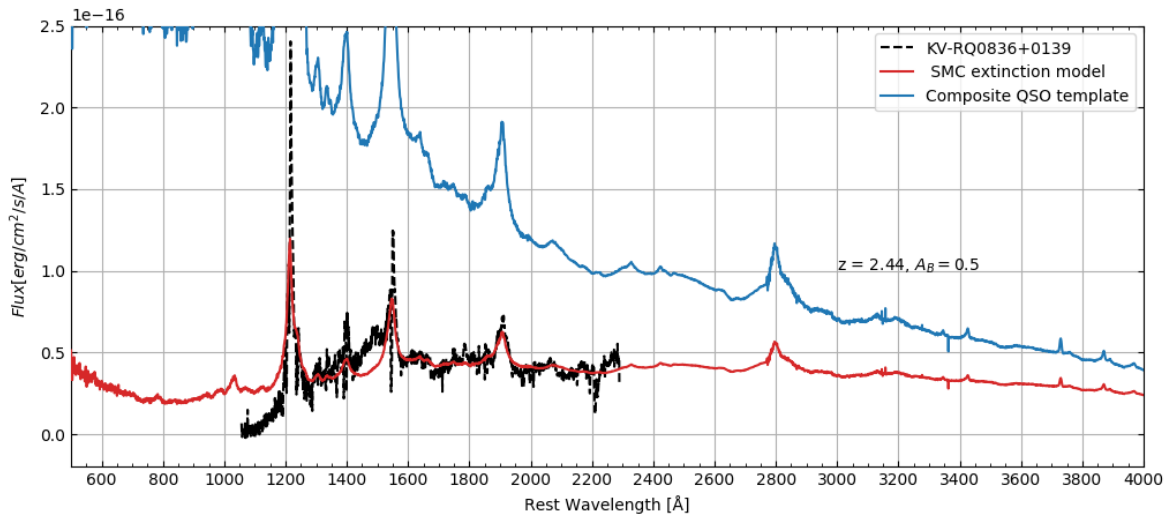


Figure 103: Figure of the spectrum of KV-RQ0836+0139.

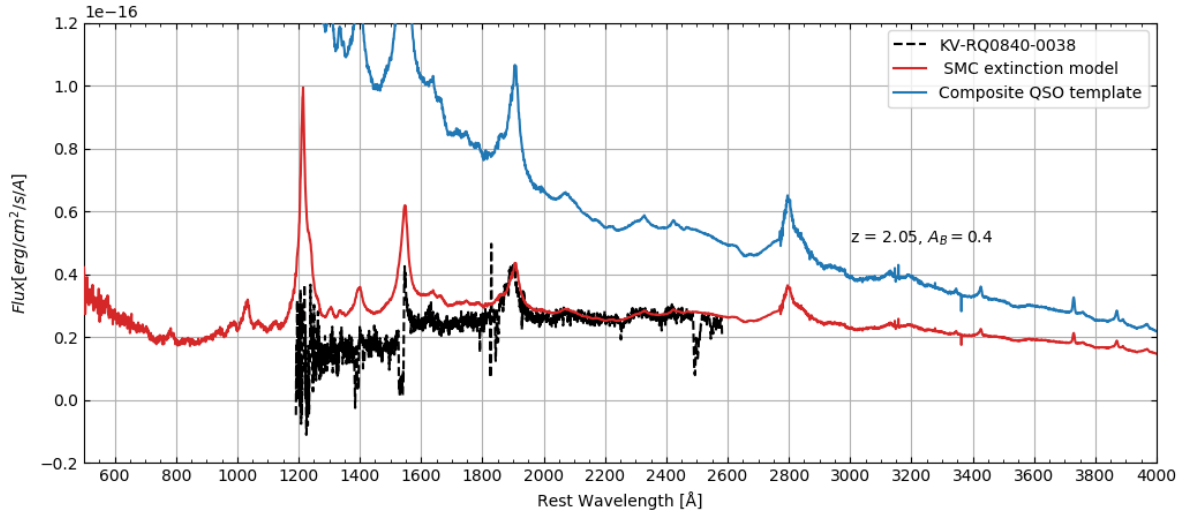


Figure 104: Figure of the spectrum of KV-RQ0840-0038.

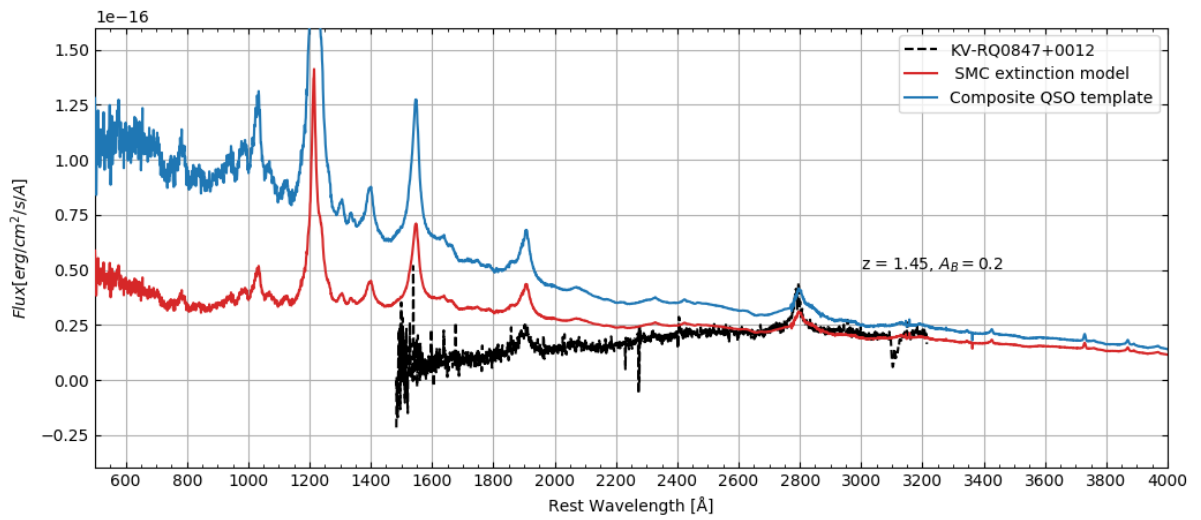


Figure 105: Figure of the spectrum of KV-RQ0847+0012.

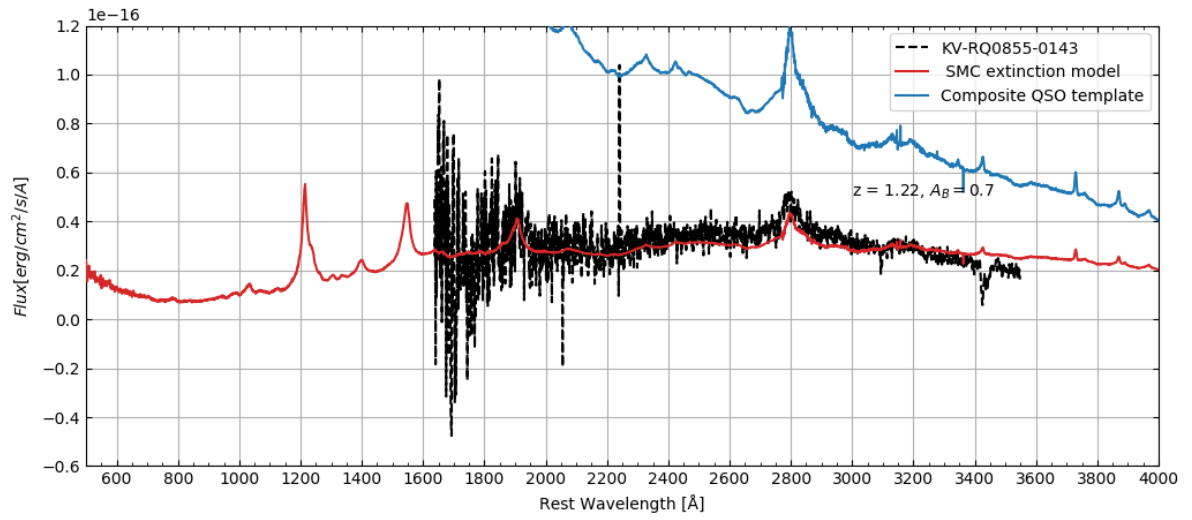


Figure 106: Figure of the spectrum of KV-RQ0855-0143.

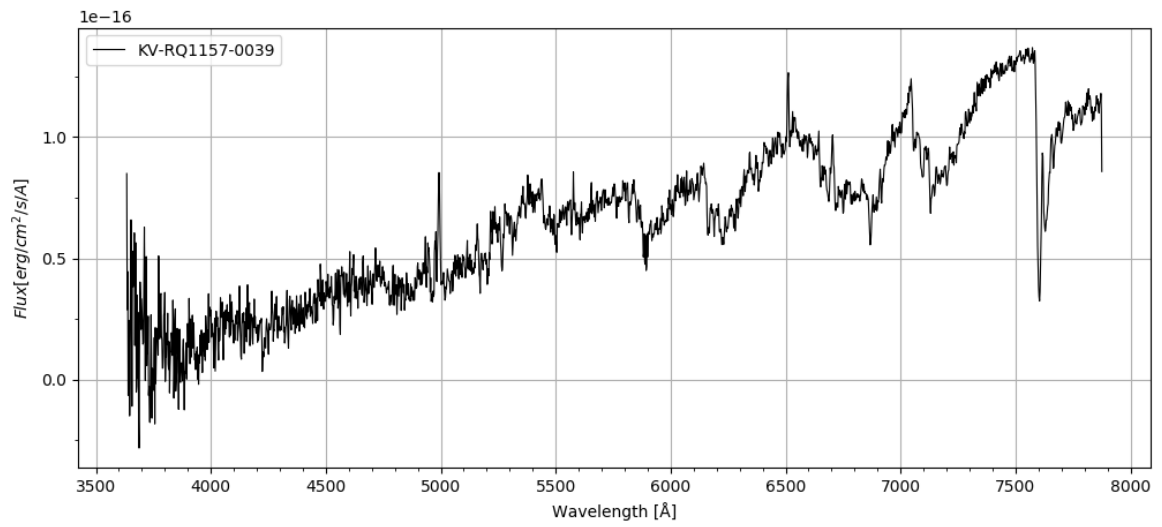


Figure 107: Figure of the spectrum of KV-RQ1157-0039.

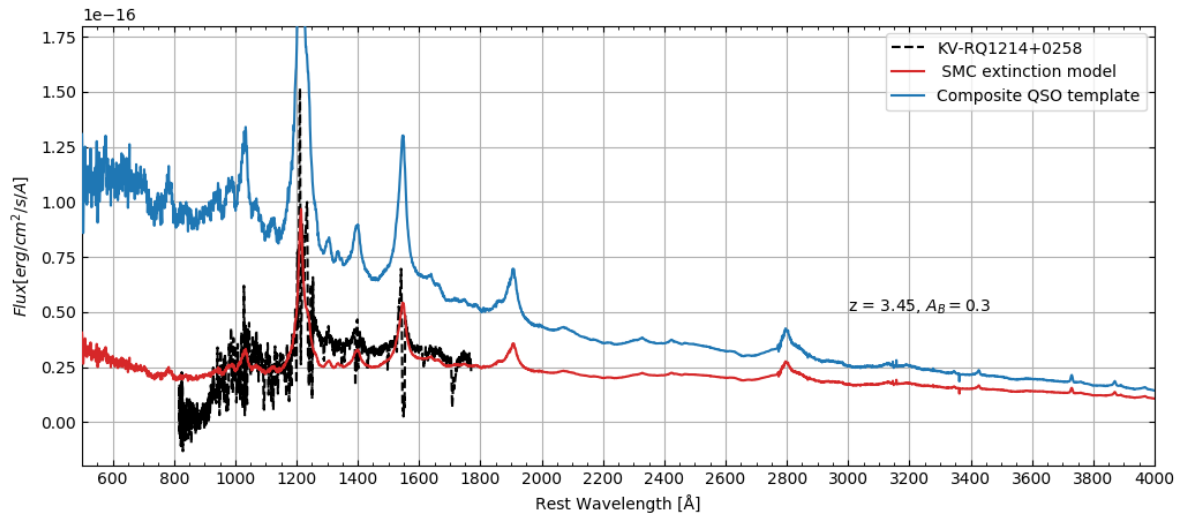


Figure 108: Figure of the spectrum of KV-RQ1214+0258.

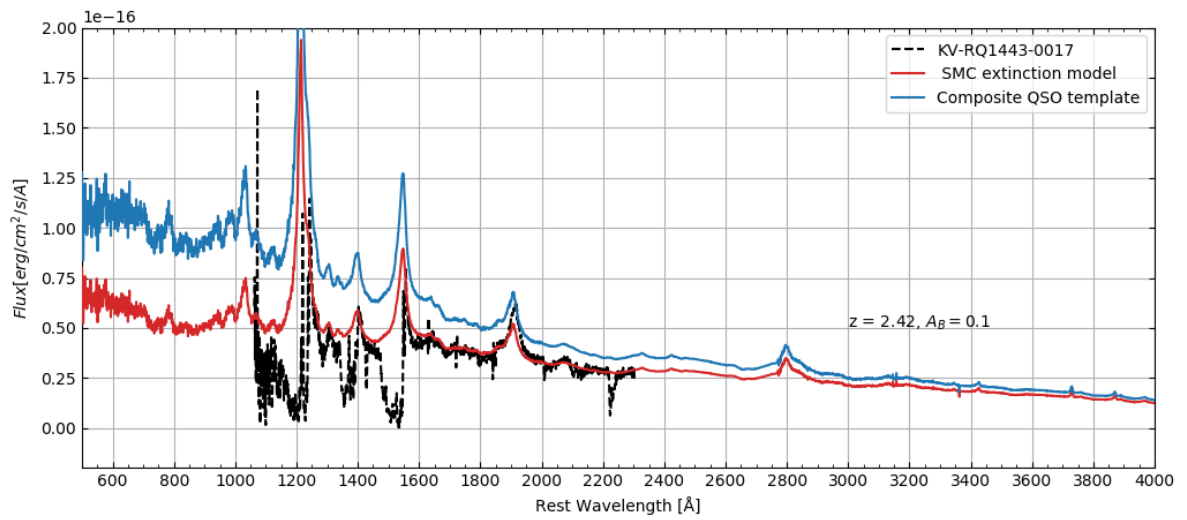


Figure 109: Figure of the spectrum of KV-RQ1443-0017.

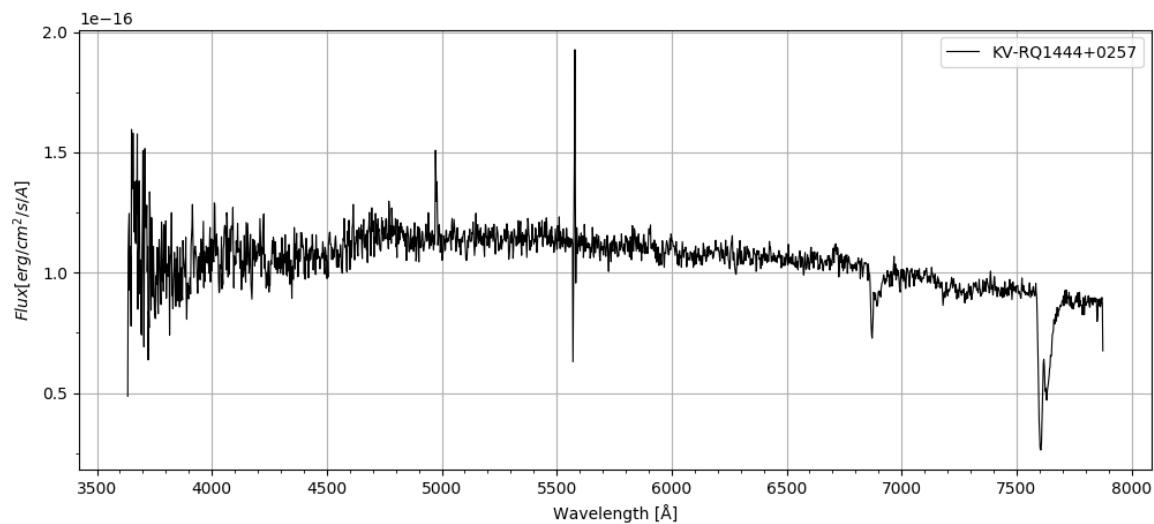


Figure 110: Figure of the spectrum of KV-RQ1444+0257.

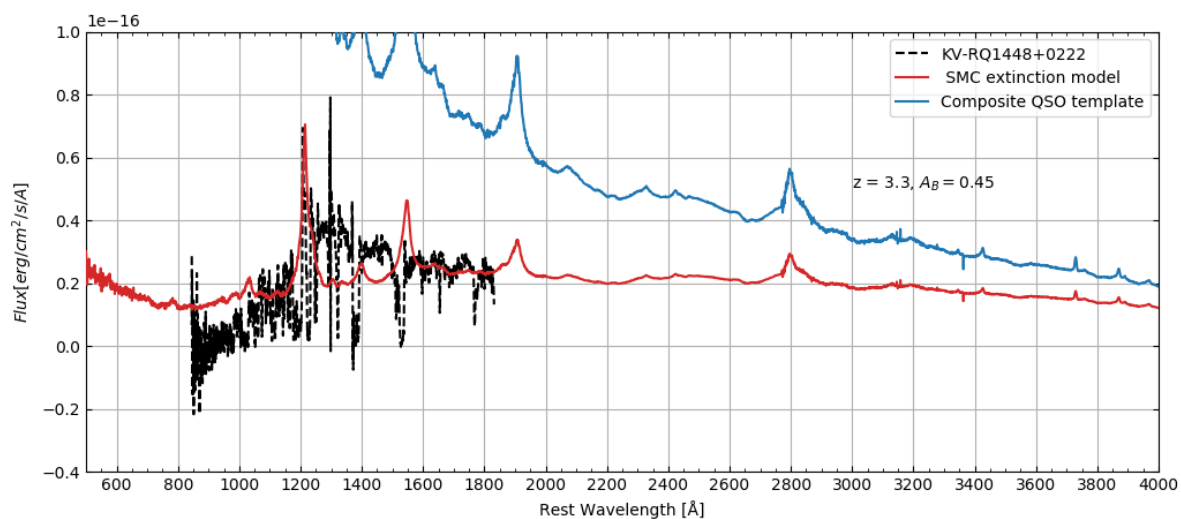


Figure 111: Figure of the spectrum of KV-RQ1448+0222.

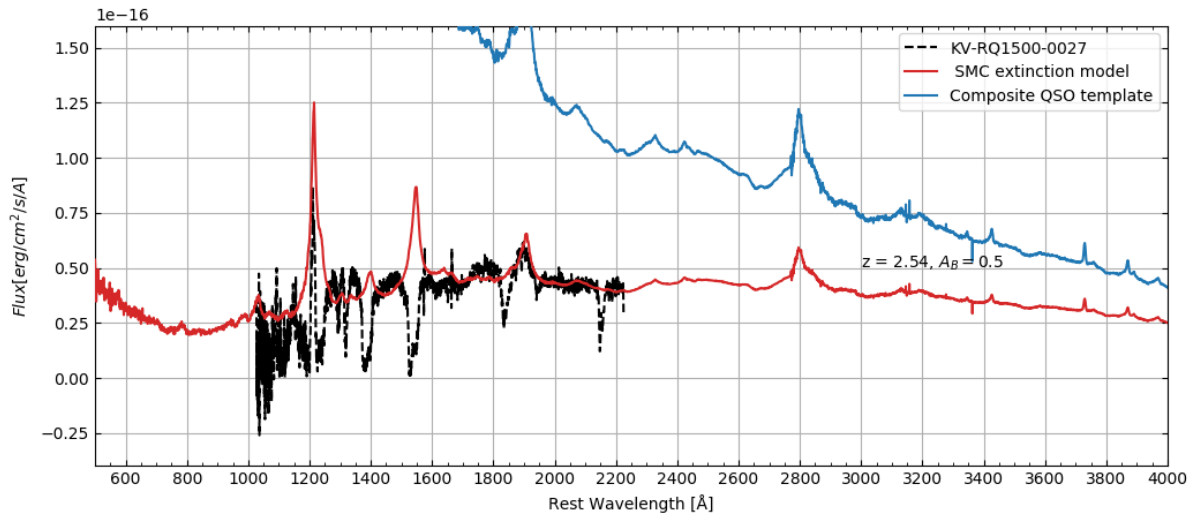


Figure 112: Figure of the spectrum of KV-RQ1500-0027.

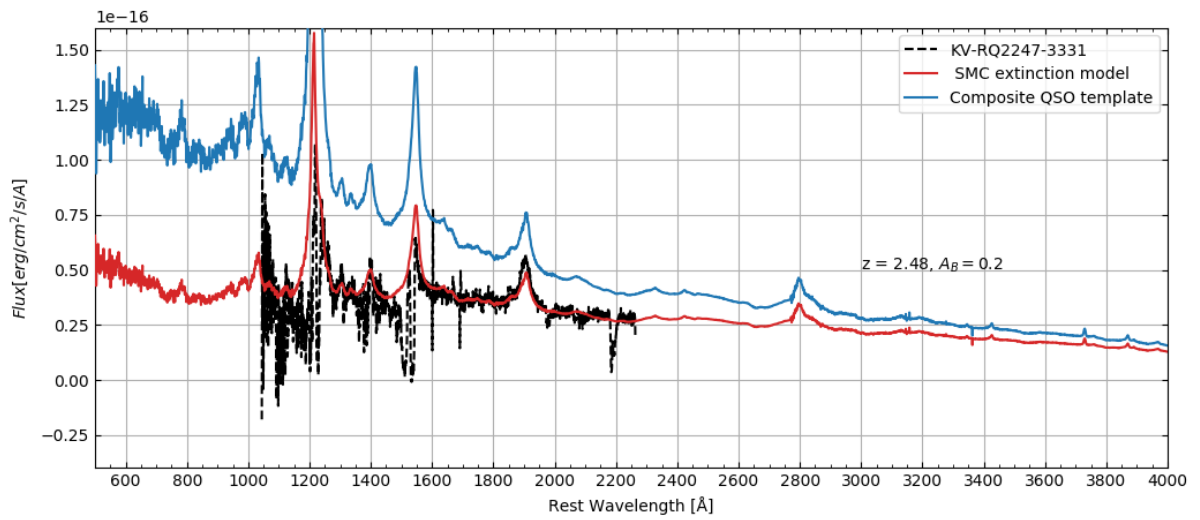


Figure 113: Figure of the spectrum of KV-RQ2247-3331.

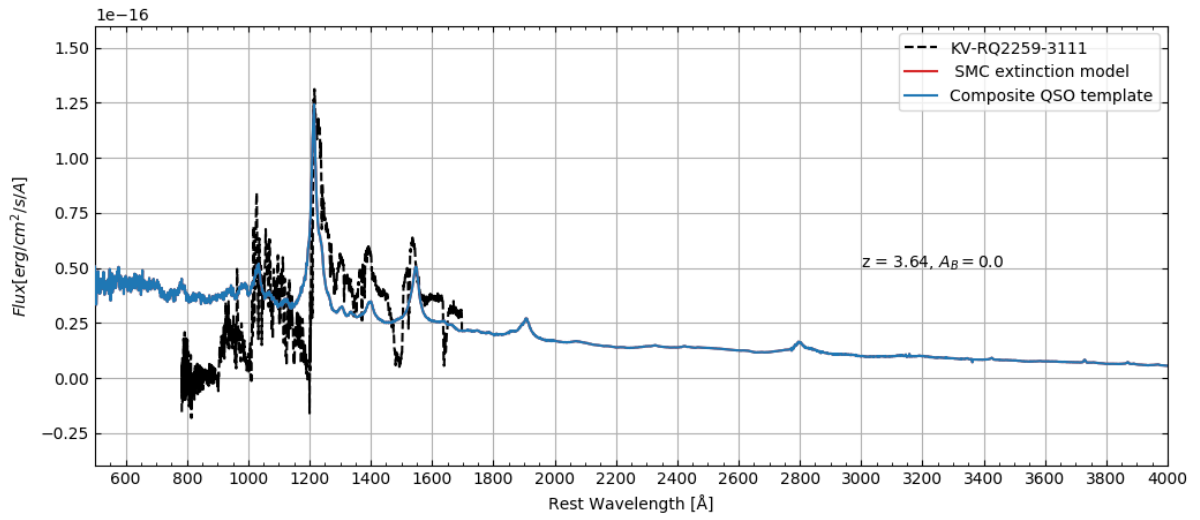


Figure 114: Figure of the spectrum of KV-RQ2259-3111.

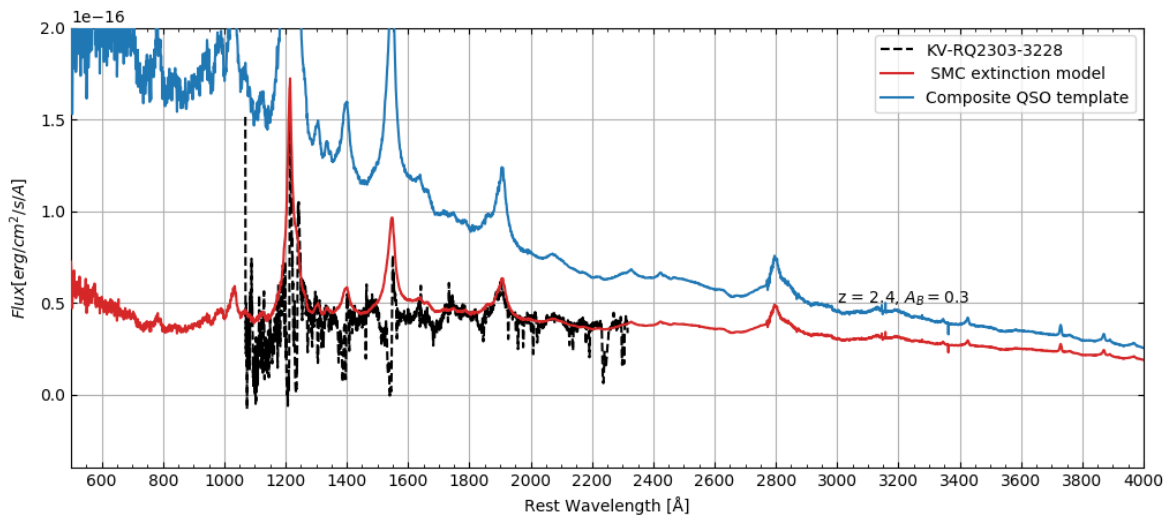


Figure 115: Figure of the spectrum of KV-RQ2303-3228.

7.5 The script: Dust extinction model

```

#####
from astropy.io import ascii;

import numpy as np;
import matplotlib.pyplot as plt;
from astropy.io import fits;
from matplotlib.ticker import (MultipleLocator, FormatStrFormatter,
                               AutoMinorLocator)

#####Composite data
CompoM= ascii.read('compoM.data');

CompoM.Wavelength=CompoM['col1'];
CompoM.Flux=CompoM['col2'];

##### fits file

hdulist_KV_RQ1446 = fits.open('flux_KV-RQ1446+0246.fits');
tbdata_KV_RQ1446 = hdulist_KV_RQ1446[0].data;

##### Wavelength
length_KV_RQ1446 = hdulist_KV_RQ1446[0].header['NAXIS1'];
CD1_1_KV_RQ1446 = hdulist_KV_RQ1446[0].header['CD1.1'];
CRVAL1_KV_RQ1446 = hdulist_KV_RQ1446[0].header['CRVAL1'];
Array_KV_RQ1446 = np.arange(0,length_KV_RQ1446);
Wavelength_KV_RQ1446 = Array_KV_RQ1446*CD1_1_KV_RQ1446+CRVAL1_KV_RQ1446;

##### flux
Flux_KV_RQ1446_N = tbdata_KV_RQ1446[0,:];
Flux_KV_RQ1446 =[]

for i in range(length_KV_RQ1446):
    Flux_KV_RQ1446.append(Flux_KV_RQ1446_N[0,i]);

##### Composition galaxy plot and redshift
Redshift = 2.07
Wavelength_Test =Wavelength_KV_RQ1446/(1+Redshift)
Flux_Test = np.array(Flux_KV_RQ1446) * 10E16

#####Extinction model with SMC

lam = CompoM.Wavelength
flux = CompoM.Flux

#Parameters
z = Redshift
AB = 0.2

#SMC extinction parameters
ai = np.array([185.,27.,0.005,0.010,0.012,0.030])
wli = np.array([0.042,0.08,0.22,9.7,18.,25.])
bi = np.array([90.,5.50,-1.95,-1.95,-1.80,0.0])
ni = np.array([2.0,4.0,2.0,2.0,2.0,2.0])
Ki = np.array([2.89,0.91,0.02,1.55,1.72,1.89])

#Do it for Quasar
AlambdaQ = flux*0.
wlrQ = lam/1e4
for e in range(len(ai)):
    AlambdaQ=AlambdaQ+ai[e]/((wlrQ/wli[e])**ni[e]+(wli[e]/wlrQ)**ni[e]+bi[e])

AlambdaQ = AlambdaQ*AB
modelQ = 10**(-0.4*AlambdaQ)*flux

ii = np.where((lam*(1+z) > 6900) & (lam*(1+z) < 7100))
norm = np.mean(flux[ii])
normmodel = np.mean(modelQ[ii])

ii_2 = np.where((Wavelength_KV_RQ1446 > 6900) & (Wavelength_KV_RQ1446 < 7100))
Flux_KV_np= np.array(Flux_KV_RQ1446)
norm_KV = np.mean(Flux_KV_np[ii_2])

#Make plot
#plt.figure(figsize=(12,8))
fig, ax = plt.subplots(figsize=(12,8))
plt.plot(Wavelength_Test, Flux_KV_RQ1446, label='KV-RQ1446+0246', color='black', linestyle='dashed', zorder=2)
plt.plot(lam, modelQ/normmodel*norm_KV, label = '_SMC_extinction_model', color='tab:red', zorder=3)
plt.plot(CompoM.Wavelength, CompoM.Flux/normmodel*norm_KV, label = 'Composite_QSO_template', color='tab:blue',
         zorder=3)

```

```

plt.xlim(1000,2500)
ax.xaxis.set_major_locator(MultipleLocator(100))
ax.xaxis.set_minor_locator(MultipleLocator(20))
ax.yaxis.set_major_locator(MultipleLocator(0.5E-16))
ax.yaxis.set_minor_locator(MultipleLocator(0.25E-16))
ax.tick_params(axis='both', which='major', labelsize=10, direction='in', top='on', right='on')
ax.tick_params(axis='both', which='minor', labelsize=0, direction='in', top='on', right='on')
#plt.ylim(0,2)
plt.xlabel('Rest Wavelength [ ]')
plt.ylabel('$Flux [erg/cm^{2}/s/A]$')
plt.annotate('z=2.07, A_{B}=0.2$', xy=(2200,0.6E-16))
plt.legend()
plt.grid(True)
plt.show()

```

7.6 The script: Voigt profile

```

from astropy.io import ascii;
import numpy as np;
import matplotlib.pyplot as plt;
from astropy.io import fits;

from matplotlib.ticker import (MultipleLocator, FormatStrFormatter,
                               AutoMinorLocator)
### Input

hdulist = fits.open('flux_KV-RQ1500-0013.fits');
# Normalized spectra
DLA_Check = np.loadtxt('KV-RQ1500-0013-Bal-Check.nspec');

### Input the data Blue

###

Redshift = 2.52
AB = 0.2
### Wavelength
tbdata= hdulist[0].data;

length = hdulist[0].header['NAXIS1'];
CD1_1 = hdulist[0].header['CD1_1'];
CRVAL1 = hdulist[0].header['CRVAL1'];
Array = np.arange(0,length);
Wavelength = Array*CD1_1+CRVAL1;
Wavelength_Test = Wavelength/(1+Redshift)

### flux
Flux = tbdata[0,:];

Flux_KV =[]

for i in range(length):
    Flux_KV.append(Flux[0,i])

###

DLA_Check_Wavelength = DLA_Check[:,0]
DLA_Check_Flux=DLA_Check[:,1]
DLA_Check_Wavelength_Test = DLA_Check_Wavelength/(1+Redshift)

###

Wavelength_Test = Wavelength/(1+Redshift)

w_center_adj = 1186
Redshift_DLA = (w_center_adj*(1+Redshift) - 1215.67) /1215.67
#redshift is 2.434

# Voigt Hjerting function of
#the numerical approximation.
def H(a, x):
    P = x**2
    #zeroth order
    H0 = np.exp(-(x**2))
    Q = 1.5/x**2
    H = H0 - (a/np.sqrt(np.pi))/P*(H0*H0*(4*P*P+7*P+4+Q)-Q-1)
    print(P, H0, Q)
    return H

#Constants.
c = 2.998E8

#oscillator strength
f = 0.416
#Doppler parameter (related to the kinetic temperature of the gas)
b = 10E3

w10 = (w_center_adj)*1E-10

#damping constant
gamma = 6.265e8

```

```

#damping parameter a
a = w10*gamma/(4*np.pi*b)

#the thermal or Doppler broadening
dwld = b/c*w10

#Need to check. I believe it is the C N a part.
front = 1.498e-2*((f*w10)/b)

#Density
N = 10**20.9
logN = np.log10(N)
deltalogN = 0.2

N1 = 10**(logN+deltalogN)
N2 = 10**(logN-deltalogN)

#Test wavelength
wl = (np.arange(200000)/100.+500.)*1E-10

#The variable x is the wavelength displacement from line center,
x = (wl-w10)/dwld
binsize = wl[11]-wl[10]

#Plotting the absorption coefficient exp(-tau), tau = (C N a ) H
fig, ax = plt.subplots(figsize=(9,7))
plt.plot(wl*1E10,np.exp(-front*N*H(a, x)),color='blue',zorder=2,label = 'Voigt_profile')
plt.plot(wl*1E10,np.exp(-front*N1*H(a, x)),color='red',zorder=2,linestyle='dashdot')
plt.plot(wl*1E10,np.exp(-front*N2*H(a, x)),color='red',zorder=2,linestyle='dashdot')
plt.xlim(1140,1250)
plt.plot(DLA_Check_Wavelength_Test,DLA_Check_Flux,color='black',linestyle='dashed',zorder=2,label = 'KV-
RQ1500-0013')
plt.axhline(y=1,color='red',linestyle='-')
plt.ylim(0,1.25)
plt.annotate('log($N_{HI})_{\pm}(20.9_{\pm}0.2)_{\text{cm}^{-2}}$', xy = (1200,0.3),size=15)
plt.xlabel('lambda_{i}')
plt.ylabel('Flux')
plt.grid(True)
plt.legend()
plt.xlabel('Rest_Wavelength_['])
plt.ylabel('Normalized_Flux')
ax.xaxis.set_major_locator(MultipleLocator(20))
ax.xaxis.set_minor_locator(MultipleLocator(5))
ax.yaxis.set_major_locator(MultipleLocator(0.2))
ax.yaxis.set_minor_locator(MultipleLocator(0.1))
ax.tick_params(axis = 'both', which = 'major', labelsize = 10, direction = 'in', top= 'on', right = 'on')
ax.tick_params(axis = 'both', which = 'minor', labelsize = 0, direction = 'in', top= 'on', right = 'on')
plt.show()

```